

**Porous Metal Oxides: Catalysts for Activation of  
Small Molecules**

vorgelegt von

M.Sc. Elham Baktash

aus Amol, Iran

von der Fakultät II – Mathematik und Naturwissenschaften

der Technischen Universität Berlin

zur Erlangung des akademischen Grades

Doktor der Naturwissenschaften

- Dr. Rer. Nat. -

genehmigte Dissertation

Promotionsausschuss:

Vorsizender: Prof. Dr. Michael Gradzielski

Gutachter: Prof. Dr. Arne Thomas

Gutachter: Prof. Dr. Holger Dau

Tag der wissenschaftlichen Aussprache: 20. August 2014

Berlin 2014

D83

*The work presented herein was carried out in the research group of Prof. Dr. Arne Thomas (functional materials group) at the department of chemistry at Technische Universität Berlin, Germany, in the time between Jun. 2011 and Jun. 2014.*



## Acknowledgements

I would like to express my gratitude to all those who gave me the possibility to complete this thesis.

I wish to thank ...

... Prof. Dr. Arne Thomas, the supervisor of this work, for making it possible in the first place, for the experience of scientific freedom and for all the support during my PhD. It has been an honour working in his group,

... Prof. Dr. Matthias Driess, the second supervisor of this work for his support and the productive collaboration,

... Prof. Dr. Holger Dau, the reviewer of this work, for his kind support, a very nice and fruitful collaboration and scientific discussions,

... Prof. Dr. Reinhard Schmäcker for his help and support with the catalytic part of this thesis,

... Prof. Peter C. Stair for his generosity which also gave me the opportunity to work in his group and learn ALD technique which resulted in a very interesting outcome presented in this thesis,

... Dr. Ivelina Zaharieva and Dr. Petko Chernev my colleagues in Free University, Patrick Littlewood, Marc Schröder, Johannes Pfrommer from TU Berlin and Dr. Alexis Jhonson, Cassie George, James McCarthy Dr. Kunlun Ding, Mike S. Liu, Sicelo Masango and Dr. Alex Peroff From Northwestern University,

... All members of the Thomas group, Christina Eichenauer, Daniel Becker, Hakan Bildirir, Dr. Jens P. Paraknowitsch, Dr. Jérôme Rôeser, Dr. Johannes Schmidt, Dr. Kamalakannan Kailasam, Dr. Kerstin Thiel, Maria Unterweger, Matthias Trunk, Dr. Michael J. Bojdys, Miriam Klapproth, Dr. Phisan Katekomol, Dr. Robert Dawson, Sabrina Fischer, Sophie Kücken, Viktoria Mainka tryandwinha, Dr. Xiao Xie for much more than being a colleague,

... Anne Sobotta, the soul of our group, for everything she has done for all of us.

I would like to thank BIG-NSE (graduate school of UniCat) and Durchstarter Stipendium (Start-Up Scholarship) for the financial support.

I am beyond grateful to my family, my parents and my brother Amin for their faith and support.

My especial thanks to my husband Mehran, for all his encouragement and support.

## Abstract

In order to meet the increasing energy demand of our world in future, it is crucial to change or improve the traditional ways of energy production and consumption. In this respect, strategies like the development of suitable technologies to take full advantages of sustainable energy sources such as sunlight, a more efficient use of fossil fuels like  $\text{CH}_4$  and converting waste materials like  $\text{CO}_2$  or  $\text{CH}_4$  into a source of energy should be considered. Therefore catalytic conversion of small molecules such as photocatalytic splitting of water which produces  $\text{H}_2$  as clean and renewable source of energy or dry reforming of methane to produce syngas as raw material for fuel production are two interesting but challenging processes. For these reactions, the development of highly active and selective catalysts is of crucial importance. In this contribution novel strategies to prepare porous metal oxides are presented that have the potential to activate small molecules ( $\text{CH}_4$ ,  $\text{H}_2\text{O}$ , etc.) and convert them into useful fuels.

In this work, varied types of synthetic protocols were employed to prepare materials as catalyst for water oxidation and dry reforming of methane. The first part of this thesis is focused on preparation and characterization of porous calcium-manganese oxides with a unique foam-like nanostructure prepared via a facile and robust synthetic route using cyanamide as porogen. A series of such oxide foams annealed at different temperatures was characterized by TEM, SEM, XRD,  $\text{N}_2$  physisorption, and X-ray absorption spectroscopy (XAS) in order to correlate crystallinity, atomic structure, surface area and oxidation state of the materials with catalytic activity. Some of the resulting CaMn oxides show high activity as catalysts for water oxidation in presence of cerium(IV) ammonium nitrate as a non-oxo transfer oxidant. Amorphous calcium-manganese-oxide foam with  $130 \text{ m}^2 \cdot \text{g}^{-1}$  surface area and Mn oxidation state of +3.6 was identified to be most active and its activity is superior to previously reported CaMn oxides. At the atomic level, this material shares structural motifs with the biological paragon as revealed by dual-edge XAS at the Mn and Ca K-edge. Rather than nanostructure and surface area, the atomic structure of the CaMn oxide and the extent of structural order appear to be crucial determinants of catalytic activity. Fully disordered low-valent Mn materials as well as high-valent but crystalline CaMn oxides are unreactive. Highly disordered variants of layered manganese oxide with Ca and water molecules interfacing layer fragments are most reactive.

In the second part of the project, porous nickel manganese oxides with different ratio between nickel and manganese were prepared using the same cyanamide-based protocol. NiMn oxides with high surface area and foam-like structure, showed high activity for the dry reforming of methane (DRM) reaction. The thermodynamic equilibrium of the DRM reaction at  $500 \text{ }^\circ\text{C}$  is achieved with a  $\text{NiMn}_2\text{O}_x$  foam catalyst. The catalyst showed stable conversion during the time on stream.

Supported Ni NPs were also prepared by impregnation of SBA-15 as highly porous silica support using aqueous solutions of a Ni4 cubane molecule as precursor. This cubane molecule is a tetranuclear complex with di-2-pyridyl ketone  $[(\text{C}_5\text{H}_4\text{N})_2\text{CO}$ , dpk] as ligand. Using this ligand stabilized, preformed nickel oxide nanoparticles as precursor yield the formation of highly dispersed Ni NPs on silica support after heat treatment. The resulting materials showed improved catalytic activity and stability compared to the ones prepared using  $\text{Ni}(\text{OAc})_2$  as nickel precursor.

The next group of Ni-based catalyst was prepared by employing the atomic layer deposition technique. Different numbers of alumina ALD cycles (5, 10, 15, 20) were applied to form protective alumina overcoats around Ni species. The obtained materials employing 5 and 10 cycles of alumina

ALD showed significant improvement in catalytic activity as well as stability in DRM reaction at elevated temperatures (700-800).

The influence of different parameters, such as the Ni : Mn ratio, the Ni NP size and dispersion or the support structure on the catalytic performance, especially regarding activity and stability in the DRM reaction is critically discussed.

## Table of content

1.	Introduction.....	1
1.1	Renewable energy sources .....	2
1.2	Photosynthesis: Nature’s way for energy conversion and storage.....	2
1.3	Alternative energy production-Artificial photosynthesis .....	4
1.4	Alternative energy production-Dry reforming of methane .....	5
1.5	Porous metal oxides as catalyst for heterogeneous catalysis.....	6
1.5.1	Sol-gel method.....	7
1.5.2	Templating method .....	9
1.5.3	Supported catalysts by Immobilization of NPs on porous materials.....	10
1.5.3.1	Impregnation .....	10
1.5.3.2	Atomic Layer Deposition .....	11
1.6	Motivation .....	14
2.	Results and discussion.....	16
2.1	Metal-based catalyst for water oxidation.....	16
2.1.1	Co and Ni oxides .....	17
2.1.2	Manganese oxides .....	17
2.2	Synthesis and characterization of porous CaMn oxides.....	19
2.2.1	Calcium manganese oxides as water oxidation catalysts .....	33
2.2.2	Elucidation of structural details.....	38
2.2.2.1	Manganese oxidation states.....	38
2.2.2.2	Information on atomic structure from EXAFS .....	40
2.2.3	Optimum amount of template for CaMn <sub>2</sub> O <sub>x</sub> -A-400.....	44
2.3	Synthesis and characterization of nickel, cobalt and manganese oxides.....	47
2.4	Synthesis of Cu, Cr, Fe and Sn oxides .....	54
2.5	Summary and conclusion.....	56
2.6	Catalysts for dry reforming of methane .....	57
2.6.1	Introduction.....	57
2.6.2	Effect of supporting material on the catalytic activity of Ni-based catalysts.....	57
2.6.3	Effect of metal content on the activity of Ni-based catalysts .....	58
2.6.4	Role of promoters in Ni-based catalysts .....	58
2.6.5	Methods of catalyst preparation .....	59
2.7	Results and discussion .....	60
2.7.1	Nickel manganese oxides .....	60

2.7.2	Synthesis and characterization of porous nickel manganese oxide .....	61
2.7.3	Catalytic test on NiMn <sub>2</sub> O <sub>x</sub> .....	62
2.7.4	Synthesis and characterization of NiMn <sub>6</sub> O <sub>x</sub> and NiMn <sub>8</sub> O <sub>x</sub> .....	63
2.7.4.1	Catalytic activity of NiMn <sub>6</sub> O <sub>x</sub> and NiMn <sub>8</sub> O <sub>x</sub> .....	65
2.7.4.2	The source of catalyst deactivation .....	66
2.8	Supported nickel oxide nanoparticles .....	70
2.8.1	Catalytic performance of Ni <sub>4</sub> /SBA-15 and Ni/SBA-15 in DRM reaction .....	76
2.9	Coated Ni-based catalysts.....	79
2.9.1	ALD-formed alumina overcoat .....	80
2.9.2	Alumina overcoated Ni nanoparticles.....	81
2.9.2.1	Catalytic test on alumina coated Ni NPs .....	83
2.9.3	Alumina coated NiO nanopowder .....	85
2.9.3.1	Catalytic test on NiO nanopowder.....	87
3.	Summary and outlook .....	93
4.	Experimental.....	96
4.1	Synthesis of CaMn <sub>2</sub> O <sub>x</sub> -A-B.....	96
4.2	Synthesis of CaMn <sub>2</sub> O <sub>x</sub> -A-400.....	97
4.3	Synthesis of M-A.....	98
4.4	Synthesis of porous nickel manganese oxides .....	99
4.5	Supported Ni particles on SBA-15 .....	100
4.5.1	Syntheses of Ni precursor .....	100
4.5.2	Preparation of SBA-15.....	100
4.5.3	Synthesis of Ni <sub>4</sub> /SBA-15 and Ni/SBA-15 catalysts.....	100
4.6	Alumina overcoated Ni and NiO nanostructures .....	101
4.7	Catalytic tests .....	101
4.7.1	Chemical water oxidation test with Clark electrode.....	101
4.7.2	Chemical water oxidation test with Gas Chromatography .....	102
4.7.3	Catalytic test for DRM reaction .....	103
4.7.3.1	Thermodynamic equilibrium of the DRM reaction under the standard conditions	103
5.	Characterization methods .....	104
5.1	Electron microscopy (EM).....	104
5.1.1	Scanning electron microscopy (SEM).....	105
5.1.2	Transmission electron microscopy (TEM) .....	106
5.1.3	Energy dispersive X-ray spectroscopy.....	108
5.2	X-Ray Diffraction .....	108

5.3	X-ray Absorption Spectroscopy XAS .....	109
5.4	Nitrogen sorption .....	111
5.4.1	Determination of the surface area .....	112
5.5	Instrumental details .....	113
6.	Appendix.....	114
7.	References.....	127

### 1. Introduction

Massive development in agricultural productivity and medical advances caused rapid population growth in the last decades. In 1995 the world population was 5.7 billion, with an increase of 1.3% per year. It was more than 6 billion in 2010 and is expected to be about 9.2 billion people until 2050.<sup>[1]</sup> This strong increase in population and the availability of large amount of fossil fuels have led to an average primary energy consumption rate of almost 15 trillion watts of power worldwide. Primary energy is the energy from natural sources before undergoing any human-made conversion. This energy can be converted into useful energy like electricity, heat and fuels. The last source is the most proper one because of its capability to be stored, transported and used when needed.

Current trends in energy production and consumption are not environmentally and economically sustainable. In a system with restricted energy sources, opportunities discovered by one generation can cause problems and limitations for the next generation. Fossil fuels brought significant opportunities for rich countries in the 20th century but now world has to face the problems arising from the overexploitation of fossil fuels.<sup>[2]</sup> Despite this problem, more energy yet is needed to fill the gap between industrial and developing countries. Contrarily we should not consume fossil fuels because of not only their limited amount, but also their ever increasing price and the effect on global warming via CO<sub>2</sub> emission. The climate change which is caused by increasing in CO<sub>2</sub> emission will have an impact on food security<sup>[2]</sup>, water availability<sup>[3]</sup>, global forest<sup>[4]</sup> and at the end lead to devastating effect on humanity.<sup>[5]</sup> This means we have to save energy, find better ways for extracting energy from traditional sources or developing new ones. In this respect the catalytic conversion of small molecules such as photocatalytic splitting of water into hydrogen and oxygen ( $2\text{H}_2\text{O} \rightarrow 2\text{H}_2 + \text{O}_2$ ) and the CO<sub>2</sub> reforming of methane ( $\text{CH}_4 + \text{CO}_2 \rightarrow 2\text{CO} + 2\text{H}_2$ ) are two highly interesting but also challenging reactions. Water splitting can produce hydrogen as a clean and renewable source of energy, which could be used directly as a fuel or in other chemicals production. The synthesis gas (CO + H<sub>2</sub>) which is the product of reforming reaction can be converted into higher hydrocarbons or fuels via Fischer-Tropsch (FT) synthesis.<sup>[6,7]</sup> However both processes (water splitting and dry reforming of methane) are amongst the most challenging and energy demanding reactions. Therefore development of cheap and efficient catalysts capable of reducing the required activation energies as well as preventing unwanted side reactions is of crucial importance. In this contribution novel strategies are presented to prepare porous metal oxides that have the potential to activate small molecules (CH<sub>4</sub>, H<sub>2</sub>O) and convert them into useful fuels.

### 1.1 Renewable energy sources

One way to overcome world's increasing energy demand and global warming in future is to replace traditional energy sources like fossil fuels with sustainable sources of energy. There are several options as replacement for fossil fuels such as solar energy, wind, geothermal, ocean and biofuels. Renewable energy sources already play an important role in energy production in many countries around the world. In the European Union, almost 70% of the additions to electric capacity in 2012 mostly came from solar photovoltaic and wind power. In Germany, 22.9% of electricity, 10.4% of national heat consumption and 12.6% of total final energy demand were covered by renewable sources.<sup>[8]</sup>

Among all kinds of renewable sources, solar energy has by far the largest potential. Comparison between the average solar flux of  $170 \text{ Wm}^{-2}$  over the entire earth's surface which yields about 90 PW of incoming solar power and the amount of primary energy consumption of the early 21st century which is about 15TW shows that the sun can provide about 6000 times more energy than our current energy consumption.<sup>[5]</sup> Therefore solar energy is applicable even in a scenario which estimates future global energy demand up to 40 TW in 2050.<sup>[9]</sup> But currently only a small fraction of this enormous potential energy source is used in photovoltaic and solar-thermal heating. In order to take advantage of renewable energy sources including solar energy, some challenges should be overcome. Existing technologies for energy production as well as consumption should be optimized to achieve higher efficiencies and decrease energy demand where possible. Moreover we need to develop new technologies or improve the existing ones in the field of energy conversion and storage. So far all these types of renewable sources (wind, ocean, sun, etc.) were applied for the production of heat and electricity but not for fuels. To produce fuels which can be stored or used in transportation in a sustainable manner, research activities in development of methods and materials should be intensified. One way to approach this goal is to follow nature. In nature green plants use sun in order to convert  $\text{CO}_2$  into biomass which can be stored for later utilization. The ability to mimic this process in a simplified manner would be a major step towards sustainable energy production.

### 1.2 Photosynthesis: Nature's way for energy conversion and storage

Photochemistry which is the interaction between light and substances is one of the most important phenomena in our world. Via photosynthesis, light energy is captured and converted into chemical energy. All energy sources for our life, such as our food or fossil fuels are the result of this light-material interaction.<sup>[10]</sup> One of the important factors which make such a process successful and long-lasting is that the power (sunlight) and the required raw materials (water and carbon dioxide) are abundantly available. Although, due to the diverse conditions of different photosynthetic organisms,

## Introduction

---

some of them uses different types of materials such as  $\text{H}_2\text{S}$ <sup>[11]</sup> or  $\text{NO}_2$ <sup>[12]</sup> instead of  $\text{H}_2\text{O}$ . This process which is called anoxygenic photosynthesis will not be discussed here.

Oxygenic or oxygen-evolving photosynthesis which takes place in plants, algae and cyanobacteria consists of the splitting of water by sunlight into oxygen and hydrogen. Oxygen is released to the atmosphere but hydrogen reacts with carbon dioxide to make organic compounds. Photosystem II provides reduction equivalents, which are needed to convert  $\text{CO}_2$  into biomass as energy storage. These reduction equivalents are produced via water oxidation. The active site of PSII for water oxidation reaction consists of a  $\mu$ -oxido ( $\mu\text{-O}^{2-}$ )  $\text{CaMn}_4$  cluster. Zou et al. published the first X-ray structure of PSII, which showed the framework of this complex at 3.8 Å resolution.<sup>[13]</sup>

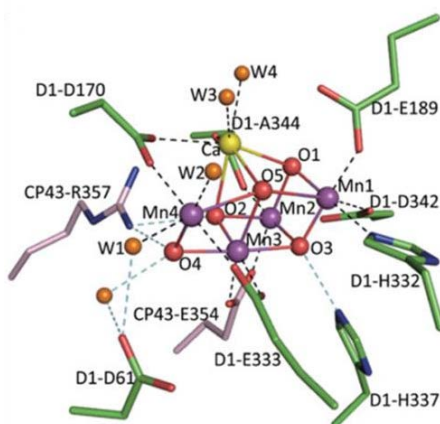
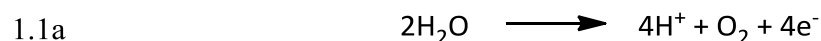


**Fig. 1.1: Schematic representation of the oxygen-evolving-complex.**<sup>[13]</sup>

In 2011, Umena et al. published a crystal structure of PSII at a resolution of 1.9 Å.<sup>[14]</sup> In agreement with previous works<sup>[15-18]</sup>, it has been shown that three Mn and one Ca of the  $\text{CaMn}_4$  cluster are connected via four  $\mu_3\text{-O}$ -bridging ligands, resulting in a distorted cubane-like motif. The fourth Mn and a fifth O is attached to one edge of the cube (Fig. 1.1).<sup>[14]</sup> Water oxidation takes place via the following chemical reaction, which indicates that four electrons and four protons are removed from two water molecules generating an oxygen molecule.

## Introduction

---



Water is a very stable molecule, so its oxidation is a challenging reaction. Because of this characteristic, the photosynthetic oxygen evolving complex is the only biochemical system that performs this reaction in nature. Photosynthesis is an outstanding process for the conversion and storage of solar energy into chemical energy out of abundant and non-toxic materials with the rate of 120 TW per year.<sup>[19]</sup> With such an energy production rate, this system could be a paragon for sustainable energy generation.

### 1.3 Alternative energy production-Artificial photosynthesis

Among all sort of sustainable energy sources, solar energy is the most available one. Therefore investigations have been started in order to find ways to apply sunlight in clean fuel production.

The possibility of fuel production by artificial photosynthesis was first brought up by an Italian chemist named Giacomo Ciamician at 1912.<sup>[20]</sup> He estimated that "This enormous quantity of energy that the earth receives from the sun, in comparison with which the part which has been stored up by the plants in the geological periods is almost negligible, is largely wasted." He suggested finding photochemical reactions for capturing the solar energy that hits the earth. Then by means of a sustainable catalyst, mimic the light-driven conversion of CO<sub>2</sub> into useful fuels.<sup>[20]</sup> At his time the major energy source was coal. Later by replacement of coal with partially clean and easy to extract oil and gas as well as discovery of nuclear energy, it was assumed that energy problem has been solved.<sup>[5]</sup> Ciamician's idea about artificial photosynthesis was brought up again after the energy crisis of the 1970<sup>[21,22]</sup> and gained extensive attention recently after realization of fossil fuels' burning consequences and difficulties with nuclear energy.<sup>[5,23]</sup> However, it is also predictable that the complicated process of photosynthesis cannot be exactly and easily duplicated by an artificial process. Therefore it is necessary to cut the process down into simple steps that can be functionally mimicked.

As mentioned before, if hydrogen could be generated from water splitting, the energy and environmental problems of human being would be largely decreased. Therefore many research groups have recently focused on finding a way to mimic this portion from the whole photosynthetic

process. The splitting of water into hydrogen and oxygen, ideally in presence of sunlight is one of the most challenging reactions in chemistry. Water splitting includes two chemical processes, water oxidation and proton reduction (1.1)

Finding a robust catalyst for the thermodynamically and kinetically demanding water oxidation reaction<sup>[24]</sup> is a crucial requirement for the development of an economic solar-driven water oxidation device. By the urgent need for development of an efficient oxidation catalyst for incorporation into water splitting devices and inspired by the structure of the oxygen evolving center (OEC) of PSII, significant efforts have been made to mimic the water oxidation center of PSII functionally. Therefore solid-state materials, molecular complexes and clusters have been investigated as water oxidation catalyst in homogenous or heterogeneous media as well as deposited on electrodes.<sup>[25]</sup>

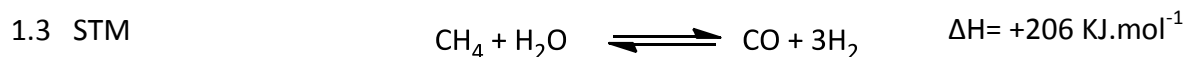
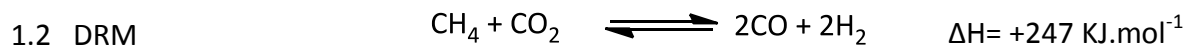
### 1.4 Alternative energy production-Dry reforming of methane

Fuels such as coal, natural gas and petroleum are the major energy sources in transport, industry and in the production of electricity. Global warming caused by continuous use of these fuels has resulted in damaging effects in our environment and the depleting levels of their supplies continues to drive interests in the alternative fuel sources. In recent years, it has been obvious that a drastic shift in energy generation, conversion and consumption is needed in order to meet the global energy demands of the future and to avoid global warming. Therefore more efficient use of fossil fuels or the development of processes that allows us to generate alternative fuels in a sustainable manner is key challenges of this century. One possible strategy that recently has received attention is the activation of small molecules such as methane. Methane, which is the principal component of natural gas, is currently being used for home and industrial heating. Large amounts of methane are found in areas that are located far away from industrial regions. Therefore its transportation is uneconomical or even impossible. At the moment, a part of the methane obtained, is flared or vented which is waste of hydrocarbon resource and causes more environmental problems. These concerns and the increasing oil price have led to world-wide investigation for directly converting methane into easy transportable products.

Reforming reactions of methane play a key role in the production of syngas, a mixture of hydrogen and carbon monoxide from natural gas which is made up of 98% CH<sub>4</sub>. It is known that methane reforming has two major types, i.e., steam reforming (STM) and dry reforming (DRM). At industrial scale, syngas is used for the production of numerous chemicals, including methanol, dimethyl ether, Fischer-Tropsch chemicals, ammonia, acetic acid, and formic acid<sup>[26-29]</sup>, which can potentially be used both as fuel and as feedstock for petrochemical industries.

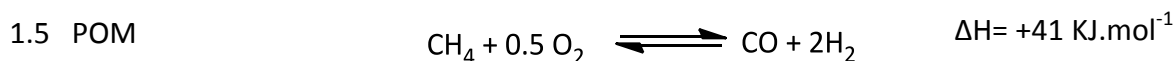
## Introduction

---



Methane and carbon dioxide which are used in DRM are two of the cheapest and most abundant carbon-containing materials that can be transformed into useful products. On the other hand the two gases which both consumed by this reaction are undesirable greenhouse gases.

Reforming with  $\text{CO}_2$ , rather than  $\text{H}_2\text{O}$ , is attractive because it can be applied in regions where water is not available and it yields syngas with lower  $\text{H}_2/\text{CO}$  ratios which makes it a preferable feedstock for the Fischer–Tropsch process for production of long-chain hydrocarbons<sup>[30]</sup>. This is the key advantage of Dry reforming reaction over other reactions such as the partial oxidation of methane and steam reforming of methane where  $\text{H}_2/\text{CO}$  ratios of 2 and 3 are obtained. The product ratio resulting from dry reforming of methane is directly affected by the tendency of the  $\text{H}_2$  to react via the reverse water gas shift (RWGS) reaction, which results in  $\text{H}_2/\text{CO}$  ratios less than one.



However both reforming reactions are thermodynamically unfavorable. Therefore in order to both decrease the effect of RWGS reaction on  $\text{H}_2/\text{CO}$  product ratio and increase the yield of the products, suitable catalysts should be employed which can improve the conversion rate and prevent side reactions from occurring. Despite the considerable effort in this area, no applicable process has developed which results in satisfactory yield and stability. The main problem that needs to be addressed for the DRM reaction is deactivation by coke formation and sintering of the catalyst. Thus, catalyst development becomes a major aspect of research in this area.

### 1.5 Porous metal oxides as catalyst for heterogeneous catalysis

In heterogeneous catalysis, porosity of the solid phase which provides a good accessibility to the active sites is an important factor. A porous material (porous media) is a material containing pores or voids. Many natural substances such as rocks, soil, zeolites, biological tissues (e.g. bones, wood, and

## Introduction

---

cork) and artificial materials such as ceramics and cements can be placed in the category of porous materials. The concept of porous material has been vastly used in many areas of applied science and engineering such as filtration, liquid adsorption and catalysis. They have been applied either as catalyst themselves or as an inert support for the active phase. Some of porous materials have the ability to, at the same time, act as support and also take part in the catalytic process.<sup>[31]</sup>

A useful way to classify a nanoporous material is by the size of their pores, because most of properties interesting for applications of adsorption and diffusion are dependent to this parameter. Porous materials are classified into three categories, based on their pore size: Micropores with pore diameter less than 2 nm, mesopores with pores between 2-50 nm and macropores with pore diameter larger than 50 nm. The size distribution, shapes and volume of the porous materials determine their potential to be applied for a particular function. For instance mesoporous materials are typically used as catalyst support, because of their high surface area which makes them suitable for anchoring the active material as well as diffusion of the reactant and products.<sup>[31]</sup> More than structural characteristics of porous materials, their chemical nature also plays an important role in their application. Porous materials can be obtained via two main pathways:

- top-down approach, creating empty spaces in a bulk material
- bottom-up approach, synthesizing the material with already formed empty spaces inside

With the first approach, we start from a bulk, non-porous material, and then empty spaces will be created by physical or chemical etching. The second approach is principally based on chemical methods. Via these methods, material precursors arrange or react to form the porous nanostructures. Pores could be formed in two main ways: precursors self-assemble in a regular open pore structure (as seen in metal-organic framework) or they condense around specific molecules, called templates, which, once removed, leave the empty spaces or pores (seen in zeolites).<sup>[32]</sup> In recent decades, significant developments were occurred in preparation of porous material through a wide range of synthetic routes using varied types of precursors and templates. Among them sol-gel methods combined with templating approaches are most often used to prepare porous materials. If the porous material itself is not catalytically active, catalysts can be prepared from using impregnation and atomic layer deposition (ALD) methods. As these methods have been used in this project they will be briefly described in following.

### 1.5.1 Sol-gel method

The sol-gel method is a process to synthesize porous materials by their solidification from a solution phase at low temperature.<sup>[33,34]</sup>

## Introduction

In this process, first a clear colloidal solution named sol is formed via primary condensation of the molecular precursors. Then these colloidal particles merge into polymeric chains thus forming a gel. Both stages are controlled by condensation chemistry.

In a sol-gel process, the sol is formed by hydrolysis of metal salts or alkoxide  $M(OR)_n$  precursor.

1.6



Sols can either be used to synthesize powders (e.g. microspheres, nanospheres), or deposited on a substrate to form a film (e.g. by dip-coating or spin-coating), casted into a suitable container with the desired shape (e.g. to obtain monolithic ceramics, glasses, fibers and membranes).

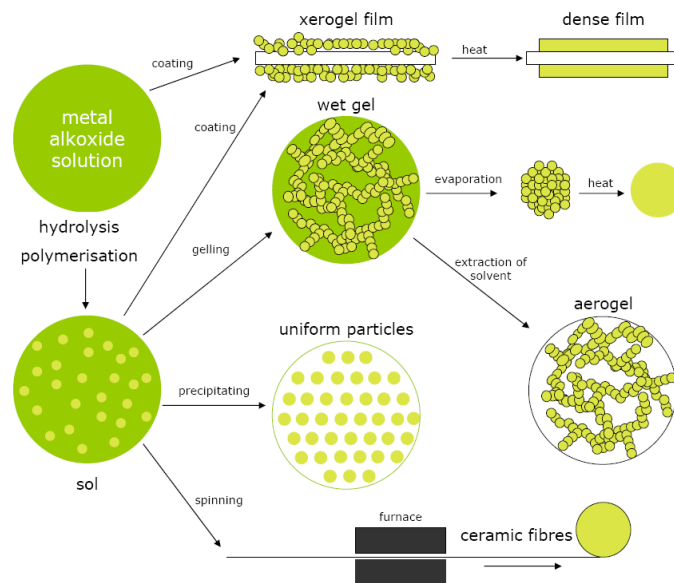
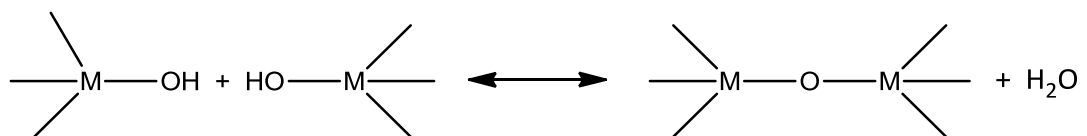


**Fig. 1.2: Schematic representation of the different stages and routes of the sol-gel technology.** <sup>[266]</sup>

Sol formation can be followed by condensation when hydroxide molecules bind together and release water. This step is called gelation.

1.7



## Introduction

---

The gel is a polymer with three-dimensional interconnected pores containing solvent molecules. Removal of the solvent via appropriate drying results in a fine powder of the metal oxide or hydroxide. There are different types of drying methods which yield in products with different properties. For example eliminating the solvent in supercritical conditions (high pressures and temperatures) produces an aerogel, while drying the gel by simple evaporation of the solvent at ambient pressure (Subcritical drying) produces xerogel. Supercritical drying is the best way to maintain the porous and structural properties of the gel. On the other hand subcritical drying which is a fast and cheap method may causes the partial collapse of the porous structure in the obtained xerogel. Finally calcination of the hydroxide leads to the corresponding metal oxide material. Main advantages of the sol-gel method are low temperature and ease of the process which leads in homogeneous, pure, highly porous materials. Moreover the characteristics of the final product such as average pore size, pore size distribution and surface area, can be controlled and tailored via manipulations in the sol-gel process conditions.<sup>[32-34]</sup>

### 1.5.2 Templating method

Generally a “template” is a pattern which is used to replicate, for instance, letters, shapes or designs in graphic arts. In material science, a template represent a particular molecule or structure which helps to generates or design porosity in a matrix. Template-assisted synthesis of porous materials can occur in two pathways: hard-templating (casting) and soft-templating. In hard templating, materials like silica, polystyrene or carbon (nano)structures are used to generate porosity within the material.<sup>[35]</sup> In this process usually the desired material nucleates and grows around the preformed template. Therefore upon the removal of the templating structure, its structural properties are replicated in the formed porous materials.<sup>[32,35,36]</sup> In the soft-templating method, a template acts as structure directing agent (SDA) in the formation of porous materials.<sup>[37]</sup> There are different types of SDAs. Surfactants are a type of SDA, which act as template via formation of self-assembled micelles. Surfactants are amphiphilic molecules containing a hydrophobic tail and hydrophilic head. During soft-templating with surfactants, the template molecules self-assemble into micelles, while the corona of the micelles interacts with the inorganic metal precursor to form a metal-template composite. The inorganic precursors then condense around the micelles, e.g. in the way as described for the sol-gel process. After the removal of the template by calcination or solvent extraction, a porous metal oxide is formed. A large variety of porous metal oxides can be prepared by proper selection of surfactants.

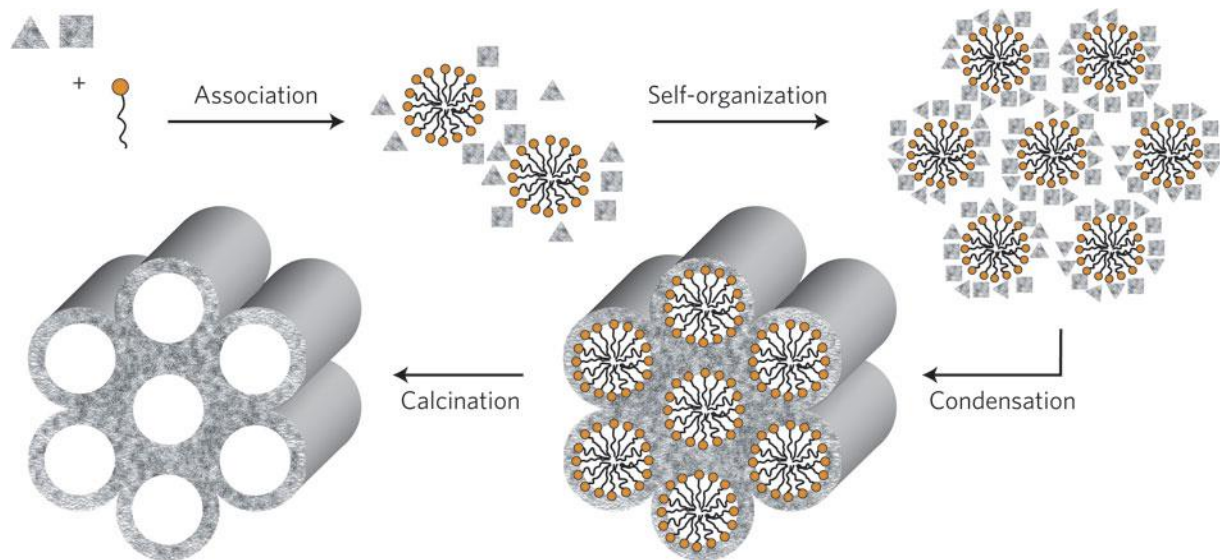


**Fig. 1.3:** The formation mechanism of the porous materials by templating of micelles. <sup>[267]</sup>

### 1.5.3 Supported catalysts by Immobilization of NPs on porous materials

Supported catalysts consist of a catalytically active phase, which are normally metal or metal oxide particles dispersed on mostly high-surface area support. Supported catalysts are important materials in the field of heterogeneous catalysis. The smaller and dispersed the active phase, the larger the fraction of the metal atoms exposed at surfaces, where they are accessible to reactant molecules and available for catalysis. In order to achieve dispersion, the precursor of the active phase should be distributed uniformly.<sup>[31,34]</sup> Various synthetic methods such as impregnation, atomic layer deposition, etc. have been tried in order to uniformly distribute the active phase on the surface of the support.

#### 1.5.3.1 Impregnation

Probably one of the most common techniques for heterogeneous catalysts preparation is impregnation. The term “impregnation” which originates from the traditional vocabulary of industrial chemistry refers to absorption of a liquid phase by a solid. This term defines a procedure in which a certain volume of solution, containing the precursor of the active element of the catalyst, is contacted with the solid support.<sup>[38]</sup> During impregnation the dissolved precursor migrate into the pores of the support which could be a powder, extrudes or pallets. Several chemical species may be present in the impregnation solution, such as; the metal precursor of the active phase, its counter ions and coimpregnants which can effect on the process and resulting materials.

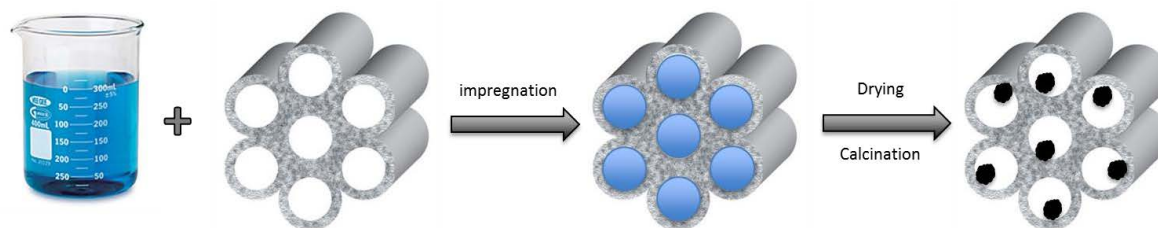


**Fig. 1.4: Schematic illustration of impregnation method**

Moreover based on parameters like concentration and temperature, different physicochemical phenomena may lead to various types of deposited phases and as a result more or less active catalyst may form.<sup>[34]</sup> According to the volume of the solution added, impregnation can be classified in two categories: one is dry or incipient wetness impregnation.<sup>[38]</sup> In this method, the active metal precursor is dissolved in an aqueous or organic solvent, and then the solution is added to a support having the same pore volume as the volume of the solution that was added. Capillary action draws the solution to the pore.<sup>[39–41]</sup>

Impregnation also can be done by immersing support in the precursor solution, which is called “wet impregnation”. In both cases the impregnation is followed by drying and calcination to drive off the volatile components within the solution as well as deposit the metal on the support.

### 1.5.3.2 Atomic Layer Deposition

Atomic layer deposition (ALD) or atomic layer epitaxy (ALE) is a chemical gas phase deposition technique for the formation of inorganic material layers with thickness down to a fraction of a monolayer.<sup>[42,43]</sup> In this process the reactant gases are separately introduced to the substrate and growth is achieved via self-limiting surface reactions. High uniformity and excellent thickness control which is results from this process leads in deposition of very thin film with a uniform thickness.

The starting point of ALD is somewhat controversial. The most acknowledged one is dated back to the 1970s in Finland. Suntola and co-workers published a patent in which the growth of ZnS, SnO<sub>2</sub> and GaP were demonstrated.<sup>[44]</sup> Commercial applications of ALD for making thin-films, based on the work of Suntola and co-workers, were started already in the 1980s. The less commonly acknowledged origin of ALD dates back to the 1960s. The group of Aleskovskii described the TiCl<sub>4</sub>/H<sub>2</sub>O process to grow TiO<sub>2</sub> and the GeCl<sub>4</sub>/H<sub>2</sub>O process to grow GeO<sub>2</sub>. The term atomic layer epitaxy (ALE) was in common use to describe the process till 2000.<sup>[45–47]</sup> However later it has been replaced by ALD because of the fact that the most films grown were not epitaxial to their underlying substrates. Moreover, amorphous films were most preferred for dielectric<sup>[48–50]</sup> and diffusion barrier applications.<sup>[51–53]</sup>

## Introduction

---

ALD is based on self-limiting continuous dual reactions between gaseous precursor molecules and a substrate leading in films deposition in an atomic layer-by-layer fashion. In order to avoid mixing of the chemicals, which causes non-self-limiting growth, an inert gas purge period is introduced between each precursor pulse.<sup>[54–56]</sup> Therefore, ALD can deposit uniform and conformal coatings on various kind of materials regardless of their shape and morphology.<sup>[56–58]</sup> As a consequence, ALD has attracted great attention and applied in various fields such as catalysis,<sup>[59–64]</sup> photovoltaics,<sup>[65]</sup> batteries,<sup>[66]</sup> fuel cells<sup>[60,67]</sup> and polymers<sup>[54,68,69]</sup>.

In this respect, Kim et al. showed that deposition of oxide thin films by ALD on metallic catalysts could be an efficient way to enhance their catalytic performance.<sup>[70]</sup> They demonstrated that ALD-formed nanometer-sized TiO<sub>2</sub> islands on Ni powder can enhance its catalytic activity in the DRM reaction. It has been showed that TiO<sub>2</sub>–Ni interface can actually form active sites for catalytic DRM reactions while inhibiting coke formation.<sup>[71]</sup> Moreover recently Shu Hu *et al.* explored the use of thick pinhole-free ALD-formed TiO<sub>2</sub> films to protect Si, as well as GaAs and GaP, from photocorrosion.<sup>[72]</sup> These semiconductors which are efficient photoanodes for solar fuel production, but are unstable in aqueous media. Via this ALD formed “electronically leaky” TiO<sub>2</sub> films, the photogenerated holes are conducted away from the semiconductor to Ni islands on the surface of the film, to be used by Ni oxide for water oxidation into O<sub>2</sub>.<sup>[72]</sup>

Well-dispersed and uniform metal nanoparticles (NPs) formed by ALD showed interesting catalytic activity, which was comparable or better than the ones prepared via conventional methods, such as impregnation and deposition-precipitation.<sup>[73–76]</sup> Recently, Peter C. Stair and others tried to stabilize supported metal NPs using ALD metal oxide coatings.<sup>[64,76]</sup> The motivation behind this procedure was the precise control over the thickness and composition of the protective layers formed by ALD in comparison with other methods such as chemical vapor deposition, grafting, microemulsion, and dendrimer encapsulation.<sup>[77–82]</sup> These less precise methods can yield overly thick shells that reduce mass transport and lower catalytic performance. On the other hand, the catalytic activity of the covered supported metal NPs by ALD, was maintained or even slightly enhanced up to a certain thickness Therefore it can be concluded that ALD is a suitable technique to either form small dispersed metal NPs on porous supports or to form porous cover around metal NPs in order to prevent them from agglomeration.

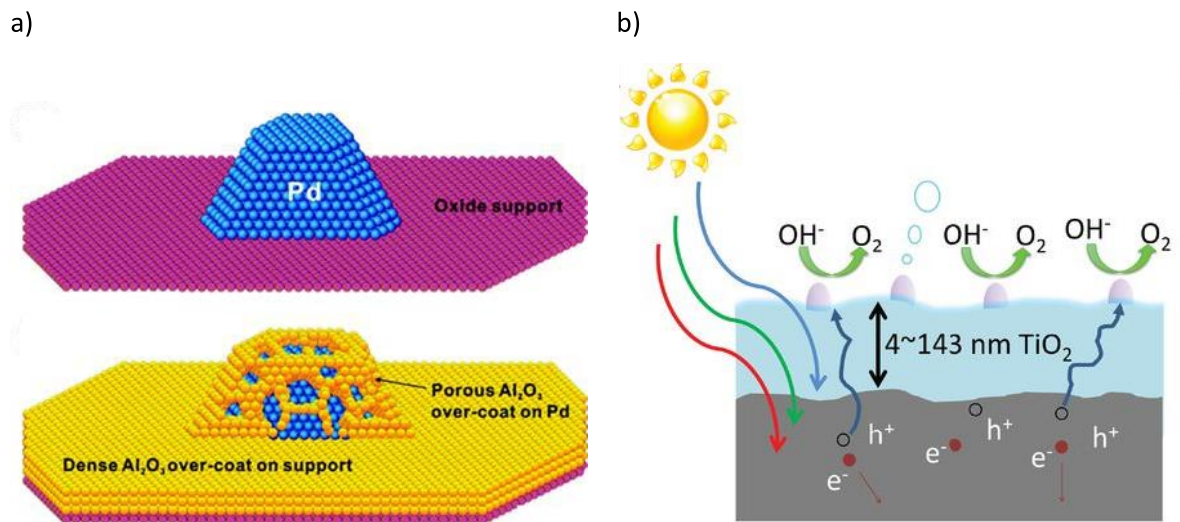


Fig. 1.5: a) Schematic illustration of porous ALD  $\text{Al}_2\text{O}_3$  overcoat on Pd NP<sup>[248]</sup>, b) Cross-sectional schematic of a photoanode stabilized against corrosion in a 1.0 M KOH(aq) by a thick layer of ALD-formed  $\text{TiO}_2$ .<sup>[72]</sup>

### 1.6 Motivation

In order to overcome world's increasing energy demand, we have to either replace the traditional energy sources like fossil fuels with the sustainable forms of energy sources like sunlight or develop materials and technologies for their optimum utilization.

To take full advantage of solar energy, it should be captured and converted into storable forms of energy. In nature this process is taking place in green plants via photosynthesis. The reducing equivalent required for CO<sub>2</sub> conversion by plants into biomass is provided by water oxidation. In scheme of artificial photosynthesis as a solution for energy problem, water oxidation half reaction is one of the major challenges. Therefore a cheap and robust catalyst is in high demand.

The first part of this thesis is focused on preparation and characterization of porous calcium manganese oxides by a novel synthetic protocol with the application in the field of water oxidation. Often metal oxides with unordered and amorphous nature at both the nanostructural and atomic level showed high activity in water oxidation reaction but the insight into structure–reactivity relationship has remained insufficient. On the other hand, well-ordered manganese hydroxides and oxides showed catalytic activity in water oxidation, but only at comparatively low level.<sup>[83–86]</sup> Inspired by the biological catalysts bound to the proteins of photosystem II, the photosynthetic Mn<sub>4</sub>Ca(μ-O)<sub>n</sub> cluster,<sup>[87]</sup> calcium manganese oxides have been also studied as water oxidation catalysts. Indeed, it has been recently shown that incorporation of calcium ions can improve the catalytic activity of synthetic Mn oxides pronouncedly, but only by the amorphous CaMn oxides.<sup>[88,89]</sup>

In heterogeneous catalysts, increasing the surface area, either by forming smaller particles or by creating pores, is a practical pathway to increase the catalytic efficiency of solid materials. For the generation of porous materials most often templating approaches are applied. For example, the inorganic phase can be formed in the presence of an organic porogen, which afterwards is removed leaving behind more or less defined pores in the inorganic matrix. In this study a facile and robust synthetic route using cyanamide as porogen was used to prepare porous binary metal oxides such as calcium manganese and nickel manganese oxides with a unique foam-like structure.

Porous calcium manganese oxides were used as catalyst for water oxidation reaction and investigation has been carried out to study the 1) effect of synthetic parameter on the morphology and atomic structure of the prepared materials and 2) the influence of structural characteristics on the catalytic activity of the catalyst. Moreover the same protocol was used in preparation of a series of other nanostructured metal oxides such as Mn, Co, Ni, Cu, Fe and Sn oxides with varied morphology and application.

## Introduction

---

The second part of the project was focused on dry reforming of methane as the second path for addressing the energy problem by better utilization of the already available sources such as CO<sub>2</sub> and CH<sub>4</sub> for preparation of precursors (syngas) which can be applied in fuels production. Porous nickel manganese oxide was prepared to be used as catalyst for DRM reaction. Nickel is a well-known catalyst for DRM reaction and manganese is a cheap metal which has been reported to act as promoter to enhance the performance of the nickel-based catalysts. Coke formation, which is the major problem in dry reforming reaction, can be extremely prevented by controlling the size of active sites (Ni).<sup>[90]</sup> In this part of the project this problem has been addressed by using manganese as promoter or silica as support. ALD formed alumina overcoats also were used to cover the nickel-based nanostructures in order to prevent them from agglomeration. All these materials were tested as catalyst in dry reforming reaction to study the influence of the morphological and structural characteristics of the catalysts on their activity and stability.

## 2. Results and discussion

### 2.1 Metal-based catalyst for water oxidation

The first homogeneous catalyst capable of oxidizing water into molecular oxygen in presence of a single-electron oxidant  $Ce^{4+}$  was introduced by Mayer and coworkers in the early 1980. This compound was a mono  $\mu$ -oxido-bridged dinuclear ruthenium complex  $[(bpy)_2(H_2O)Ru^{III}ORu^{III}(H_2O)(bpy)_2]^{4+}$ , known as blue dimer<sup>[91,92]</sup>.

Catalytic activity in water oxidation reaction has also been documented for complexes containing other transition metals. For example Co-based catalysts, capable of catalysis of water oxidation reaction are also gaining attention recently.<sup>[93]</sup> Some of these single-site and multi-metallic Co complexes were introduced by Nocera, Berlinguette<sup>[94–95]</sup> and Dismukes.<sup>[97,98]</sup> However some of them act as precursors for  $CoO_x$  nanoparticles that are responsible for water oxidation catalysis.<sup>[96,99]</sup>

Homogeneous manganese-containing complexes have been widely studied as models of oxygen evolving center (OEC) of PSII.<sup>[100–104]</sup> However, based on  $^{18}H_2O$  isotope-labeling test, just few of them are capable of catalyzing the water oxidation reaction. Recently the first known manganese complex capable of water oxidation catalysis in presence of a single-electron oxidant  $[Ru(bpy)_3]^{3+}$  was presented by Karlsson et al. Interestingly, the crystal structure which has been reported by the authors shows dimerization of the complex in the solid state, reminiscent of the tetranuclear cluster of OEC.<sup>[102]</sup> Tetranuclear manganese complex  $[Mn_4O_4(O_2P(Ph)_2)_6]$  having a cubane-like motif was presented in 1997 by Dismukes and coworkers.  $O_2$  evolution under illumination in the gas phase was reported later.<sup>[105,106]</sup> Electrocatalytic water oxidation also has been done with an electrode deposited by Nafion membrane containing ion exchanged  $Mn_4O_4$  complex.<sup>[107]</sup> However recently Hocking et al. showed that, the complex in Nafion matrix serves only as precursor to form manganese oxide nanoparticles as catalytically active species.<sup>[108]</sup>

Metal complexes are suitable to study by using different types of characterization, but their instability during operation is a major problem for their application as practical water oxidation catalyst. Moreover there are some reports showing that these complexes might not be the actual water oxidation catalyst, but only a precursor for the formation of respective metal oxide catalyst.<sup>[96,108]</sup> Metal oxides have long been known to catalyze water oxidation. In 1988, Harriman et al. screened various transition metal oxides as catalyst for water oxidation reaction.<sup>[109]</sup> In this study,  $IrO_2$ ,  $Co_3O_4$ ,  $RuO_2$ ,  $Rh_2O_3$ ,  $Mn_2O_3$  and  $NiCo_2O_4$  showed catalytic activity in presence of a single-electron oxidant  $[Ru(bpy)_3]^{3+}$ , generated by irradiation ( $\lambda > 350$  nm) of  $[Ru(bpy)_3]^{2+}$ . Major advances have been made during the past decade in the preparation and characterization of cheap and

## Results and discussion

---

abundant highly active metal oxide catalysts.<sup>[110–114]</sup> Among them Co, Ni and Mn-containing metal oxides will be discussed below.

### 2.1.1 Co and Ni oxides

In 1980s Parmon et al. as well as Harriman and coworkers reported water oxidation by spinel  $\text{Co}_3\text{O}_4$  cluster.<sup>[109,115]</sup> Later Jiao and Frei presented  $\text{Co}_3\text{O}_4$  nanoparticulate clusters immobilized on a mesoporous silica support as a catalyst for water oxidation.<sup>[116]</sup> The silica support was assumed to stabilize cobalt cluster, which showed no changes after operation for hours, based on XRD and EXAFS data.

Recently electrochemically deposited cobalt oxide films showed promising activity in electrocatalytic water oxidation reaction.<sup>[112]</sup> The prepared material was amorphous, therefore detailed structural information was extracted from x-ray absorption spectroscopy (XAS). Based on the data from XAS, Dau and coworkers proposed a  $\text{Co}^{3+}$  oxo cubane-like structure in which, each Co ion is coordinated to six oxygen atoms. Edge sharing  $\text{CoO}_6$  octahedra are forming single layers containing  $\mu$ -oxido bridged  $\text{Co}^{3+}$  ion. The cubane motifs most likely are connected (corner sharing) to other cubanes in the system. Nocera and his group lately illustrated the potential of Co oxide catalyst to be used in large scale in water splitting devices. They used Co film as the water oxidation catalyst coupled with a photovoltaic made of amorphous silicon in a photochemical cell to perform light-driven water splitting.<sup>[117,118]</sup> Cobalt-substituted ZnO material also has recently been prepared by Driess and coworkers which was used as electrocatalyst for water oxidation reaction.<sup>[119]</sup>

Nickel has long been known to oxidize water in highly pH medium. Several research groups<sup>[120–125]</sup> reported the electrochemical catalytic activity of Ni hydroxide films. Recently electrochemically active nickel-based films were deposited on ITO and FTO electrodes using an aqueous borate electrolyte containing  $\text{Ni}^{2+}$  ions.<sup>[110]</sup> Using a sol-gel method, Sun et al. prepared a thin film of  $\text{NiO}_x$  coated on the n-type Si which acts as efficient photoanodes for solar driven water oxidation.<sup>[126]</sup> The output of this study shows the promising potential of Ni oxide in addition to Co oxide to be used in solar water splitting devices for alternative energy production.

### 2.1.2 Manganese oxides

In 2001 it has been proposed by M. J. Russel and A. J. Hall that, the  $\text{Mn}_4\text{CaO}_5$  cluster of PSII which is the active center responsible for catalysis of water oxidation reaction in all photosynthetic organisms may have been originated from  $\text{MnO}_2$  or Mn minerals formed in the early ocean.<sup>[127]</sup> Ranceiéite ( $\text{CaMn}_4\text{O}_9 \cdot 3\text{H}_2\text{O}$ ) which is a  $\text{MnO}_2$ -based mineral was their suggestion for the source of calcium

manganese cluster of PSII. This particular mineral with layer-type or sandwich structure occurs widely in seafloor manganese-iron nodules, submarine exhales or minerals that have been exposed to weathering in the atmosphere.<sup>[128]</sup> This kind of mineral consists of two dimensional lattices of  $\text{MnO}_2$  with interlayer spaces occupied with cations ( $\text{Ca}^{2+}$  in the case of ranceiéite) and water. The structural analysis showed that the  $\text{MnO}_2$  layers are not perfect meaning that some Mn atom sites are not occupied. This is the place that the exchangeable species in the spacing layers above and below of  $\text{MnO}_2$  layer are bound to. In some minerals, significant number of  $\text{Mn}^{4+}$  ions have been replaced by  $\text{Mn}^{3+}$  ions, which can provide additional places for charge balancing ions such as  $\text{Ca}^{2+}$ .<sup>[128]</sup>

Some years before this proposal from Russel and Hall, in the late 1970, Morita et al. prepared Mn oxide electrodes, which were electrochemically active in water splitting reaction.<sup>[129]</sup> They deposited a mixture of  $\text{Mn}_2\text{O}_3$  and  $\beta\text{-MnO}_2$  via thermal decomposition of manganese nitrate. The electrochemical activity tests were carried out in acidic as well as basic medium. It was reported that the electrode performance depends on the pH of the electrolyte and the Mn oxide phase. In detail, they showed better catalytic activity in basic media than acidic one and electrodes with manganese oxides consisting of mixture of  $\beta\text{-MnO}_2$  and  $\text{Mn}_2\text{O}_3$  were better catalyst than the ones with pure  $\beta\text{-MnO}_2$ .<sup>[129]</sup> Speccia et al. deposited  $\text{MnO}_x$  nanorods with different morphology by varying the acidity of the applied electrolyte. Performing the water oxidation reaction in basic medium revealed that, films predominantly containing  $\text{Mn}_2\text{O}_3$  and birnessite-like phase show the highest catalytic activity while the ones with more  $\text{Mn}_3\text{O}_4$  phase were almost inactive.<sup>[130]</sup>

Recently several groups reported on the chemical water oxidation by manganese oxide as catalyst, either in presence or absence of light.  $\lambda\text{-MnO}_2$ <sup>[131]</sup>,  $\alpha\text{-MnO}_2$ <sup>[132]</sup> nanowires and nanotubes as well as  $\beta\text{-MnO}_2$  nanowires, nanosized  $\alpha\text{-Mn}_2\text{O}_3$ <sup>[133]</sup> and amorphous manganese oxide<sup>[134]</sup> are examples of such catalysts. Najafpour et al. presented a nanosized, soluble  $\text{Mn}^{4+}$  oxide colloid which showed catalytic activity in presence of chemical oxidants such as  $\text{H}_2\text{O}_2$ , oxone,  $\text{Ce}^{4+}$  and  $[\text{Ru}(\text{bpy})_3]^{3+}$ .<sup>[135]</sup> Frei and coworkers developed an efficient water oxidation catalyst consisting of highly dispersed manganese oxide nanostructures on silica.<sup>[116]</sup> It has been postulated that the silica framework provides a stable support and high dispersion, which result in sustainable catalytic activity. Dismukes and coworkers developed a nanoparticulate  $\lambda\text{-MnO}_2$  via a novel strategy named delithiation of inactive  $\text{LiMn}_2\text{O}_4$ . The manganese oxide which has been prepared by delithiation route is an efficient catalyst when tested at pH=5.8 with  $[\text{Ru}(\text{bpy})_3]$  as photosensitizer, light and  $\text{Na}_2\text{S}_2\text{O}_8$  as an electron acceptor.<sup>[136]</sup>

Pure polymorphs of manganese oxides also were prepared by the same group and different structural factors which can affect catalytic activity of the oxides were studied.<sup>[137]</sup> They found out that the most active material all contain  $\text{Mn}^{3+}$  in edge-sharing octahedra. It was therefore hypothesized that  $\text{Mn}^{3+}\text{-O}$  in edge-sharing octahedra at the surface are more catalytically active due

to the longer (Jahn-Teller distorted) and more flexible Mn-O bond than  $\text{Mn}^{4+}$ -O. Recently Driess and coworkers reported the formation of highly active water oxidation catalyst through the partial corrosion of nanostructured MnO particles.<sup>[138]</sup> Using different analytical techniques they have been able to show that MnO nanostructures act as a precursor, which is transformed into an active mixed valant  $\text{MnO}_x$  catalyst in presence of cerium ammonium nitrate as an oxidant.

Calcium manganese oxides were also investigated, inspired by the catalytic activity of manganese oxides as well as the composition of the OEC. It has been shown by Kurz et al.<sup>[89]</sup> and others<sup>[139]</sup> that incorporation of calcium ions into manganese oxide structure can improve their catalytic activity.

### 2.2 Synthesis and characterization of porous CaMn oxides

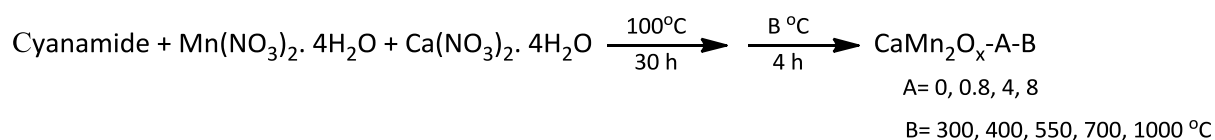
In heterogeneous catalysis, porosity of the solid phase is essential, because it provides a high surface area for catalysis and good accessibility to the active sites. Recently, Kailasam et al. presented a pathway to prepare highly porous silica in a one-step approach by adding cyanamide to a silica precursor solution, subsequent gelation and heat treatment of this mixture. Heat treatment of cyanamide yields, over several polycondensation steps, a polymeric carbon nitride, which acted as hard template to create the porosity in the silica.<sup>[140]</sup> Herein we used a comparable approach, namely mixing CaMn oxide precursors with cyanamide and additional heat treatment. However, here the organic porogen decomposed already at lower temperatures leaving behind a porous, foam-like CaMn oxide.

Some metal oxides nanostructures were previously prepared by using urea as fuel and metal nitrate as oxidizing material via combustion reaction.<sup>[141,142]</sup> High temperature of the reaction makes urea to decompose into  $\text{CO}_2$  and  $\text{NH}_3$  gasses and leave nanoparticle/porous metal oxide behind. It has been described before, that upon thermal treatment, cyanamide transforms via several condensation steps into dicyandiamide, melamine, melem and finally into melon, a polymeric carbon nitride.<sup>[143,144]</sup> Such polymeric carbon nitrides are just formed at temperatures as high as 550 °C and have recently gained increasing interest for their application as photocatalyst.<sup>[144]</sup> Decomposition of such carbon nitrides finally occurs at around 650 °C. However in the present system no formation of a polymeric carbon nitride was observed at temperatures above 300 °C.

Similar to previous works of Kurz<sup>[89]</sup> and Shilov<sup>[145]</sup> we used simple  $\text{Mn}^{2+}$  and  $\text{Ca}^{2+}$  salts as precursors (Scheme 2.1). However in our synthetic route we do not add an oxidant ( $\text{MnO}_4^-$ ). Instead heating the CaMn mixture in presence of oxygen induces oxidation of Mn. When no cyanamide is added (e.g.  $\text{CaMn}_2\text{O}_x$ -0-550), a non-porous mixture of crystalline phases is formed, which just showed very low catalytic activity for water oxidation. However, the addition of cyanamide yields materials with

## Results and discussion

increased surface area and strongly affects the atomic structure of the formed oxides, which eventually results in the formation of highly active catalysts. Different cyanamide/metal ratios and calcination temperatures (300-1000 °C) were applied in order to study their effect on the structure and catalytic activity of formed metal oxides.



**Scheme 2.1: Synthetic route for preparation of CaMn oxides.**

**Table 2.1: Characterization of oxides prepared at different calcination temperatures.**

Catalyst	$S_{\text{BET}}^{\text{a}}$	Oxygen evolution rate <sup>b</sup>	Crystal Size <sup>c</sup>	Oxidation state	Parent phase
CaMn <sub>2</sub> O <sub>x</sub> -0.8-300	0.2	0.011	Amorphous	2.1 <sup>e</sup>	Mn <sup>2+</sup> and Ca <sup>2+</sup> in amorphous organic matrix
CaMn <sub>2</sub> O <sub>x</sub> -0.8-400	130.0	3.000/0.420 <sup>g</sup>	Amorphous, <5 <sup>d</sup>	3.6 <sup>e</sup>	Layer-type CaMn <sub>2</sub> <sup>3+/4+</sup> oxide,
CaMn <sub>2</sub> O <sub>x</sub> -0.8-550	62.0	0.620	5-18	3.7 <sup>e</sup>	similar Ca <sub>2</sub> Mn <sub>3</sub> O <sub>8</sub>
CaMn <sub>2</sub> O <sub>x</sub> -0.8-700	19.0	0.082	17-53	3.8 <sup>e</sup>	Ca <sub>2</sub> Mn <sub>3</sub> O <sub>8</sub>
CaMn <sub>2</sub> O <sub>x</sub> -0.8-1000	3.3	0.018	40-93	3.0 <sup>f</sup>	CaMn <sub>2</sub> O <sub>4</sub> (marokite)
Mn <sub>2</sub> O <sub>3</sub> -0.8-550	36.0	0.100	15-38	3.0 <sup>f</sup>	Mn <sub>2</sub> O <sub>3</sub>

<sup>a</sup>Surface area of oxides ( m<sup>2</sup>.g<sup>-1</sup>), <sup>b</sup>oxygen evolution rate (mmolO<sub>2</sub>.molMn<sup>-1</sup>.s<sup>-1</sup>) in presence of [Ce<sup>4+</sup>]= 0.5 M,

<sup>c</sup>Crystal size (nm) calculated based on Scherrer equation of XRD peaks, <sup>d</sup>Crystal or particle size as estimated from (HR)TEM image, <sup>e</sup>Oxidation state based on XANES data, <sup>f</sup>Oxidation state as deduced from XRD results (Fig. 2.4 and 6.4.), <sup>g</sup>Oxygen evolution rate (mmolO<sub>2</sub>.molMn<sup>-1</sup>.s<sup>-1</sup>) in presence of [Ce<sup>4+</sup>]= 0.5 M resulted from long-term measurement by gas chromatography (Fig. 2.13).

## Results and discussion

**Table 2.2: Characterization of the oxides prepared with different amount of cyanamide.**

Catalyst	$S_{\text{BET}}^{\text{a}}$	Oxygen evolution rate <sup>b</sup>	Crystal Size <sup>c</sup>	Oxidation state	Parent phase
CaMn <sub>2</sub> O <sub>x</sub> -8-550	46.0	0.140	11-39	-	Ca <sub>2</sub> Mn <sub>3</sub> O <sub>8</sub>
CaMn <sub>2</sub> O <sub>x</sub> -4-550	51.0	0.220	7-27	-	Ca <sub>2</sub> Mn <sub>3</sub> O <sub>8</sub>
CaMn <sub>2</sub> O <sub>x</sub> -0.8-550	62.0	0.620	5-18	3.7 <sup>d</sup>	Ca <sub>2</sub> Mn <sub>3</sub> O <sub>8</sub>
CaMn <sub>2</sub> O <sub>x</sub> -0-550	3.9	0.029	16-66	3.9 <sup>e</sup>	mixture of oxide phases <sup>f</sup>

<sup>a</sup>Surface area of oxides ( $\text{m}^2 \cdot \text{g}^{-1}$ ), <sup>b</sup> oxygen evolution rate ( $\text{mmolO}_2 \cdot \text{molMn}^{-1} \cdot \text{s}^{-1}$ ) in presence of  $[\text{Ce}^{4+}] = 0.5 \text{ M}$ , <sup>c</sup>Crystal size (nm) calculated based on Scherrer equation of XRD peaks, <sup>d</sup>Oxidation state based on XANES data, <sup>e</sup>Oxidation state as deduced from XRD results (Fig. 2.4), <sup>f</sup>XRD reflections were assigned to MnO<sub>2</sub>, Mn<sub>2</sub>O<sub>3</sub>, Ca<sub>2</sub>MnO<sub>4</sub>, and CaO; alternative assignments are not excluded.

Indeed thermogravimetric analysis (Fig. 2.1) and elemental analysis showed that only in the sample prepared at 300 °C (CaMn<sub>2</sub>O<sub>x</sub>-0.8-300) a considerable amount of organic moieties can be found, while already at 400 °C (CaMn<sub>2</sub>O<sub>x</sub>-0.8-400) only minor contributions of carbon and nitrogen residues are detectable (N%: 0.8, C%: 1.9) suggesting that the formed CaMn oxide accelerates decomposition of the carbon nitride precursors drastically. TGA measurement of the oxide heated to low temperature (300°C) also show considerable weight losses due to organic phase decomposition. The weight loss of CaMn<sub>2</sub>O<sub>x</sub>-0.8-400 in the temperature range of 300-400 °C, can be explained by the loss of water weakly bound to the oxide layers. Further weight loss in the range of 400 °C to 1000 °C can be explained by phase transition with oxygen release e.g. by reduction of manganese from Mn<sup>4+</sup> to Mn<sup>3+</sup> and finally Mn<sup>2+</sup>.<sup>[146]</sup>

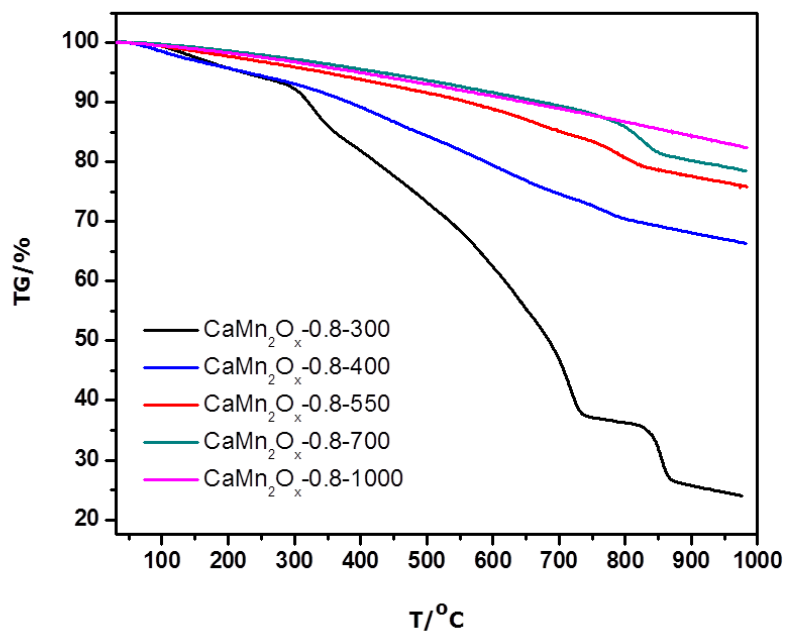


Fig. 2.1: TGA curves for the thermal decomposition of CaMn oxides (in ambient condition at a temperature range of 30-1000 °C with the heating rate of 10 °C/min.).

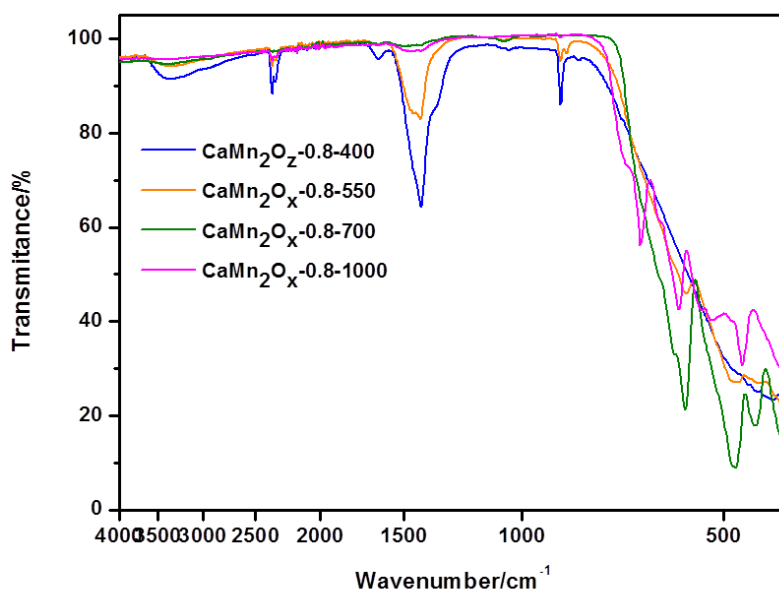


Fig. 2.2: IR spectra of calcium manganese oxides.

## Results and discussion

---

In the infrared (IR) spectra (Fig. 2.2), broad bands around  $3300\text{ cm}^{-1}$  and  $1640\text{ cm}^{-1}$  are assignable to O-H stretching and H-O-H bending mode vibrations of water. They are especially pronounced in  $\text{CaMn}_2\text{O}_x\text{-0.8-400}$ , confirming the presence of sizeable amounts of water. The vibrational modes of the  $\text{MnO}_6$  units expand over the  $700\text{-}400\text{ cm}^{-1}$  region, as expected for Mn oxides.<sup>[147]</sup>

ICP-OES was carried out to determine the calcium and manganese content of the oxides and showed that the Ca:Mn ratio in calcium manganese oxides remained unchanged during the preparation process (Ca:Mn $\sim$  1:2) (Table 6.1 and 6.2).

X-ray powder diffraction (XRD) was used to identify the formed oxide phases. Fig. 2.3 shows the XRD patterns of samples produced with constant amount of cyanamide but different calcination temperatures ( $\text{CaMn}_2\text{O}_x\text{-0.8-B}$ ). The oxide heated to  $300\text{ }^\circ\text{C}$  is completely XRD amorphous. By heating the sample to  $400\text{ }^\circ\text{C}$ , a broad peak of low intensity at  $2\theta=29.4^\circ$  may be observable, which cannot be assigned to any known phase. Partial crystallization (lowered amorphicity) of the samples is observed for oxides heated to  $550\text{ }^\circ\text{C}$ . At  $700\text{ }^\circ\text{C}$ , the XRD peaks become more intense and can be finally assigned to a layered  $\text{Ca}_2\text{Mn}_3\text{O}_8$  structure (Fig. 2.4).<sup>[148,149]</sup> Further heating to  $1000\text{ }^\circ\text{C}$  yielded a complete phase change from  $\text{Ca}_2\text{Mn}_3\text{O}_8$  to  $\text{CaMn}_2\text{O}_4$  (Fig. 2.4).

XRD patterns of the oxides heated to  $550\text{ }^\circ\text{C}$  and prepared with different amount of cyanamide are shown in Fig. 2.3 ( $\text{CaMn}_2\text{O}_x\text{-A-550}$ ). All patterns point toward the presence of  $\text{Ca}_2\text{Mn}_3\text{O}_8$ , however the broad peaks again point to a high level of amorphicity.

The broad XRD peaks are explainable either by very small crystallites (see 'crystal size' in Tables 2.1 and 2.2) or by structural disorder (amorphicity) at the atomic level resulting, e.g., from a high number of defect sites or lack of a well-defined unit cell. The XRD pattern generally reflects the pair distribution function (PDF) of the atoms in the diffracting material. For ideal XRD data, the PDF can be obtained directly from the XRD pattern by appropriate Fourier transformation. For non-crystalline samples of limited long-range order, broad reflections may be observable which are assignable to the 'parent structure' of a crystalline material. Accordingly we suggest that the temperature increase from  $400\text{ }^\circ\text{C}$  via  $550\text{ }^\circ\text{C}$  to  $700\text{ }^\circ\text{C}$  results in increasing similarity of the material to the same parent structure, namely  $\text{Ca}_2\text{Mn}_3\text{O}_8$  (Fig. 2.4). This suggestion is supported by the EXAFS data presented further in the section 2.2.2.2 (Here and in the following, we use the term 'parent structure' to denote a crystalline material that contains a set of structural motifs also found in the amorphous materials. In the amorphous material however, mixed oxidation states, the presence of water molecules, and other factors result in a low degree of order such that the structural motifs of the parent structure become less prominent.)

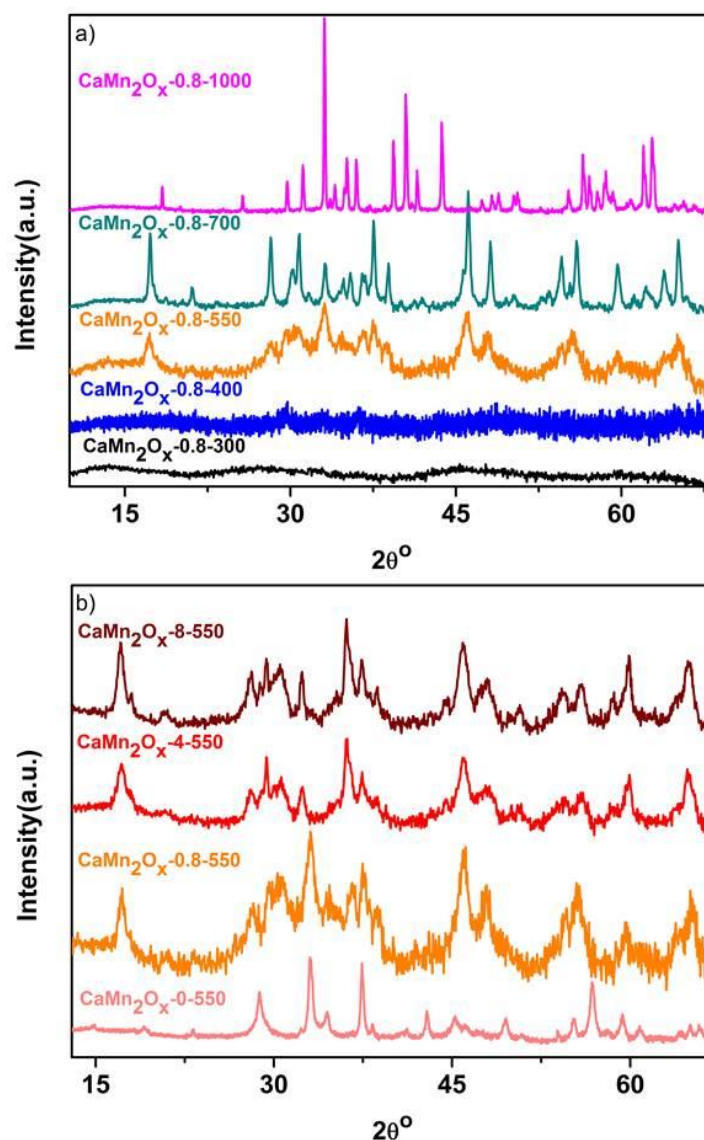
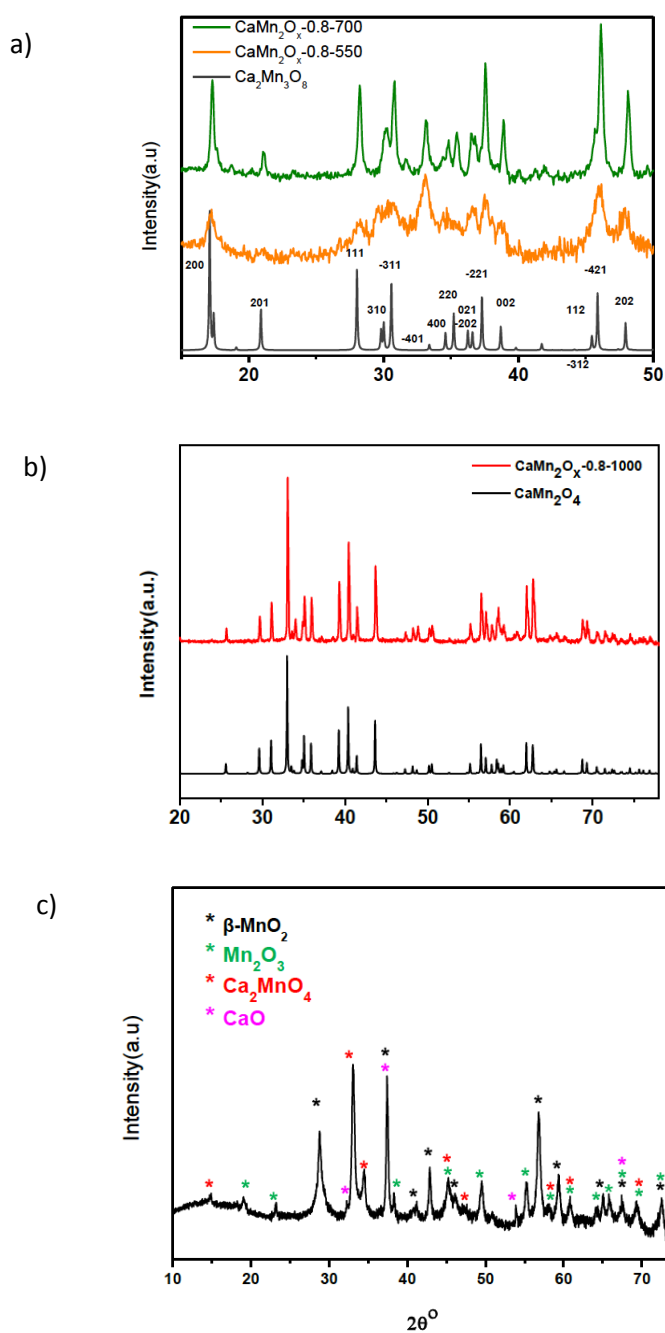


Fig. 2.1: XRD patterns of a) CaMn<sub>2</sub>O<sub>x</sub>-0.8-B calcined at different temperatures and b) CaMn<sub>2</sub>O<sub>x</sub>-A-550 prepared with different amount of cyanamide porogen.

As visible in Fig. 2.3, more intense but still broadened peaks for the layered Ca<sub>2</sub>Mn<sub>3</sub>O<sub>8</sub> are observed with increasing amount of cyanamide. Alternatively, when no cyanamide was added (CaMn<sub>2</sub>O<sub>x</sub>-0-550) the formation of Ca<sub>2</sub>Mn<sub>3</sub>O<sub>8</sub> is not observed anymore. Instead reflections assignable to different Mn and Ca oxide phases or parent structures are observed (Fig. 2.4). Heating materials to 1000 °C causes a complete phase change to marokite (CaMn<sub>2</sub>O<sub>4</sub>) (Fig. 2.4). XRD analysis thus shows that the addition of cyanamide to the precursor mixture not only introduces porosity (see below) but also is responsible for a phase change of the CaMn oxides during heat treatment. In Fig 2.4 c, the stars label reflections that are found in crystalline calcium and manganese oxides at similar diffraction angles.



**Fig. 2.2:** XRD patterns of a)  $\text{CaMn}_2\text{O}_x-0.8-550$ , 700 and reflections expected for  $\text{Ca}_2\text{Mn}_3\text{O}_8$ , b) XRD patterns of  $\text{CaMn}_2\text{O}_x-0.8-1000$  and the reflections expected for Marokite and c) XRD patterns of  $\text{CaMn}_2\text{O}_x-0-550$ .

We note that this assignment does not necessarily mean that there is a phase separation involving four distinct oxide phases. For amorphous materials, the XRD pattern reflects the pair distribution function (as obtained by appropriate Fourier-transformation of the XRD pattern); a single amorphous phase may be characterized by reflections of several parent structures.

## Results and discussion

---

Calcium manganese oxides have been prepared without addition of cyanamide.<sup>[89]</sup> These oxides showed long range metal-metal interaction at 400 °C and even at 60 °C which indicates the formation of pre-ordered structures already at low temperature.<sup>[150]</sup> In the herein described protocol, cyanamide condensation forms an organic framework below 400 °C and metal ions are at this stage most likely coordinated to the building blocks of the framework (Tri-s-triazines, melamine, etc.). This results in their spatial separation and therefore inhibition of formation of any specific oxide phase. In fact, no long-range metal-metal interaction can be found in the composites until the calcination temperature approaches 550 °C. By heating the sample to 400 °C the organic network decomposes and a calcium manganese oxide with highly disordered nature is formed, proven by XRD and XAS (Section 2.2.2). Thus the formation of different phases of CaMn oxide with and without cyanamide might be explained by the very different temperatures at which first formation of long-range order and eventually crystallization occurs.

Transmission electron microscopy (TEM) was used to reveal the structure of the materials (Fig. 2.5, 2.9, and 2.10).  $\text{CaMn}_2\text{O}_x\text{-0.8-300}$  shows no distinct features, but a rather intimate mixture between CaMn oxide and carbon nitride precursors at this temperature. As mentioned before, between 300 °C and 400 °C the organic phase disappears forming gaseous decomposition products and nearly pure CaMn oxide remains. Indeed  $\text{CaMn}_2\text{O}_x\text{-0.8-400}$  shows a foam-like structure as it is typically observed in polymers when gaseous products are formed during polymerization. The porous structure becomes denser, with an average decrease in pore size that may be due to the reduced amorphicity and water loss of the material resulting in structural contraction. At 700 °C the foam or porous structure completely disappears and instead larger particles are observed. The foam structure can be also observed by SEM measurements (Fig. 2.5 and 2.6). When heated to 550 °C, the porous structure becomes denser, with an average decrease in pore size that may be due to the reduced amorphicity and water loss of the material resulting in structural contraction (Fig. 2.7). At 700 °C the foam or porous structure completely disappears and instead larger particles are observed (Fig. 2.8). EDS-mapping images (Fig. 2.6, Fig. 2.7 and Fig. 2.8) prove a homogenous distribution of calcium, manganese and oxygen within all the samples calcinated at temperatures above 300 °C, rendering a phase separation, e.g., between one calcium oxide and one or more manganese oxides unlikely.

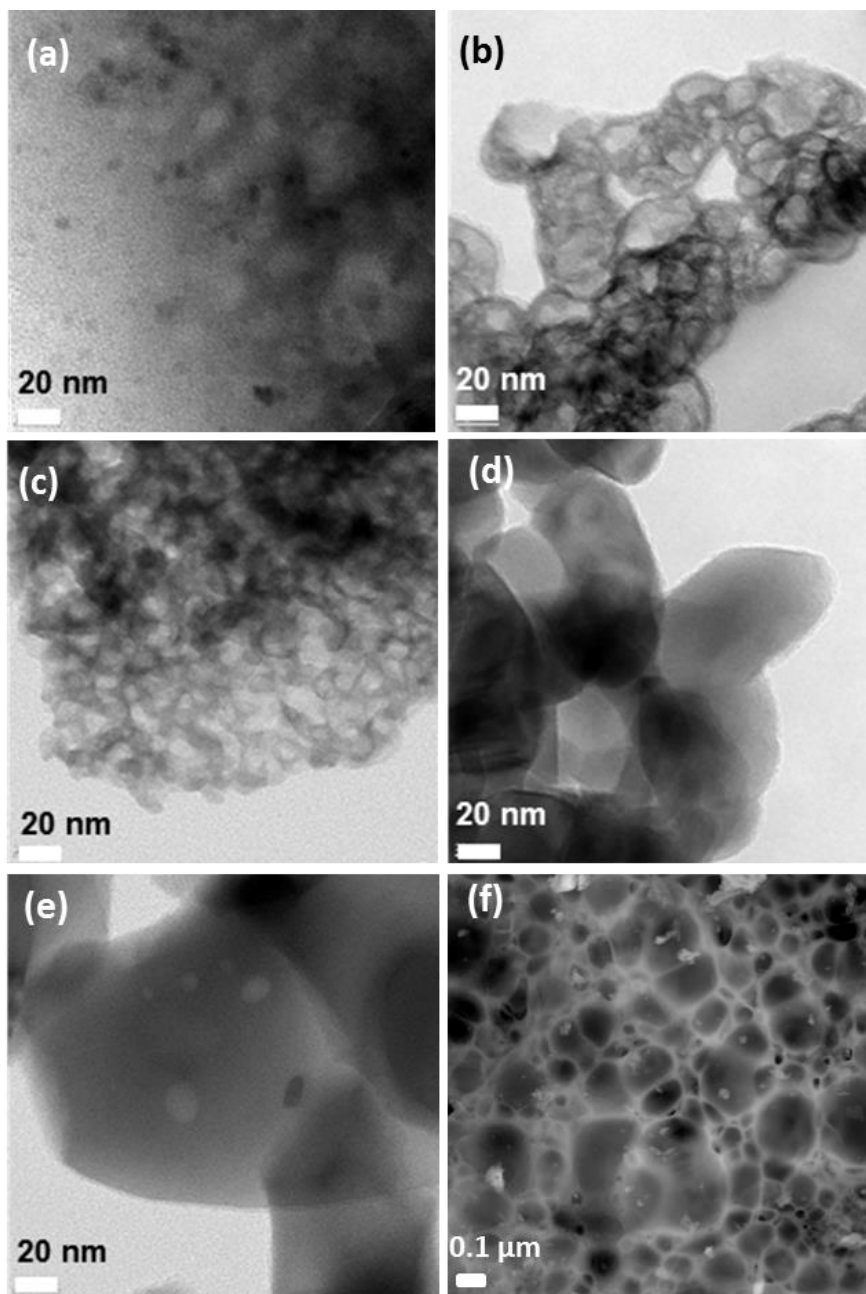


**Fig. 2.3:** (a-e)TEM images of calcium manganese oxide samples which were calcined at a) 300 °C, b) 400 °C, c) 550 °C, d) 700 °C, e) 1000 °C, f) SEM images of CaMn<sub>2</sub>O<sub>x-0.8-400</sub>.

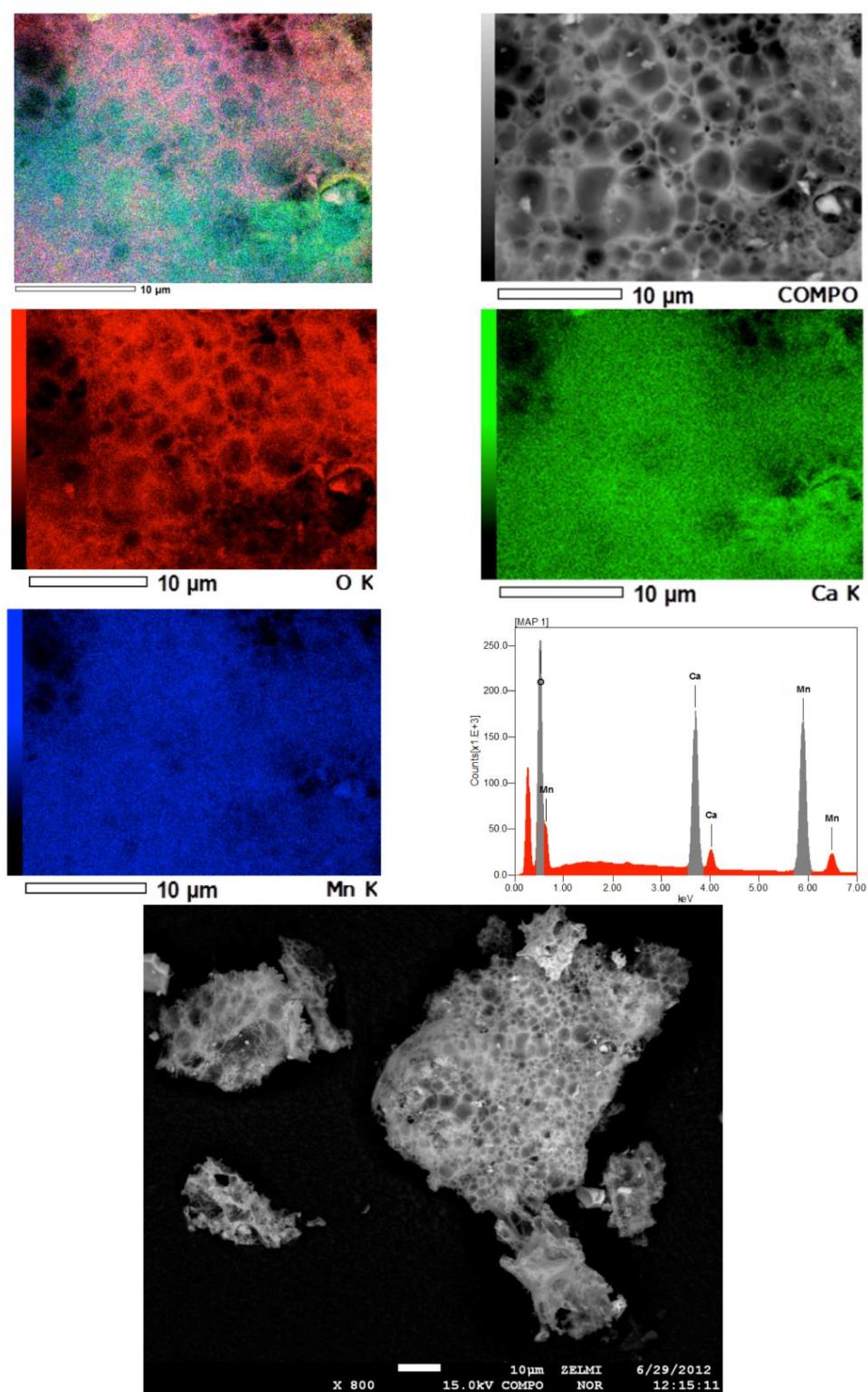


Fig. 2.4: SEM image and EDS-mapping of  $\text{CaMn}_2\text{O}_x-0.8-400$ .

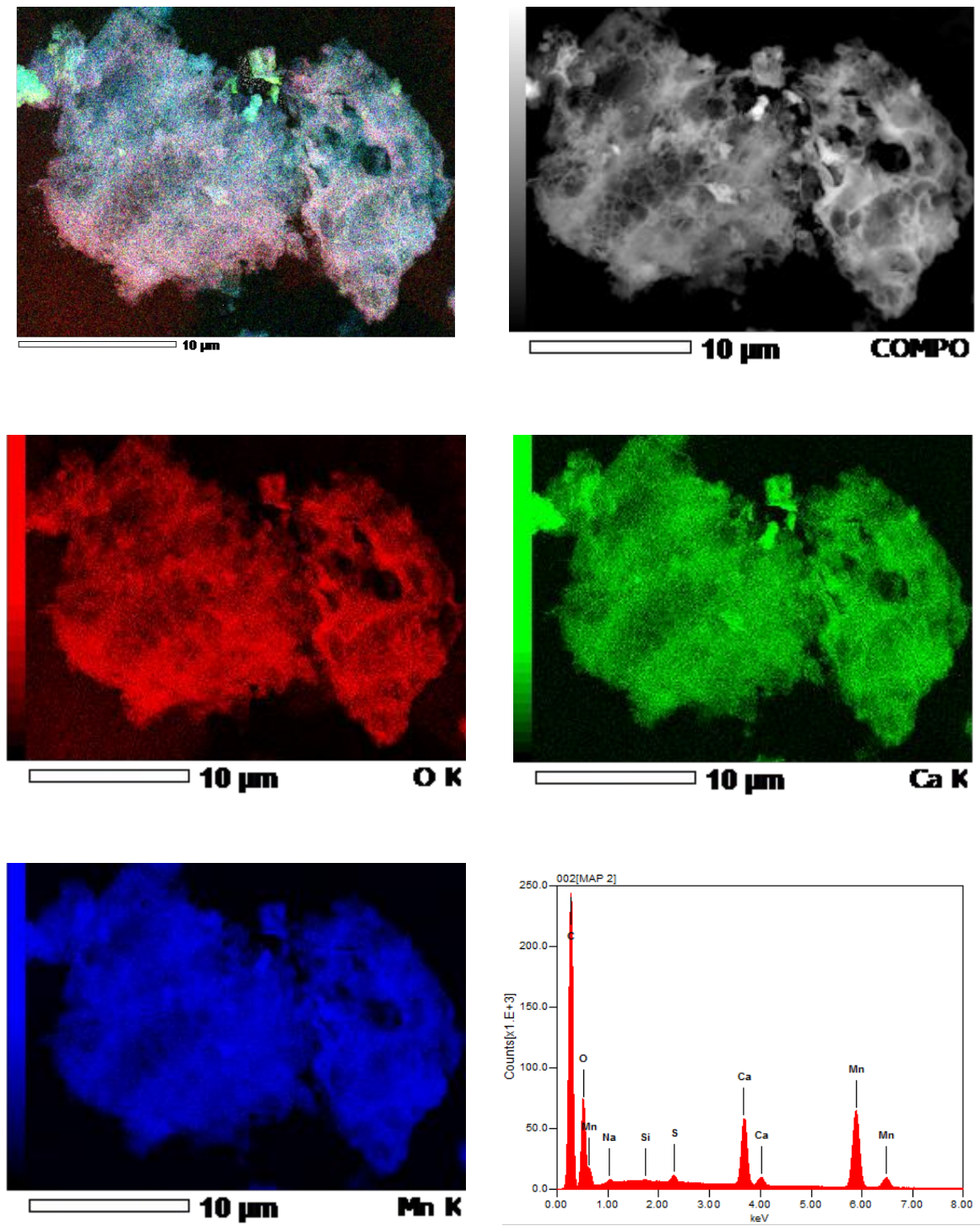


Fig. 2.5: SEM image and EDS-mapping images of  $\text{CaMn}_2\text{O}_x-0.8-550$ .

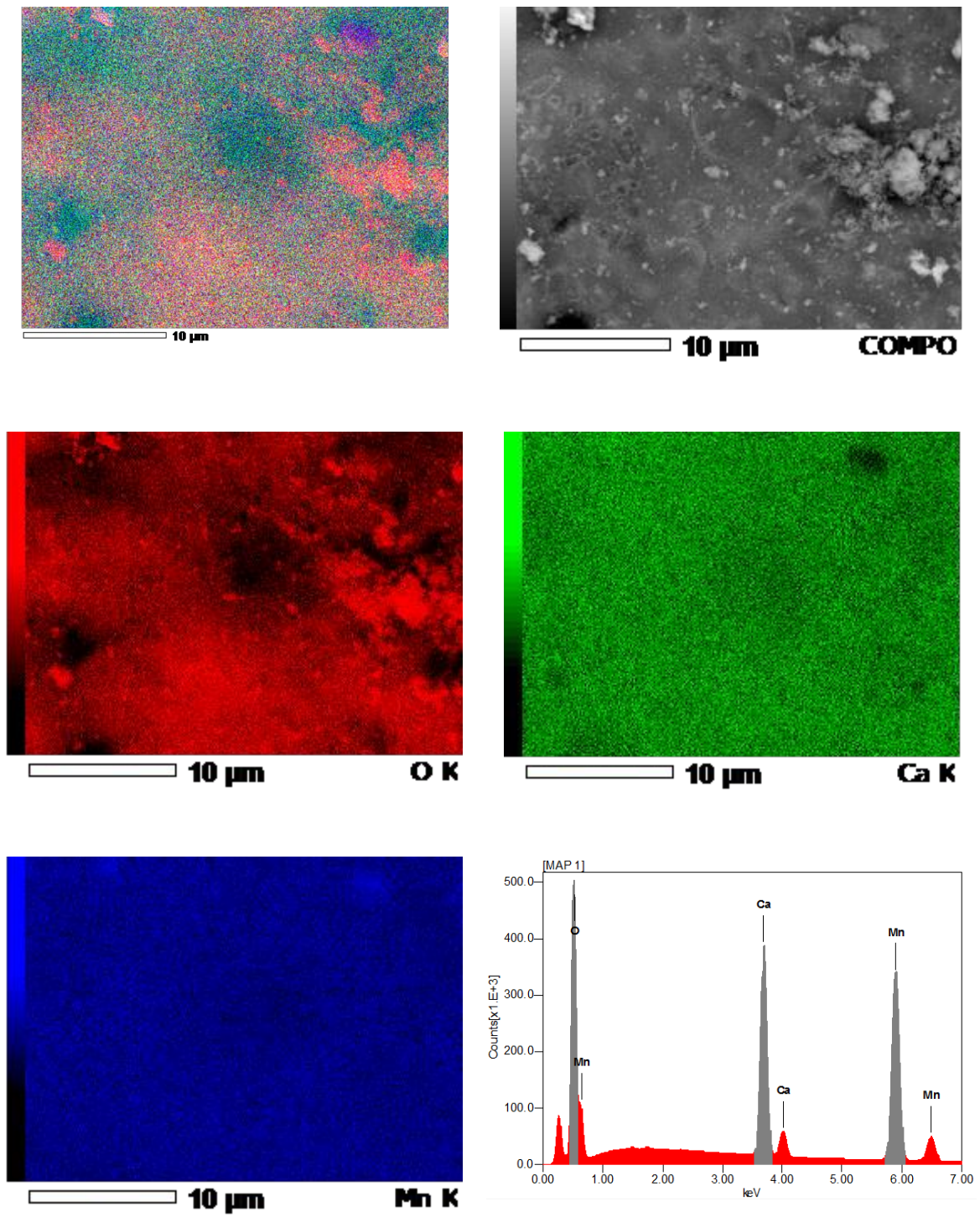
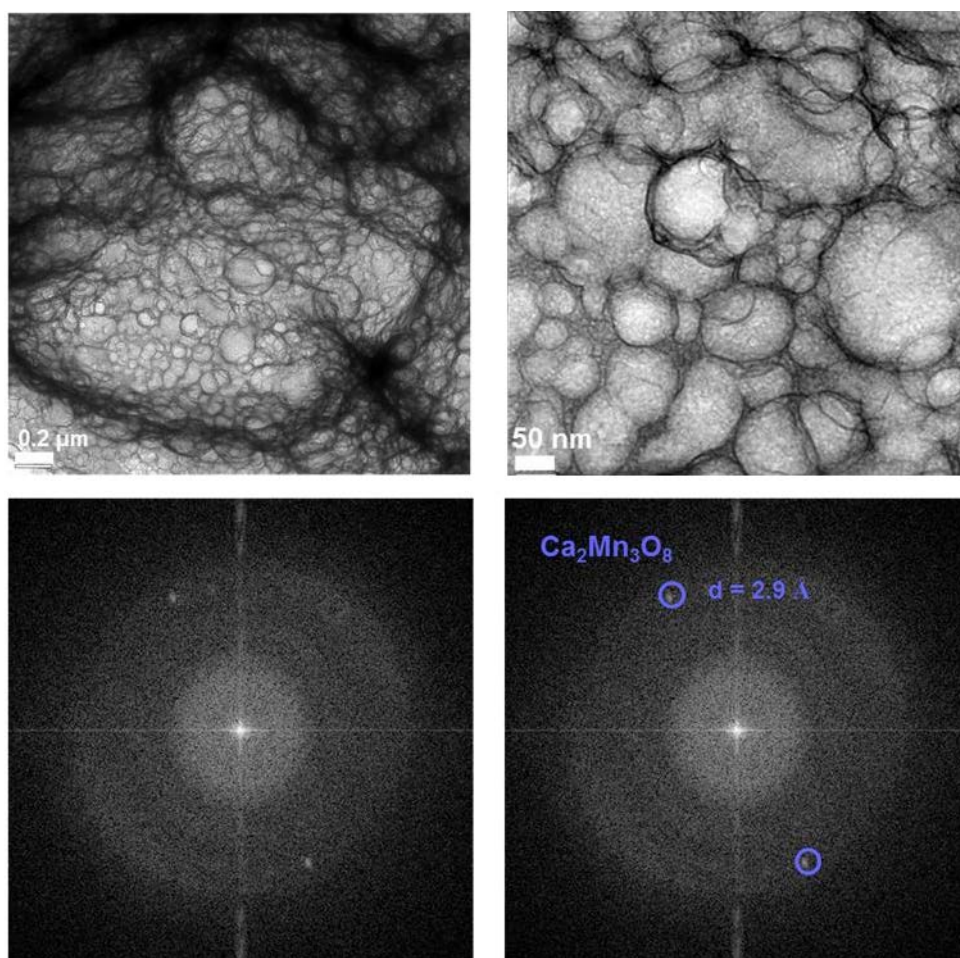


Fig. 2.6: SEM image and EDS-mapping images of  $\text{CaMn}_2\text{O}_x-0.8-700$ .

## Results and discussion

While in the XRD no reflections are observed for  $\text{CaMn}_2\text{O}_x$ -0.8-400, (HR)TEM images analyzed by Fast Fourier-Transformation reveal a diffuse diffraction ring and weak diffraction reflexes corresponding to d-values of  $\text{Ca}_2\text{Mn}_3\text{O}_8$  phase (Fig. 2.9). The d-value of 2.9 Å is in agreement with the EXAFS results (See section 2.2.2.2) revealing a prominent Mn-Mn distance of 2.87 Å. (HR)TEM images of the samples  $\text{CaMn}_2\text{O}_x$ -0.8-550 and  $\text{CaMn}_2\text{O}_x$ -0.8-700 confirm the XRD results; they suggest the presence of a layered  $\text{Ca}_2\text{Mn}_3\text{O}_8$  (parent) structure (Fig. 2.10). This structure can be described as vacancy-containing sheets of edge-sharing  $\text{MnO}_6$  octahedra which are interconnected by  $\text{Ca}^{2+}$  ions<sup>[148,149]</sup> (Fig. 2.11).



**Fig. 2.7:** (HR)TEM images and FFTs of  $\text{CaMn}_2\text{O}_x$ -0.8-400 which shows d-values corresponding to  $\text{Ca}_2\text{Mn}_3\text{O}_8$  (hkl=-311).

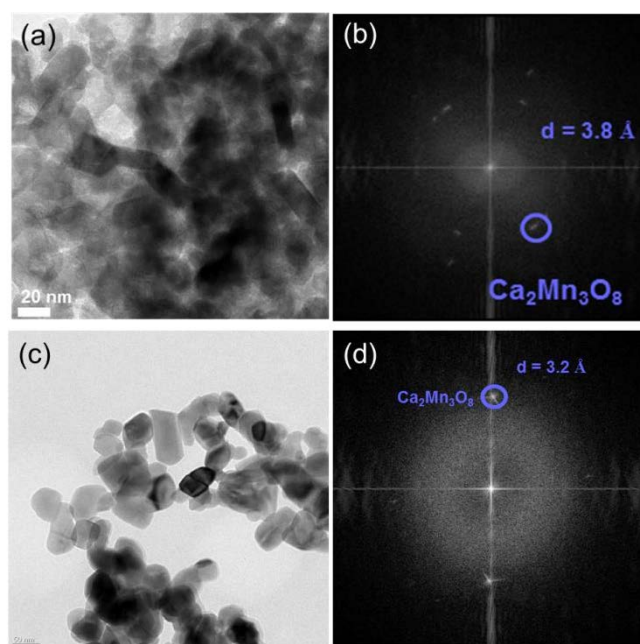


Fig. 2.8: TEM images and FFTs of a,b)  $\text{CaMn}_2\text{O}_x-0.8-550$  which shows d-values corresponding to  $\text{Ca}_2\text{Mn}_3\text{O}_8$  ( $hkl=-111$ ) and c,d)  $\text{CaMn}_2\text{O}_x-0.8-700$  with d-values corresponding to  $\text{Ca}_2\text{Mn}_3\text{O}_8$  ( $hkl=111$ ).

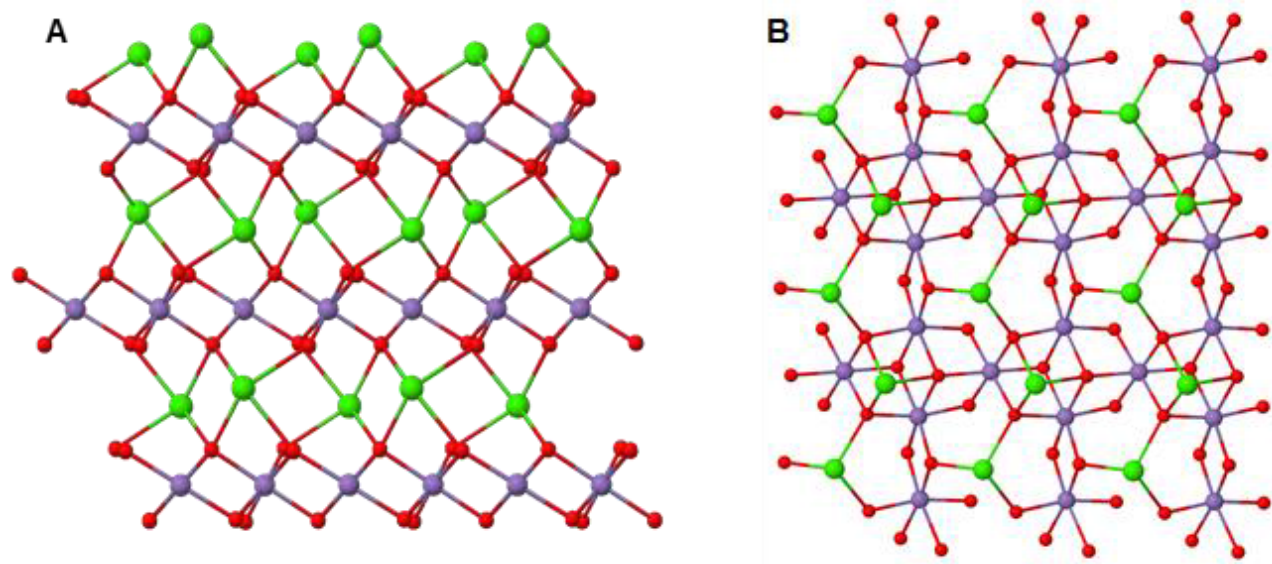


Fig. 2.9: Structure of  $\text{Ca}_2\text{Mn}_3\text{O}_8$ . A – side view in which the  $\text{MnO}_6$  layers of edge-sharing octahedral and the Ca ions connecting  $\text{MnO}_6$  layers are visible. B – top view illustrating the two binding positions of Ca: I) on the top of Mn vacancies ( $3.7 \text{ \AA}$  Mn-Ca distance) and II) in a cubane motif ( $3.3 \text{ \AA}$  Mn-Ca distance). Mn atoms are shown in magenta, Ca in green, and O in red.

Nitrogen sorption experiments showed that the herein presented preparation method resulted in oxides with increased surface areas (Tables 2.1. and 2.2). While from the pure Ca and Mn salts, Ca-Mn oxides (e.g.  $\text{CaMn}_2\text{O}_x$ -0-550) with lower outer surface areas ( $\sim 4 \text{ m}^2 \cdot \text{g}^{-1}$ ) are observed, addition of cyanamide yields surface areas up to  $130 \text{ m}^2 \cdot \text{g}^{-1}$  for  $\text{CaMn}_2\text{O}_x$ -0.8-400 and  $62 \text{ m}^2 \cdot \text{g}^{-1}$  for  $\text{CaMn}_2\text{O}_x$ -0.8-550. The chosen amount of 0.8 g cyanamide seems to be optimal for creating the porous structure, as a further increase does not yield higher surface areas for the samples prepared at 550 °C. A higher amount of template of course yields thinner pore walls in the replica. Thus, when a certain cyanamide/metal ratio is reached, structural collapse and a decrease in the overall surface area can be observed. As confirmed by electron microscopy measurements, the porosity of the samples collapsed when prepared with higher amounts of cyanamide (Fig 6.1) or at higher temperatures, i.e. at 700 °C and 1000 °C (Fig. 2.5) and consequently lower surface areas and porosities are observed.

We note that the achieved surface area of  $130 \text{ m}^2 \cdot \text{g}^{-1}$  for  $\text{CaMn}_2\text{O}_x$ -0.8-400 is still lower than the surface area of previously reported CaMn oxides<sup>[89]</sup> with surface areas of  $205 \text{ m}^2 \cdot \text{g}^{-1}$  or  $303 \text{ m}^2 \cdot \text{g}^{-1}$ . In spite of the lower surface areas, the CaMn oxides described herein excel by clearly higher oxygen evolution activity, as discussed in the following (Table 6.3).

### 2.2.1 Calcium manganese oxides as water oxidation catalysts

Water-oxidation experiments were carried out in the presence of a non-oxygen transfer oxidizing agent, cerium ammonium nitrate, to investigate the catalytic activity of the oxides (Fig. 2.12, Table 2.1 and 2.2).  $\text{Ce}^{4+}$  is a single electron oxidant with a high oxidation potential ( $\text{Ce}^{4+}/\text{Ce}^{3+}$ ,  $E_0 \sim +1.4 \text{ V}$  vs. NHE) suitable for water oxidation. It has been proven by  $^{18}\text{O}$ -labelling experiments that reactions in which  $\text{Ce}^{4+}$  act as an oxidant and manganese oxides as catalysts are “real” water-oxidation processes as bulk water provides both oxygen atoms of the produced  $\text{O}_2$ .<sup>[134,151]</sup> Our experiments were conducted in 2 ml deoxygenated aqueous solutions containing the CaMn oxide and cerium ammonium nitrate. A Clark-type electrode was used for the detection of dissolved oxygen produced in these solutions. Fig. 2.12 shows the dissolved oxygen content in the solutions at room temperature. All compounds are active for water-oxidation while  $\text{CaMn}_2\text{O}_x$ -0.8-400 is by far the most active one showing a rate of  $3 \text{ mmol O}_2 \text{ mol Mn}^{-1} \text{ s}^{-1}$ . Furthermore, long-term oxygen evolution (Fig. 2.13) and stability test with gas chromatography showed that  $\text{CaMn}_2\text{O}_x$ -0.8-400 is active for extended time periods under harsh conditions (60 h, pH  $\sim 1$ ) and without any further treatment like washing with calcium containing solution<sup>[139]</sup>, can produce oxygen in second and third run at almost the same rate (Fig. 6.2). TEM images and XRD patterns (after three catalytic run with the same catalyst) showed

that amorphous nature of the catalyst and foam-like morphology maintained (Fig. 6.3 and 6.4) while its surface area has been increased from 130 to 180  $\text{m}^2\cdot\text{g}^{-1}$ .

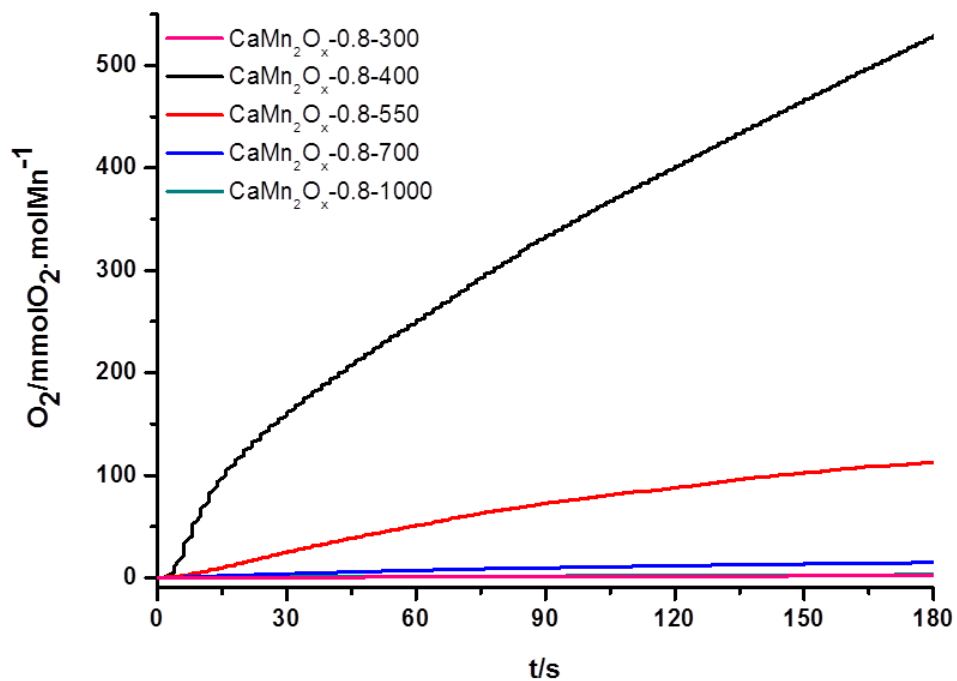
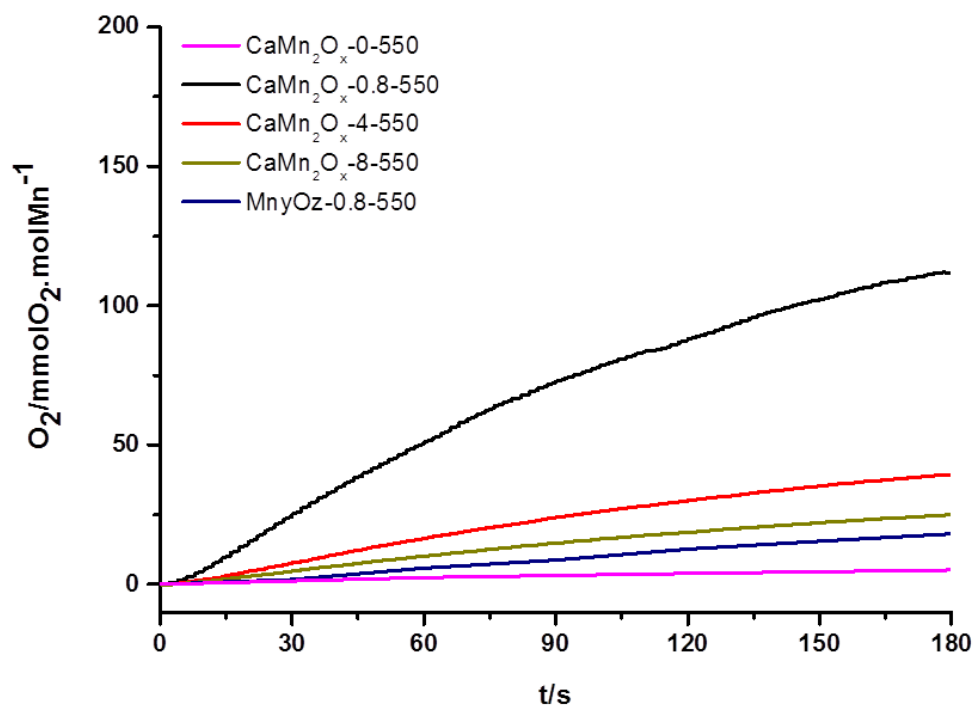


Fig. 2.10: Oxygen evolution in 0.5 M aqueous Ce<sup>4+</sup> solution.

## Results and discussion

The same phenomenon (increase in surface area) was observed in the active mixed-valant  $\text{MnO}_x$  catalyst which has been formed through partial oxidation (corrosion) of nonactive  $\text{MnO}$  particles.<sup>[138]</sup> The long-term measurements showed lower initial oxygen evolution rates compared to the ones measured by the Clark electrode (Table 2.3 Fig. 2.13.) which might be due to the different experimental conditions and setups. The oxygen evolution rate seems also to decrease with time, which however can be explained by the consumption of the oxidant ( $\text{Ce}^{4+}$ ). Indeed addition of a fresh oxidant after 60 h showed that the catalyst remains active, even after long time periods. The same result is seen when a lower amount of catalyst was used (Fig. 2.13).

**Table 2.3: Catalytic test results from gas chromatography (in 0.5 M  $\text{Ce}^{4+}$ ) for repeated addition of oxidant (0.5 M  $\text{Ce}^{4+}$  per run).**

Test	T (°C)	Cat amount (mg)	Rate ( $\text{mmolO}_2 \cdot \text{molMn} \cdot \text{s}^{-1}$ )
Long-term	23	100.8	0.42
Run 1	24.2	100.8	0.40
Run2	25	99.1	0.35
Run3	25	73.7	0.35

Still it should be mentioned that also in this experiment a decrease in the oxygen evolution rate is found, so that some deactivation of the catalysts over time has to be assumed. Partially crystalline  $\text{CaMn}_2\text{O}_x$ -0.8-550, which is the second best catalyst, showed a lower rate of  $0.62 \text{ mmol O}_2 \text{ mol Mn}^{-1} \text{ s}^{-1}$ . The crystalline  $\text{CaMn}_2\text{O}_x$ -0.8-700 is nearly inactive (oxygen evolution rate of  $0.082 \text{ mmol O}_2 \text{ mol Mn}^{-1} \text{ s}^{-1}$ ). Two samples were prepared as references,  $\text{CaMn}_2\text{O}_x$ -0-550 without the use of cyanamide and  $\text{Mn}_2\text{O}_3$ -0.8-550 without calcium, in order to study the role of these two components in the catalytic activity of resulting oxides. The catalytic activity of  $\text{Mn}_2\text{O}_3$ -0.8-550 and  $\text{CaMn}_2\text{O}_x$ -0-550 is 6 and 21 times lower, respectively, compared to  $\text{CaMn}_2\text{O}_x$ -0.8-550. In both cases the resulting oxides had completely different atomic structures. In the absence of  $\text{Ca}^{2+}$ ,  $\text{Mn}_2\text{O}_3$  is formed, while in the absence of cyanamide a mixture of several crystalline phases is obtained (Fig. 2.4 and 6.5.). In recent studies it has been suggested that layered Mn oxide phases have the highest activity in catalytic water oxidation.<sup>[88,150,152]</sup> Moreover, it has been shown that the  $\text{Ca}^{2+}$  ion is an important cofactor in biological oxygen evolution,<sup>[153]</sup> it may control charge balance and oxidation potential of the  $\text{Mn}_4\text{Ca}$  complex.<sup>[154]</sup> The  $\text{Ca}^{2+}$  ion also may act as a Lewis acid to activate water molecules for nucleophilic attack on the electrophilic oxygen atom of Mn-oxyl intermediate.<sup>[155,156]</sup>

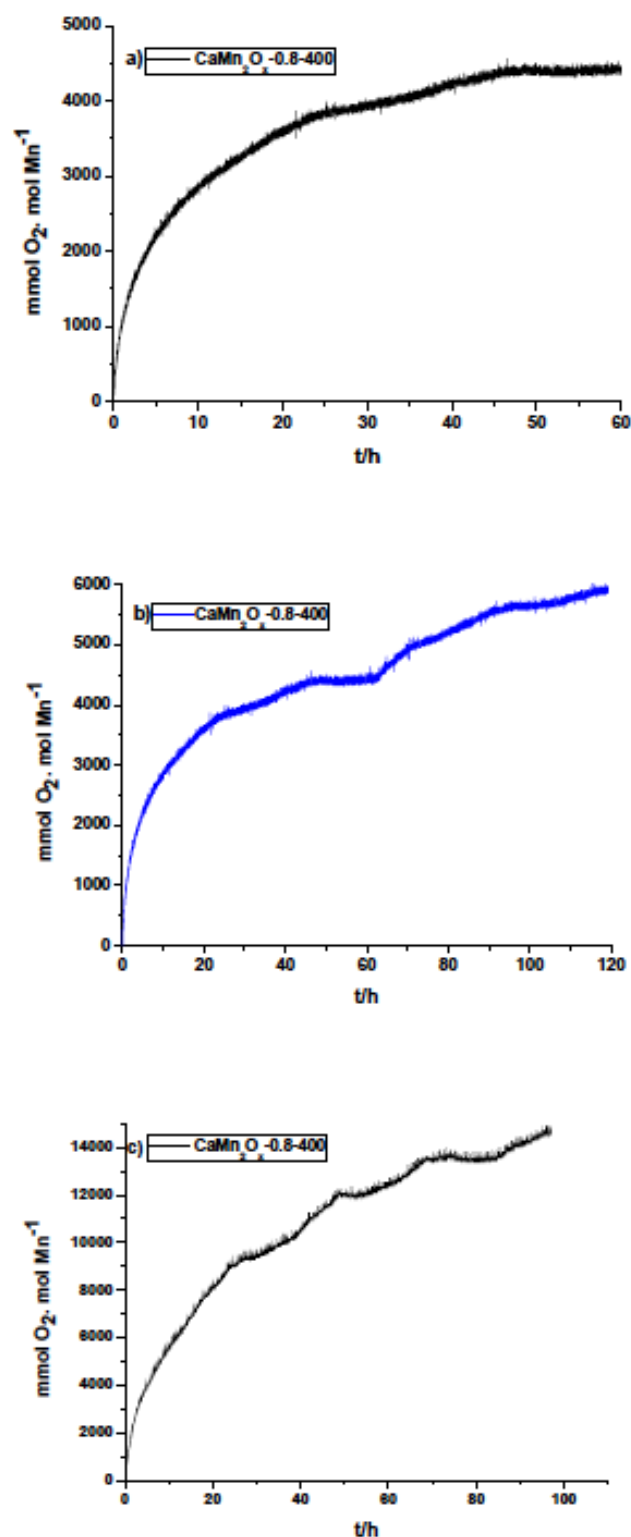


Fig. 2.11: a) Long-term oxygen evolution test (100 mg catalyst in 38 ml of 0.5M  $\text{Ce}^{4+}$  solution) b) Regaining the activity after injection of 12 ml fresh  $\text{Ce}^{4+}$  solution. Slower rate observed due to lower concentration of  $\text{Ce}^{4+}$  in solution (0.12 M) after injection. c) Catalytic activity test with less amount of catalyst (20 mg in 38 ml of 0.5 M  $\text{Ce}^{4+}$  solution.)

## Results and discussion

---

Likewise, in the layered oxides incorporation of the  $\text{Ca}^{2+}$  ion seems to be crucial to increase their activity for water oxidation.<sup>[88,89]</sup> In our case, indeed  $\text{Mn}_2\text{O}_3$ -0.8-550 showed a much lower catalytic activity than  $\text{CaMn}_2\text{O}_x$ -0.8-550.

The manganese oxidation state in the synthesized oxides may be among the crucial determinants of catalytic activity. The average oxidation states were estimated by means of XANES (X-ray absorption near-edge structure) analysis and are presented in Tables 2.1. and 2.2. In the oxide with the highest water-oxidation activity ( $\text{CaMn}_2\text{O}_x$ -0.8-400), manganese shows an average oxidation state of +3.6. It was shown for oxides used as catalysts<sup>[157]</sup> or electrocatalysts<sup>[129,158]</sup> that the performances of materials containing  $\text{Mn}^{3+}$  was superior compared to the ones with pure  $\text{Mn}^{4+}$ , which suggests that the presence of  $\text{Mn}^{3+}$  is essential for having an active catalyst. On the other hand, oxides containing  $\text{Mn}^{3+}$  only (e.g.  $\text{Mn}_2\text{O}_3$ -0.8-550 in our study) are also poor catalysts,<sup>[132,133]</sup> supporting that the presence of both  $\text{Mn}^{3+}$  and  $\text{Mn}^{4+}$  in a suitable ratio enhances the catalytic activity.<sup>[150]</sup>

We note that interpretation of the average oxidation state detected for the various oxides of the present investigation cannot be approached in a fully unambiguous way. An average oxidation state of +3.6 might not result from a mixed-valent  $\text{Mn}^{3+/4+}$  oxide but from a mixture of a  $\text{Mn}^{3+}$  oxide, e.g.  $\text{Mn}_2\text{O}_3$  or  $\text{CaMn}_2\text{O}_4$ , and a  $\text{Mn}^{4+}$  oxide, e.g.  $\beta\text{-Mn}_2\text{O}$  or  $\text{Ca}_2\text{Mn}_3\text{O}_8$ . Indeed, a mixture of microcrystalline phases of various oxides may be present in the inactive, cyanamide-free  $\text{CaMn}_2\text{O}$ -0-550 (see XRD data in Fig. 2.4). Yet in the oxides of high water oxidation activity ( $\text{CaMn}_2\text{O}_x$ -0.8-400/550), the XRD and EXAFS data are best explained in terms of a single phase of a mixed-valent  $\text{Mn}^{3+/4+}$  oxide.

### 2.2.2 Elucidation of structural details

The physical and chemical analysis of the prepared oxides discussed in previous chapter revealed a general overview of the composition and morphology of the compounds. However the structural details for the most active calcium manganese oxide,  $\text{CaMn}_2\text{O}_x$ -0.8-400, have not been discussed yet due to its amorphous nature. To shed light on this part, a more detailed structural analysis was carried out by X-ray absorption spectroscopy. Mean manganese oxidation states of the oxides were determined by XANES and structural details were provided by EXAFS spectra analysis. X-ray absorption spectroscopy (XAS) measurements were carried out by our collaboration partners, the group of Prof. Holger Dau from Free University Berlin.

#### 2.2.2.1 Manganese oxidation states

The X-ray absorption near-edge spectra (XANES) recorded at the Mn K-edge, allowed us to estimate the mean oxidation state of manganese in the samples annealed at different temperatures (Table 2.1 and Fig. 2.14). As is evident from the energy shift of the position of the main absorption edge,<sup>[16]</sup> above 300 °C the mean formal oxidation state of Mn increases from 2 to above 3.5, indicating that most of the initial  $\text{Mn}^{2+}$  is oxidized to  $\text{Mn}^{4+}$  although some low-valence Mn ions are still present. At 1000 °C however,  $\text{Mn}^{4+}$  is reduced to  $\text{Mn}^{3+}$ , the typical Mn oxidation state found in marokite ( $\text{CaMn}_2\text{O}_4$ ).<sup>[159]</sup> Similar Mn-oxidation state changes in mixed CaMn oxides upon annealing were observed before.<sup>[150]</sup> To follow the associated structural changes in the CaMn oxides and to identify the basic structural motifs in the amorphous catalytically active materials, we used extended range dual-edge EXAFS spectroscopy, recording spectra at both Mn and Ca K-edges (Fig. 2.15., Fig. 6.6).

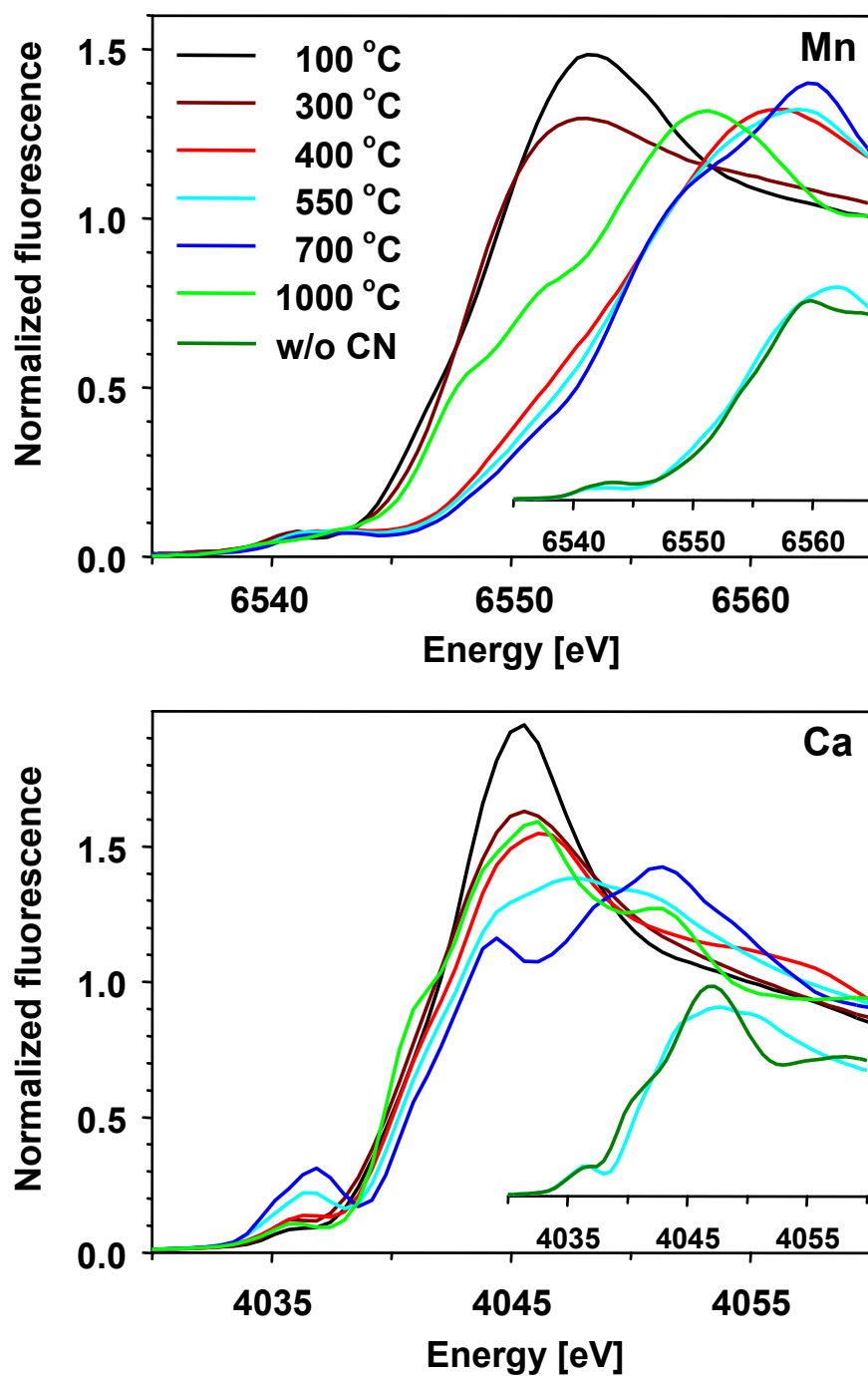


Fig. 2.12: XANES spectra measured at the Mn *K*-edge (top) and the Ca *K*-edge (bottom) from the CaMn material before annealing (labeled '100 °C') and after annealing for 4 h at the indicated temperature. Insets: comparison of the XANES spectra from CaMn oxide with and without cyanamide, annealed at 550 °C.

### 2.2.2.2 Information on atomic structure from EXAFS

X-ray absorption spectra<sup>[16,160]</sup> were collected at the K-edges of both manganese (~6550 eV) and calcium (~4040 eV). The X-ray absorption near-edge structure (XANES; Fig. 2.14) of the Mn K-edge facilitated the above estimates of the mean manganese oxidation states. The Ca-XANES (Fig. 2.14) indicates significant changes in the calcium ligand environment but cannot be easily interpreted in terms of specific structural changes.

Within about 1000 eV above the respective X-ray edge, the extended X-ray absorption fine-structure (EXAFS) was detected. The EXAFS carries information on distances between the X-ray absorbing atom (Mn or Ca) and atoms of the first, second, and higher coordination spheres. The latter atoms are denoted as backscatters as they facilitate backscattering of the photoelectron wave created at the absorber atom. In the Fourier-transformed EXAFS spectra (Fig. 2.15), each peak corresponds to an absorber–backscatter distance, which is 0.3–0.4 Å longer than the indicated reduced distance.<sup>[16,160]</sup>

The first peak of the Fourier-transformed Mn-EXAFS at reduced distances around 1.5 Å is assignable to the oxygen atoms in the first manganese coordination sphere at distances of 1.9 Å or larger. The second peak at a reduced distance of 2.4 Å corresponds to a Mn–Mn distance of 2.87 Å (as revealed by EXAFS simulations) and is assignable to a pair of di- $\mu$ -oxo bridged Mn ions (edge-sharing MnO<sub>6</sub> octahedra). The third peak of Mn-only oxides mostly is assignable to pairs of mono- $\mu$ -oxo bridged Mn ions with typical distances close to 3.4 Å. In the CaMn oxides however, there are contributions to the third EXAFS peak resulting from calcium ions connected by several bridging oxygens to manganese ions. The two long-distance peaks at a reduced distance of about 5.3 and 4.6 Å are assignable to backscattering by manganese ions in the fourth and fifth coordination spheres of the X-ray absorbing manganese (see structural motif indicated in Fig. 2.15); the presence of these two peaks is indicative of long-range order (crystallinity or low level of amorphicity).

Visual inspection of the Mn-EXAFS spectra before (Fig. 6.6) or after Fourier-transformation (Fig. 2.15) reveals that for increasing the temperature from 400 via 550 to 700 °C, the long-range order increases (increased long-distance peaks, Fig. 2.15; increased EXAFS amplitudes at higher k-values, Fig. 6.6). However, the basic shape of the spectra remains the same suggesting that the increase in calcination temperature from 400 to 700 °C causes lowered amorphicity (higher crystallinity) without changing the central structural motifs present in the first and second coordination spheres of the Mn ions. For calcination temperatures below 400 °C, no metal–metal distances are resolved suggesting that the metal ions are not interconnected by bridging oxides but merely coordinated to water molecules and cyanamide-derived ligands.

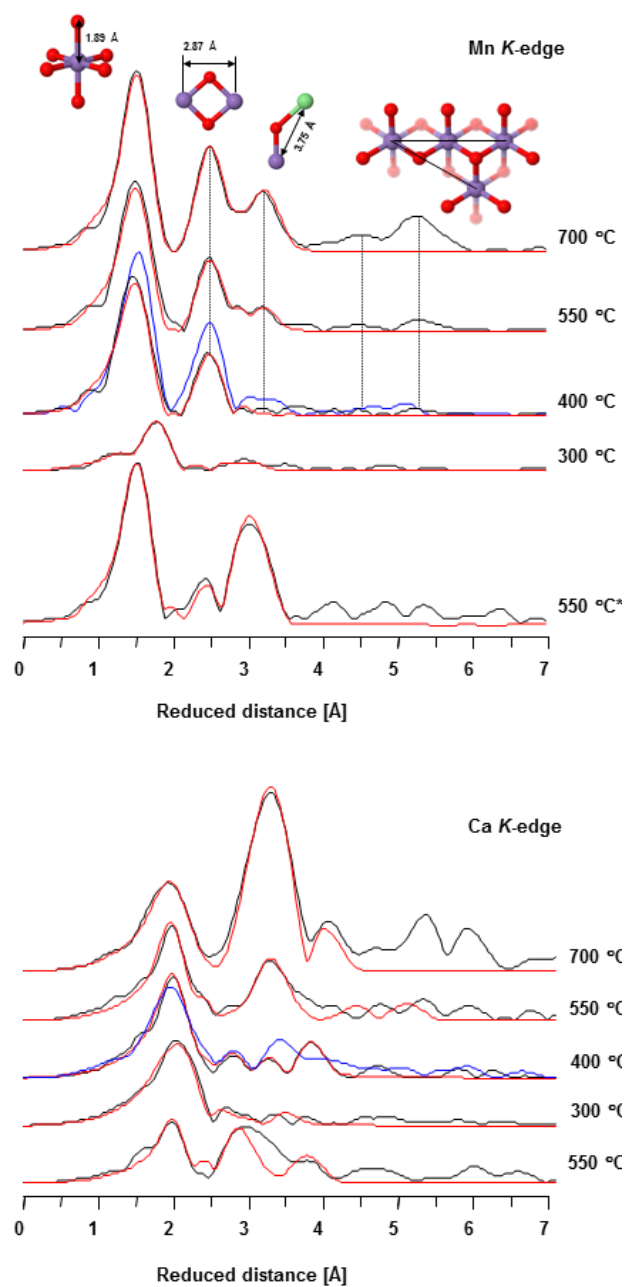


**Fig. 2.13:** Fourier-transformed EXAFS spectra measured at the Mn *K*-edge (top panel) and at the Ca *K*-edge (bottom panel). Black lines, experiment; red lines simulations; blue line, spectra of the catalytically active  $\text{CaMn}^{4+}_{1.6}\text{Mn}^{3+}_{0.4}\text{O}_{4.5}(\text{OH})_{0.5}$  oxide investigated by Kurz et al. <sup>[89,150]</sup>. The asterisk (550 °C\*) indicates the sample prepared without cyanamide. The structural motifs corresponding to each of the main peaks are schematically depicted (Mn in magenta, Ca in green, O in red).

## Results and discussion

---

In clear contrast, the Ca-EXAFS differs pronouncedly between oxides calcined at 400 °C and 700 °C (Fig. 2.15 and 6.6), indicating a pronounced change in the ligand environment of the X-ray absorbing calcium ions. This can be explained as follows. Most likely the calcium ions are located in the space between layers of edge-sharing  $\text{MnO}_6$  octahedra. In the highly ordered and largely dehydrated oxide created by calcination at 700 °C and resembling crystalline  $\text{Ca}_2\text{Mn}_3\text{O}_8$  closely, the majority of calcium ions may directly interconnect layers of edge-sharing  $\text{MnO}_6$  octahedra (see Fig. 2.11.). However in the water-rich oxide obtained by moderate calcination at 400 °C, the calcium ions are coordinated to several water molecules of the interlayer space.

Precise atom–atom distances were obtained by simulating simultaneously the Mn-EXAFS and the Ca-EXAFS using a joint-fit approach described before.<sup>[150]</sup> The simulated spectra are shown in Fig. 2.15. and Fig. 6.6; simulation parameters are given in Table 6.4. For the  $\text{CaMn}_2\text{O}_x$ -0.8-700 oxide, the EXAFS simulation results confirm the prevalence of the  $\text{Ca}_2\text{Mn}_3\text{O}_8$  structure indicated by the XRD, even though the Ca : Mn stoichiometry differ. The distances between  $\mu$ -oxo bridged Mn–Mn and Mn–Ca pairs as determined by the EXAFS simulations agree well with the corresponding distances of the crystallographic model.<sup>[148,149]</sup> Two Mn–Ca distances of 3.3 Å and 3.7 Å are resolved by EXAFS simulations. They are assignable to  $\text{CaMn}_3(\mu\text{-O})_4$  structures resembling distorted cubanes (3.3 Å) and to a motif of Ca ions capping missing layer-building Mn ions (3.7 Å) (Fig 2.16). The characteristic 2.88 Å distance for di- $\mu$ -oxo connected Mn ions of layered oxides<sup>[161]</sup> is well resolved, as well as Ca–Ca distances of  $\text{Ca}_2\text{Mn}_3\text{O}_8$ .

Both XRD and XAS strongly suggest the presence of  $\text{Ca}_2\text{Mn}_3\text{O}_8$  in  $\text{CaMn}_2\text{O}_x$ -0.8-700. There are two possible explanations for the mismatch in the Ca : Mn stoichiometry (1 : 2 in the synthesized oxide versus 2 : 3 in  $\text{Ca}_2\text{Mn}_3\text{O}_8$ ): (a) aside from  $\text{Ca}_2\text{Mn}_3\text{O}_8$  crystallites, a largely amorphous CaMn oxide with a low Ca content is present in  $\text{CaMn}_2\text{O}_x$ -0.8-700. (b) The  $\text{Ca}_2\text{Mn}_3\text{O}_8$  structure may be viewed as layers of edge-sharing  $\text{MnO}_6$  octahedra with Mn-vacancies capped by calcium ions; the removal of capping calcium ions and filling of the corresponding Mn-vacancies could result in a major change in the Ca : Mn stoichiometry, without modification of other unit cell parameters.

The latter explanation (that is, (b)) is in good agreement with the EXAFS results, but also (a) cannot be ruled out definitively. The EDS mapping supports (b) because two distinct phases differing in the Ca : Mn stoichiometry are not detectable. However, the spatial resolution of the presented EDS-mapping data might be insufficient to resolve different phases in neighboring small crystallites. Whether (b) is in conflict with the XRD powder diffraction data remains an open question. Conclusive XRD analysis of amorphous materials or crystallites with an imperfect crystalline order requires extensive simulations, which are beyond the scope of the present study.

## Results and discussion

Distances similar to the ones found in  $\text{CaMn}_2\text{O}_x-0.8-700$  are also found in  $\text{CaMn}_2\text{O}_x-0.8-550$  (Table 6.4). However the coordination numbers for the metal–metal distances are lower suggesting prevalence of a clearly less ordered structure, that is, a clearly higher level of amorphicity in  $\text{CaMn}_2\text{O}_x-0.8-550$ .

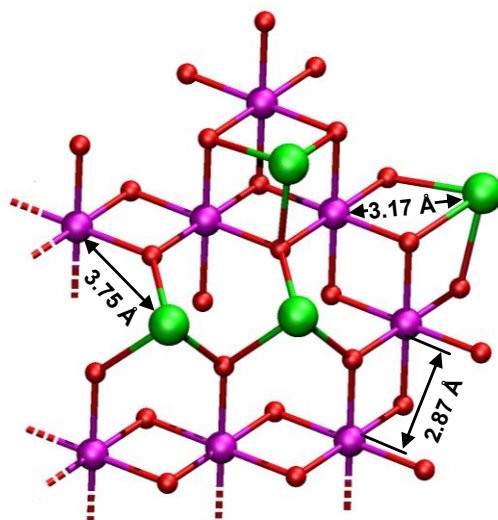


**Fig. 2.14:** Structural model of a fragment from catalytically active  $\text{CaMn}$  oxide.

At 400 °C calcination, the coordination numbers of the 2.9 Å Mn–Mn distance are even lower (lower amplitude of second Fourier peak). All Mn–Mn distances exceeding 3 Å result in small contributions to the EXAFS only indicating an especially high level of amorphicity (see Fig. 2.15). Consequently the Mn-EXAFS simulation results of Table 6.4, which relate to Mn–Mn/Ca distances exceeding 3 Å, are of low significance. It is likely that the Mn–Ca motifs with characteristic Mn–Ca distances of 3.2 Å (cubane) and 3.7 Å (Ca capping Mn- layer-vacancy) are also present in  $\text{CaMn}_2\text{O}_x-0.8-400$ , but clearly less frequently than in the oxides calcined at 550 and 700 °C. It is noteworthy that the amorphicity of  $\text{CaMn}_2\text{O}_x-0.8-400$  is even higher than observed for oxides previously synthesized in the absence of cyanamide (blue lines in Fig. 2.15).<sup>[89]</sup>

In summary, calcination at temperatures higher than 300 °C induces the formation of high-valent  $\text{Mn}^{3+/4+}$  oxides which consist of vacancy-rich layers of edge-sharing  $\text{MnO}_6$  octahedra. These oxides may be considered as being relatives of layered oxides with one layer (birnessite) or two layers (buserite) of water molecules and cations interconnecting  $\text{MnO}_2$  layers.<sup>[162]</sup> For calcinations at 400 °C, the  $\text{CaMn}$  oxide is highly disordered, providing an especially high number of both protonatable (and potentially reactive)  $\mu_2\text{-O(H)}$  bridges and terminal water-coordination sites.<sup>[163]</sup>

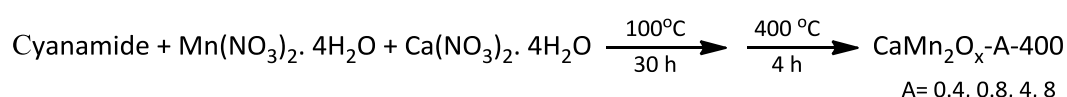
## Results and discussion

This may explain the especially high water-oxidation activity of  $\text{CaMn}_2\text{O}_x\text{-0.8-400}$ , which exceeds the activity of better ordered CaMn oxides previously synthesized in the absence of cyanamide.<sup>[89]</sup> At higher calcination temperatures (550 and 700 °C), the structure becomes increasingly well-ordered and approaches the ‘parent structure’ of crystalline  $\text{Ca}_2\text{Mn}_3\text{O}_8$  closely.

Without the addition of cyanamide but using otherwise the same synthesis protocol, an entirely different structure is formed, which is dominated by mono- $\mu$ -oxo bridging between manganese ions. This structure exhibits higher crystallinity and shows similarities to the  $\beta$ - $\text{MnO}_2$  crystalline phase (1 × 1 tunnel Mn oxides),<sup>[164]</sup> but not to the layered birnessite-like oxides.<sup>[165,166]</sup>

### 2.2.3 Optimum amount of template for $\text{CaMn}_2\text{O}_x\text{-A-400}$

The optimum amount of used cyanamide was based on the catalytic activity of calcium manganese oxides which were prepared at 550 °C.  $\text{CaMn}_2\text{O}_x\text{-0.8-550}$  sample showed the highest activity; therefore 0.8 g cyanamide was used to prepare  $\text{CaMn}_2\text{O}_x\text{-0.8-B}$  series at different calcination temperatures. Finally it has been observed that  $\text{CaMn}_2\text{O}_x\text{-0.8-400}$  with foam-like structure and high surface area is the most active calcium manganese oxide among the ones prepared via cyanamide-based protocol. However, it is worth trying to find out whether utilized amount of cyanamide (0.8 g) is the best amount of the template for preparation of CaMn oxide at 400 °C or the structural characteristics and hence, catalytic activity could be improved by altering the amount of cyanamide. Therefore a series of CaMn oxide was prepared using 0.4, 4 and 8 g cyanamide as porogen.



**Scheme 2.2:** Synthetic route for preparation of  $\text{CaMn}_2\text{O}_x\text{-A-400}$  oxides.

**Table 2.4:**  $\text{CaMn}_2\text{O}_x\text{-A-400}$  materials prepared with different amount of cyanamide.

Name	$S_{\text{BET}}^a$	Rate <sup>b</sup>
$\text{CaMn}_2\text{O}_x\text{-0.4-400}$	18.8	0.50
$\text{CaMn}_2\text{O}_x\text{-0.8-400}$	130.0	3.00
$\text{CaMn}_2\text{O}_x\text{-4-400}$	4.0	0.04
$\text{CaMn}_2\text{O}_x\text{-8-400}$	3.4	0.01

<sup>a</sup>Surface area of oxides ( $\text{m}^2 \cdot \text{g}^{-1}$ ), <sup>b</sup> oxygen evolution rate ( $\text{mmolO}_2 \cdot \text{molMn}^{-1} \cdot \text{s}^{-1}$ ) in presence of  $[\text{Ce}^{4+}] = 0.5 \text{ M}$

## Results and discussion

XRD spectroscopy was carried out to elucidate the structural differences resulted from using varied amount of cyanamide. While  $\text{CaMn}_2\text{O}_x$ -0.4-400 showed presence of mixed-phase oxides with high crystallinity, XRD patterns of  $\text{CaMn}_2\text{O}_x$ -4-400 and  $\text{CaMn}_2\text{O}_x$ -8-400 resembles the patterns of the organic intermediate material which already has been reported for heating melamine (early product of Cyanamide condensation under heat) at temperatures below 600 °C (Fig 6.8).<sup>[167]</sup>

Presence of above mentioned organic phase mixed with inorganic phase (metal oxides) causes the TEM images of  $\text{CaMn}_2\text{O}_x$ -4-400 and  $\text{CaMn}_2\text{O}_x$ -8-400 oxides to show no distinct features. On the other hand crystalline nature of  $\text{CaMn}_2\text{O}_x$ -0.4-400 is obvious in (HR)TEM image of the material (Fig. 2.17). This could be a consequence of using inadequate amount of cyanamide, which undergoes decomposition at the early stage of calcination. Then in the absence of template, further heating causes the agglomeration and crystallization of the formed oxide. Catalytic activity of  $\text{CaMn}_2\text{O}_x$ -A-400 oxides which were tested by means of Clark electrode and in presence of  $\text{Ce}^{4+}$  as an oxidant showed the superior activity of the sample prepared with 0.8 g cyanamide compared to the ones formed in presence of lower (0.4 g) as well as higher (4 and 8 g) amount of template (Fig. 2.18). These results are suggesting that 0.8 g cyanamide which already was found to be the optimum amount of template for  $\text{CaMn}_2\text{O}_x$ -A-550 series is the ideal quantity of template for the formation of porous CaMn oxide catalyst with foam-like structure at 400 °C as well.

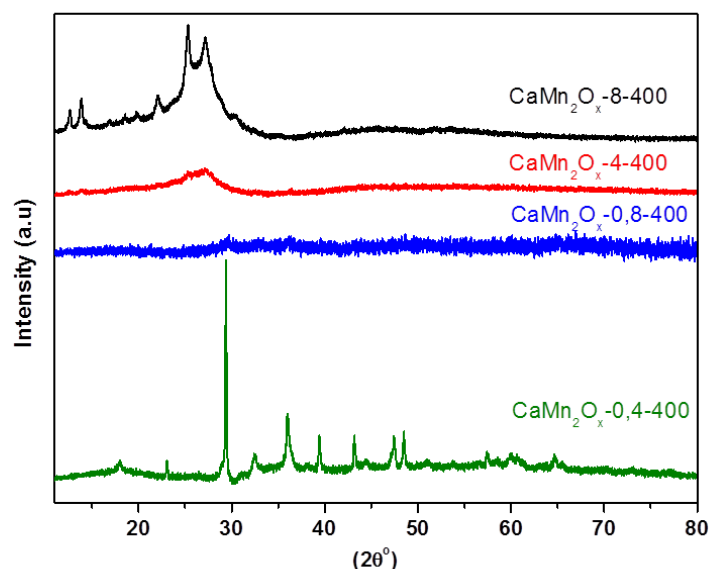


Fig. 2.15: XRD patterns of  $\text{CaMn}_2\text{O}_x$ -A-400 samples.

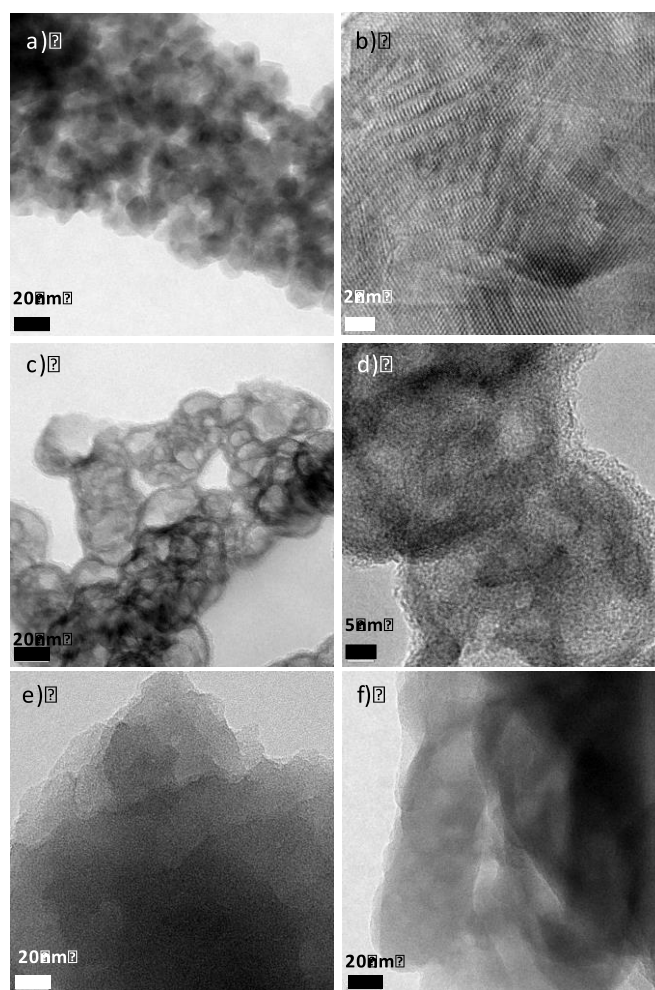


Fig. 2.16: TEM images of a-b)  $\text{CaMn}_2\text{O}_x$ -0.4-400, c-d)  $\text{CaMn}_2\text{O}_x$ -0.8-400, e)  $\text{CaMn}_2\text{O}_x$ -4-400 and f)  $\text{CaMn}_2\text{O}_x$ -8-400

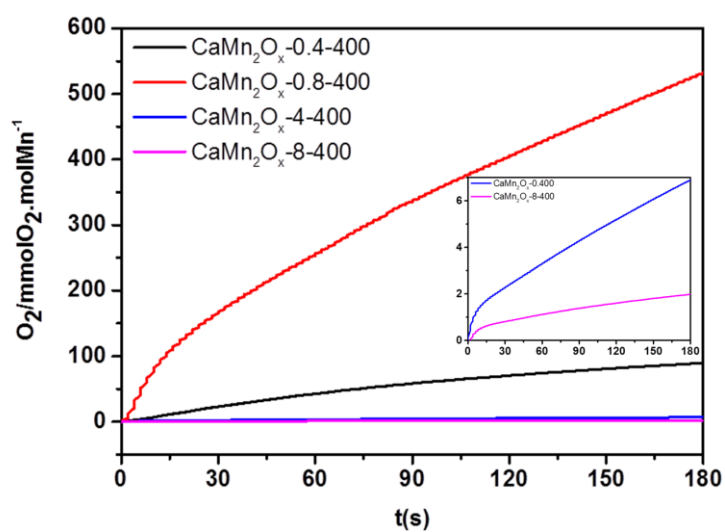
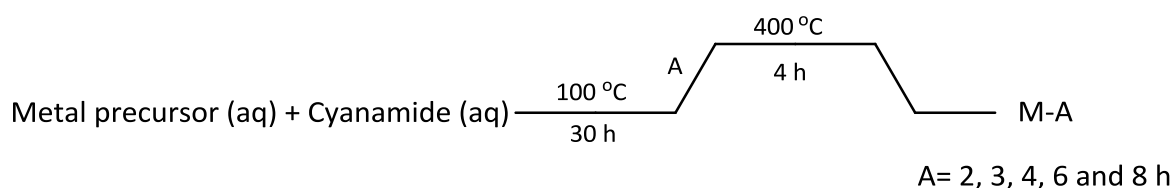


Fig. 2.17: Catalytic test results of  $\text{CaMn}_2\text{O}_x$ -A-400 series, inset: oxygen evolution results of  $\text{CaMn}_2\text{O}_x$ -4-400 and  $\text{CaMn}_2\text{O}_x$ -8-400.

### 2.3 Synthesis and characterization of nickel, cobalt and manganese oxides

Nickel, cobalt and manganese oxides are well-known active catalysts for water oxidation reaction. Due to the success of our cyanamide-mediated approach for preparation of an active CaMn oxide, the same protocol was used for the synthesis of other metal oxides. Nickel, cobalt and manganese oxides were prepared by mixing aqueous solutions of the respective precursors with an aqueous solution of cyanamide. Then the mixture was dried at 100 °C and heated to 400 °C by the ramp-time of 3h and calcined at this temperature for 4 h. This process resulted in nickel as well as cobalt and manganese oxides (M-A, A: ramp time).



**Scheme 2.3: Synthetic route for preparation of metal oxides with different ramp-time.**

**Table 2.5: Mn, Ni and Co oxides prepared with different ramp-time.**

Name	Ramp-time (h)	$S_{\text{BET}}$ ( $\text{m}^2 \cdot \text{g}^{-1}$ )	Phase
Mn-2	2	33.6	$\text{Mn}_2\text{O}_3$
Mn-3	3	37.9	$\text{Mn}_2\text{O}_3$
Mn-4	4	62.4	$\text{Mn}_2\text{O}_3$
Mn-6	6	127.5	$\text{Mn}_2\text{O}_3$ /amorphous
Ni-2	2	13	NiO
Ni-3	3	37.7	NiO
Ni-4	4	38.6	NiO
Ni-6	6	73.0	NiO
Co-2	2	1.3	$\text{Co}_3\text{O}_4$
Co-3	3	6.2	$\text{Co}_3\text{O}_4$
Co-4	4	7.3	$\text{Co}_3\text{O}_4$
Co-6	6	23.0	$\text{Co}_3\text{O}_4$

## Results and discussion

**Table 2.6: Mn, Ni and cobalt oxides prepared with 8h ramp-time.**

Name	$S_{\text{BET}}^{\text{a}}$	Parent phase	$\text{O}_2$ evolution rate <sup>b</sup>
Mn-8	132.5	$\text{Mn}_2\text{O}_3$ /amorphous	1.88
Ni-8	82.0	NiO	0.05
Co-8	28.5	$\text{Co}_2\text{O}_3$	1.24

<sup>a</sup>Surface area of oxides ( $\text{m}^2 \cdot \text{g}^{-1}$ ), <sup>b</sup> oxygen evolution rate ( $\text{mmolO}_2 \cdot \text{molMn}^{-1} \cdot \text{s}^{-1}$ ) in presence of  $[\text{Ce}^{4+}] = 0.5 \text{ M}$

The XRD pattern of nickel oxide powder Ni-3 showed peaks corresponding to a NiO phase. The presence of  $\text{Co}_3\text{O}_4$  and  $\text{Mn}_2\text{O}_3$  phases were also observed from the XRD pattern of cobalt (Co-3) and manganese oxides (Mn-3) respectively (Fig 2.20).  $\text{N}_2$  physisorption was carried out in order to determine the surface area of the oxides, which were 6.2, 37.7 and  $37.9 \text{ m}^2 \cdot \text{g}^{-1}$  for Co-3, Ni-3 and Mn-3 samples respectively.

As observed for CaMn oxides, materials with lower crystallinity are better catalysts for water oxidation reaction. Moreover high surface area, generally can improve the activity of heterogeneous catalysts. It has been seen in previous section that an optimum amount of template and calcination temperature is present which result in the calcium manganese oxide with desired structure and hence activity. Different cyanamide amount and calcination temperatures were tried in order to find the ideal parameter. In case of cobalt, nickel and manganese oxides, we decided to alter one of the synthetic parameters like the ramp-rate which has not been studied in case of calcium manganese oxide, to observe its effect on the crystallinity and surface area of the resulting materials. Therefore a ramp time of 2, 4, 6 and 8h (instead of 3h) were used.

XRD measurements were carried out in order to elucidate the phases and crystallinity of the metal oxides (Fig. 2.20). A significant peak broadening has been seen in the XRD patterns of the resulting oxides with 8h ramp-time, especially in the case of manganese and cobalt oxide. This broadening could be a sign of amorphous nature of the oxides or presence of small nanocrystalline particles.

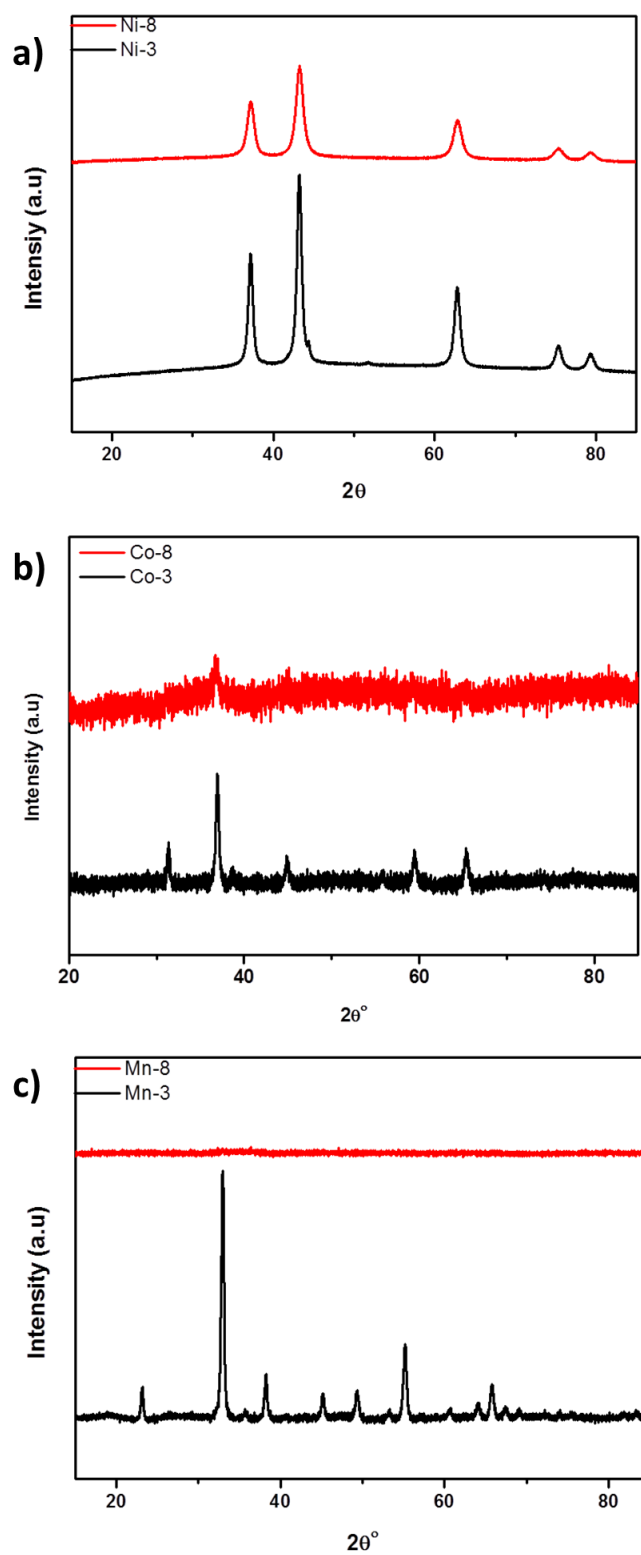


Fig. 2.18: XRD patterns of a) Ni-3 and Ni-8, b) Co-3 and Co-8 and c) Mn-3 and Mn-8.

## Results and discussion

Decreasing the ramp-time to 2 h, forms metal oxides with low surface area (Table 2.5). It has been observed that changing the ramp-time from 3 to 8h did change the surface area of cobalt from 6.2 to 28.5  $\text{m}^2.\text{g}^{-1}$ , nickel oxide from 37.7 to 82  $\text{m}^2.\text{g}^{-1}$  and for manganese oxide from 37 to 133  $\text{m}^2.\text{g}^{-1}$ . It can be assumed that a slow ramping time yields a more intimate mixture of the organic and inorganic compounds and that decomposition of the organic phase is done in a more controlled fashion, yielding well-designed metal oxide residual in form of porous metal oxide.

$\text{N}_2$  physisorption measurement was carried out which shows that, while  $\text{N}_2$  adsorption-desorption isotherm of Ni-8 and Co-8 and Mn-8 shows the mesoporous nature of these oxides, presence of macroporous/nanoparticulate nature of the Co-8 sample is observable.

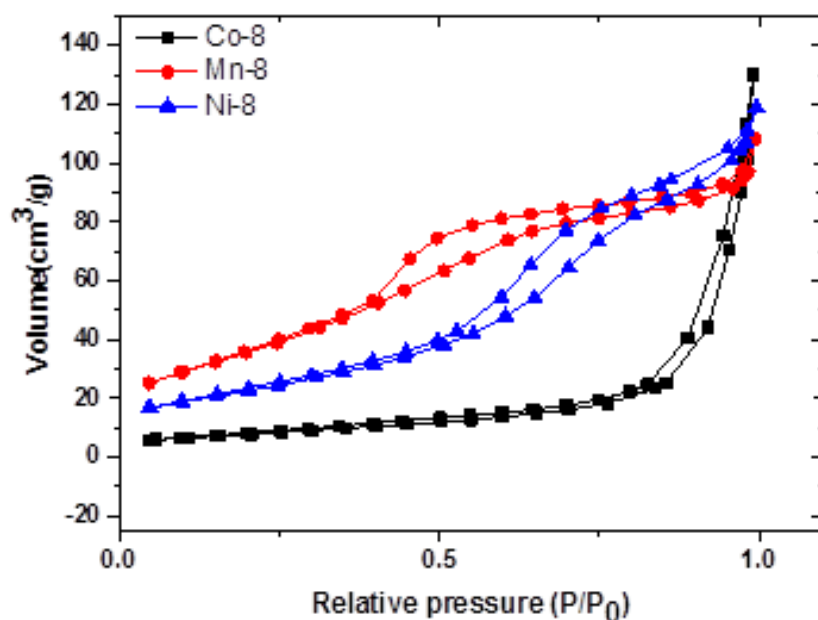


Fig. 2.19:  $\text{N}_2$  adsorption-desorption isotherm of Co-8, Ni-8 and Mn-8 compounds.

Fig. 2.22 presents TEM images of the oxides calcined using 8h ramp-time which shows the improvement in their porosity. (More TEM images are presented in Appendix, Fig. 6.8, 6.9 and 6.10).

These metal oxides, Co-8, Ni-8 and Mn-8, were tested as catalyst for water oxidation reaction in presence of  $\text{Ce}^{4+}$  (Fig. 2.23).

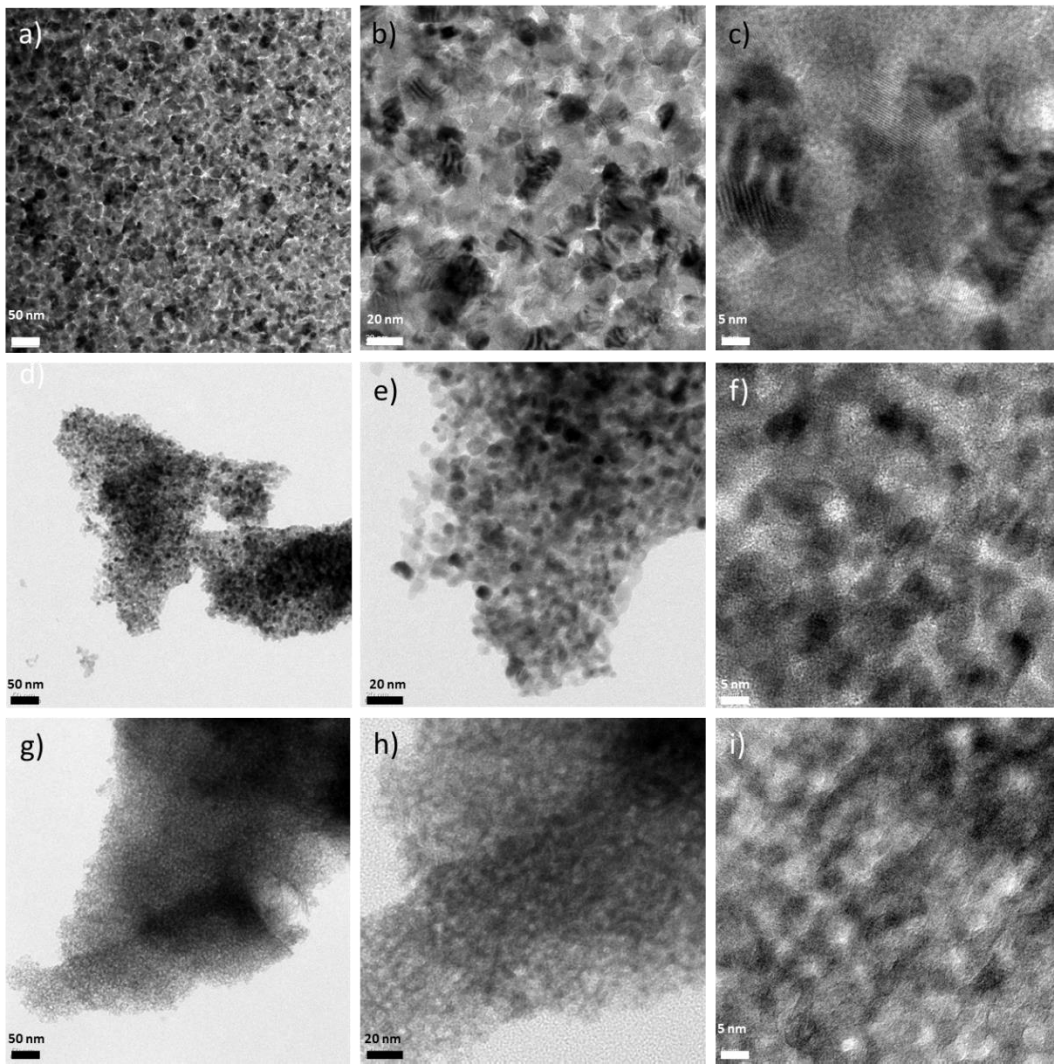
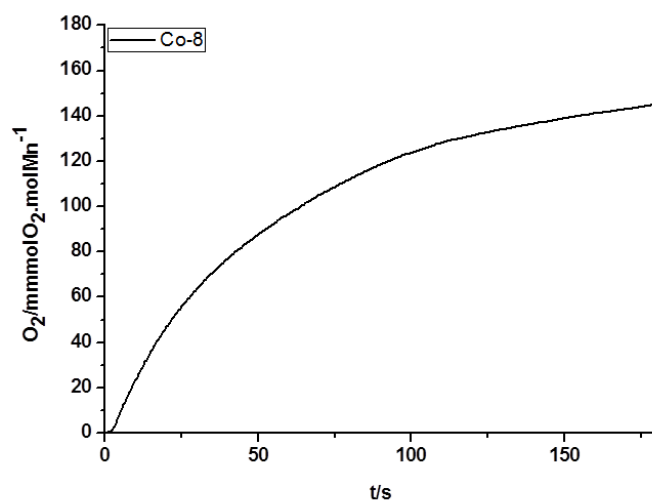
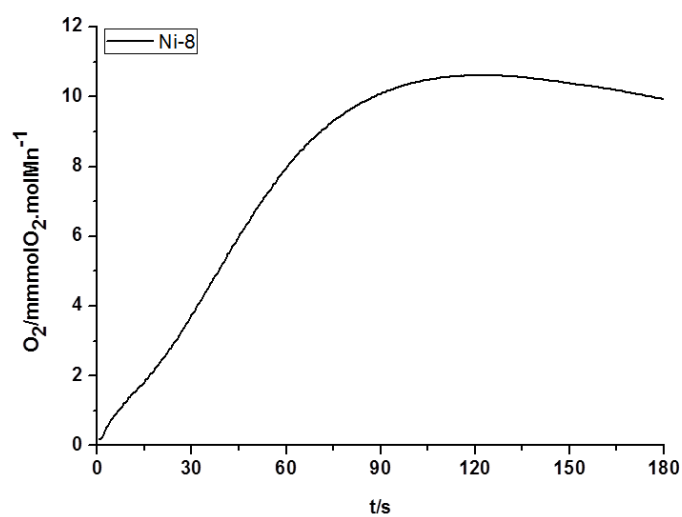


Fig. 2.20: TEM images of a-c) Co-8, d-f) Ni-8 and g-i) Mn-8.

a)



b)



c)

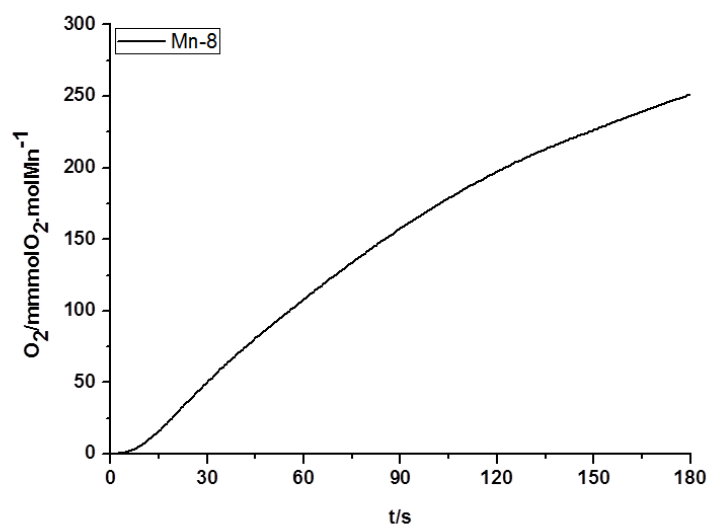


Fig. 2.21: Oxygen evolution test with a) Co-8, b) Ni-8, c) Mn-8 in 0.5 M aqueous  $Ce^{4+}$  solution.

## Results and discussion

---

Our experiments were conducted in 2 ml deoxygenated aqueous solutions containing the metal oxides and cerium ammonium nitrate. A Clark-type electrode was used for the detection of dissolved oxygen produced in these solutions at room temperature. All compounds are active for water-oxidation. The oxygen evolution rate is 0.05 and 1.24  $\text{mmolO}_2 \cdot \text{molMetal}^{-1} \cdot \text{s}^{-1}$  in presence of Ni and Co oxides respectively. The activity of manganese oxide has been increased from 0.1  $\text{mmolO}_2 \cdot \text{molMn}^{-1} \cdot \text{s}^{-1}$  for the oxide prepared by 3h ramp-time to 1.88  $\text{mmolO}_2 \cdot \text{molMn}^{-1} \cdot \text{s}^{-1}$  for the one prepared by 8h ramp-time. This activity is by far higher than other pure manganese oxides which have been reported so far.<sup>[168]</sup>

All the studies on manganese oxides are pointing towards a common set of requirements for the formation of highly active manganese water oxidation catalysts; an extensive network of  $\mu$ -oxido/ $\mu$ -hydroxido bridged Mn centers showing a high level of disorder (i.e., open coordination sites are present) and a mean Mn oxidation state between 3.5 and 3.8. The mixed-valent character of these Mn oxides, as well as the relatively high degree of defect in their structures, might provide the required structural flexibility needed for necessary changes in the oxidation state of the Mn centers, as well as for the O-O bond formation. It is also important to recognize that, even if the oxides are prepared with the use of same precursors and general synthetic route, variations in one of the synthetic parameters leads in differences in the composition, the particle size or the specific surface area which can strongly influence the catalytic activity of the prepared materials.

## 2.4 Synthesis of Cu, Cr, Fe and Sn oxides

In a further study the feasibility of the cyanamide approach was tested to prepare other metal oxides such as Copper, chromium, iron and tin oxides. The same synthetic protocol with cyanamide as porogen has been used to prepare these metal oxides with different calcination ramp-time, 2, 3, 4, 6 and 8h.

**Table 2.7: Cu, Cr, Fe and Sn oxides prepared with different ramp-times.**

Name	Ramp-time (h)	S <sub>BET</sub> (m <sup>2</sup> .g <sup>-1</sup> )	Parent Phase <sup>a</sup>
Cu-2	2	3.7	mixed
Cu-3	3	8.6	mixed
Cu-4	4	9.9	mixed
Cu-6	6	3.8	mixed
Cu-8	8	7.1	mixed
Cr-2	2	12.3	Cr <sub>2</sub> O <sub>3</sub>
Cr-3	3	11.6	Cr <sub>2</sub> O <sub>3</sub>
Cr-4	4	9.4	Cr <sub>2</sub> O <sub>3</sub>
Cr-6	6	9.9	Cr <sub>2</sub> O <sub>3</sub>
Cr-8	8	7.6	Cr <sub>2</sub> O <sub>3</sub>
Fe-2	2	0.5	Fe <sub>2</sub> O <sub>3</sub>
Fe-3	3	1.7	Fe <sub>2</sub> O <sub>3</sub>
Fe-4	4	4.3	Fe <sub>2</sub> O <sub>3</sub>
Fe-6	6	5.3	Fe <sub>2</sub> O <sub>3</sub>
Fe-8	8	7.9	Fe <sub>2</sub> O <sub>3</sub>
Sn-2	2	0.2	SnO <sub>2</sub>
Sn-3	3	0.6	SnO <sub>2</sub>
Sn-4	4	1.2	SnO <sub>2</sub>
Sn-6	6	77.4	SnO <sub>2</sub>
Sn-8	8/0.8	102.5	SnO <sub>2</sub>

<sup>a</sup> Crystal phase elucidated from XRD pattern.

## Results and discussion

---

Table 2.7. presents crystalline phases and surface areas of the oxides prepared with different ramp-times. Cr, Fe and Cu oxides showed crystalline nature regardless of the applied ramp-time but in case of tin oxide, crystallinity decreased by increasing calcination ramp-time.

TEM images show the porous nature of the Sn oxides (Fig 2.24)  $N_2$  physisorption experiment has been carried out to determine the surface area of Cu, Cr, Fe and Sn oxides. The cyanamide-based protocol with the ramp-time of 8h resulted in a highly porous tin oxide. The surface area has been increasing from  $0.2 \text{ m}^2 \cdot \text{g}^{-1}$  (ramp-time: 2h) to  $102 \text{ m}^2 \cdot \text{g}^{-1}$  (ramp-time: 8h) while no significant change is observed in the surface area of the other metal oxides by changing the ramp-time. This phenomenon could be explained by these metals catalytic effect on production and decomposition of organic porogen/template. It may be the case that in presence of Cu, Fe and Cr, polymerization of cyanamide and its decomposition takes place faster, at the beginning of the heating process, and therefore further heating of the material causes pores destruction and particles aggregation.

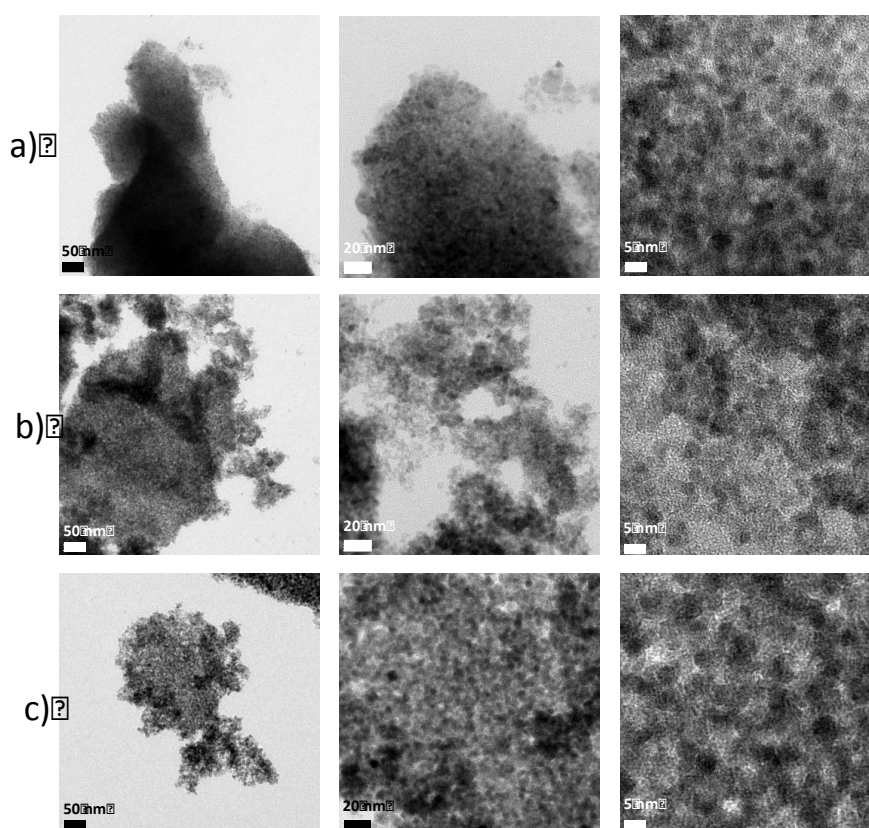


Fig. 2.22: a) TEM images of Sn-4, b) Sn-6 and c) Sn-8.

### 2.5 Summary and conclusion

In this part of the project, a simple, robust and easily reproducible synthetic protocol resulting in highly active mixed CaMn oxide catalyst for water oxidation was presented. CaMn oxides have been prepared by adding cyanamide to the Ca and Mn precursor salts and subsequent thermal treatment. Cyanamide or more probably one of its condensation and decomposition products acts as porogen and foam-like porous CaMn oxides are observed. Some of the resulting CaMn oxides show high activity as catalysts for water oxidation in presence of cerium(IV) ammonium nitrate as a non-oxo transfer oxidant. An amorphous calcium manganese oxide foam with  $130 \text{ m}^2 \cdot \text{g}^{-1}$  surface area and Mn oxidation state of +3.6 was identified to be most active; its activity is superior to previously reported CaMn oxides. At the atomic level, this material shares structural motifs with the biological paragon as revealed by dual-edge XAS at the Mn and Ca *K*-edge. Analysis of crystal and atomic structure of the resulting CaMn oxides shows that besides pore formation and surface area, cyanamide strongly influences also the prevalent Mn oxidation state, the atomic structure, and the level of amorphicity. It is generally assumed that all these factors can influence the catalytic activity of CaMn oxides for water oxidation while the surface area is not the most important factor. At the atomic level, a structure containing poorly ordered layered fragments build from di- $\mu$ -oxo connected Mn ions and coordinatively non-saturated oxygens in bridging positions establish the catalytic properties of the synthetic oxides. Incorporation of  $\text{Ca}^{2+}$  in the structure presumably contributes to the achieved high catalytic rates.

The feasibility of the cyanamide-based synthetic protocol was also examined for the formation of other metal oxides. This approach resulted in porous nickel, cobalt, manganese and tin metal oxides while nonporous materials formed in case of iron, copper and chromium. The effect of different ramp-time in the structure of formed metal oxides was investigated. It has been shown that in case of porous metal oxides increasing the ramp time from 3 to 8h results in oxides with higher surface area. Ni-8, Co-8 and Mn-8 oxides showed catalytic activity for water oxidation reaction in presence of  $\text{Ce}^{4+}$  as oxidant.

### 2.6 Catalysts for dry reforming of methane

#### 2.6.1 Introduction

Reforming of CH<sub>4</sub> with CO<sub>2</sub> has been investigated extensively in the last decades. Numerous materials have been tested as potential catalyst for this reaction. It is well known that noble metals show high catalytic activity in the DRM reaction. Among them Rh<sup>[169][170]</sup> and Ru<sup>[171][172][173]</sup> catalysts have shown the most activity and stability. While Pt<sup>[174]</sup> is not the most active catalyst, its high resistance to carbon formation leads to stable performance. Generally the order of activity for the most active metals which have been investigated so far is Rh, Ru > Ni, Pt, Pd > Co > Fe, Cu<sup>[175]</sup>. Although catalysts based on noble metals are more active and less sensitive to coking, they are costly and have low availability. From an industrial point of view, it is important to develop cheap and economical catalysts with high activity and good resistance to carbon deposition. Ni-based catalysts are one of the most interesting catalysts for DRM reaction due to their high availability and low cost. Therefore studies on promoters, different supports and preparation techniques have been conducted in order to improve the coke resistance of Ni-based catalysts, which, are amongst the most active ones but suffer from severe coke formation.

Considering the endothermic nature of the DRM reaction, a high reaction temperature is required for achieving good conversion. However, particle sintering/agglomeration becomes a critical point at elevated temperatures, which can cause deactivation of the catalyst. Moreover, operating reactions at high temperatures is not economically favored. Therefore it is desirable to operate the DRM process at lower temperatures, which also makes it possible to couple it with other processes like the oxidative coupling of methane (OCM) in which carbon dioxide is produced as a side product. The heat produced by the exothermic OCM can be used for operating the endothermic DRM reaction. The operation temperature of OCM reaction is in the range of 800-850 °C, therefore it is desirable to operate the DRM reaction below this range.

In summary there is a large temperature window in which catalyst for DRM should be investigated. While for coupling DRM with other processes (like OCM) catalysts are required which are already highly active at low temperatures, for high conversions catalysts are needed which are active and most importantly stable at high temperatures.

#### 2.6.2 Effect of supporting material on the catalytic activity of Ni-based catalysts

The supporting materials have a significant effect on the catalytic activity of Ni-based catalysts. It has been shown that a good support provides high Ni dispersion and resistance to sintering during the

high temperature reforming reaction, which results in low coke formation.<sup>[176]</sup> Wang et al.<sup>[177]</sup> showed that the pore structure of the support and metal-support interaction play important roles in catalytic activity and coke resistance. Investigation of the effect of support materials on Ni-based catalysts has indicated that suitable high surface area supports can influence the Ni dispersion, decrease the deactivation of the catalyst due to sintering and migration by increasing the dispersion of the active components.<sup>[178][179]</sup> Therefore mesoporous materials such as SBA-15 and MCM-41 with uniform two-dimensional hexagonal pore arrangements, narrow pore size distribution and large surface areas are interesting options for the choice of support material. The abundant surface silanol groups provide a unique platform for immobilization of transition metal precursors inside the pores of this material.<sup>[180]</sup> Recently Liu et al. presented a series of nickel incorporated MCM-41 and SBA-15 mesoporous molecular sieves.<sup>[180,181]</sup> Catalytic activity and stability of 5%wt, Ni-grafted SBA-15 was related to the strong resistance towards carbon formation and metal sintering caused by the formation of highly dispersed small Ni particles trapped in the silica matrix.<sup>[180]</sup>

It has been furthermore shown that coke formation during DRM reaction over Ni-based catalysts was decreased or even suppressed on supports with a strong Lewis basicity.<sup>[182–184]</sup>  $\text{Al}_2\text{O}_3$  is one of the most explored supports for catalysts in the DRM reaction. This vast application is due to its basic nature promoting a high conversion of  $\text{CO}_2$ .

### 2.6.3 Effect of metal content on the activity of Ni-based catalysts

Variations in the metal content can affect the activity and stability of the catalysts in the DRM reaction. Investigation by Bradford and Vannice showed that the optimum Ni content can vary in different Ni-based catalysts.<sup>[175]</sup> Blanchard et al. found that, in Ni/ $\text{Al}_2\text{O}_3$ -YSZ Catalyst with high Ni content, access of reactant gas to the active sites and support is limited and carbon forms rapidly by methane dissociation leading catalyst deactivation.<sup>[185]</sup> Therefore, high concentration of active metal may result in a higher activity at the beginning of the reaction but a decreased stability over time. It can be concluded that a balance between activity and stability can be achieved by finding the optimum metal loading for each catalyst.

### 2.6.4 Role of promoters in Ni-based catalysts

Modifiers or promoters were used to improve the activity and stability of Ni-based catalysts for the dry reforming reaction. Promoters are generally classified as chemical, which directly takes part in the reaction or textural promoters which are not active in the reaction but change the structure of the catalyst. Most promoters explored for DRM reaction are chemical.

Ru and Rh which are known as active monometallic catalysts in the dry reforming reaction can also be used as promoters on already active materials. It has been shown that doping of Ni/MCM-41 catalyst with Rh can dramatically increase the activity and stability of the catalyst.<sup>[186]</sup> Pietraszek et al. found out that when Rh and Ru are added to Ce-Zr-Ni catalysts, they can inhibit the deposition of non-active carbon and increase the stability of the catalyst.<sup>[187]</sup> Pt and Pd also have been tested as promoters for DRM catalysts.<sup>[188][189]</sup> It has been revealed that addition of Pt to Ni/ $\gamma$ -Al<sub>2</sub>O<sub>3</sub> can effect both catalyst activity and stability. Pt-Ni alloy were formed with low amount of Pt loading, which can be more easily reduced and causing less carbon deposits.<sup>[190]</sup> It was furthermore shown that the synergic effect between deposited Pd and Ni particles in MCM-41 supported Pd-Ni catalysts resulted in a superior activity and stability compared to monometallic catalysts.<sup>[189]</sup>

Various textural promoters including alkali, alkaline and rare-earth metals promoted Ni catalysts were also reported extensively. These promoters generally facilitate the formation of dispersed active phases and may also prevent their changes during the reaction period. Promoters including Li, K, Mg, Ca, Mn, Yt, Ce and Zr have been reported recently. In a study on modified Ni/Al<sub>2</sub>O<sub>3</sub> with different dopant, it has been shown that each dopant could affect the catalyst performance in a different way.<sup>[191]</sup> Utilizing K and Sr as promoters in Ni/Al<sub>2</sub>O<sub>3</sub><sup>[192]</sup>, Co/Al<sub>2</sub>O<sub>3</sub><sup>[193]</sup> and Ni/MgO<sup>[194]</sup>, resulted in lower carbon deposition and higher stability. MgO also was reported to be used as promoter for Ni/Al<sub>2</sub>O<sub>3</sub><sup>[195]</sup> and Co/SiO<sub>2</sub><sup>[196]</sup> catalysts. In high metal loaded Co/SiO<sub>2</sub> catalyst, Mg<sub>2</sub>SiO<sub>4</sub> phase formed small metallic Co particles, which prevent sintering during the reaction period and increased catalyst stability. Stabilization occurred with the addition of K, Ca, Mg, La and Ce dopants to the catalyst with ZrO<sub>2</sub> support<sup>[197]</sup>. The doping effect of phases such as ZrO<sub>2</sub><sup>[198]</sup>, CeO<sub>2</sub><sup>[199]</sup> and Ce<sub>x</sub>Zr<sub>1-x</sub>O<sub>2</sub><sup>[181]</sup> on Ni catalysts has also been investigated. It was found that the higher amount of oxygen vacancies close to active metal sites promotes carbon removal from the metallic surface.<sup>[200]</sup> Mn also has been used as promoter to increase the stability of Ni-based catalyst.<sup>[201]</sup> Mn has multiple valance state with a superior performance of oxidation and reduction, which could assist the stabilization of the metallic Ni, forming more selective and stable catalysts.<sup>[202,203]</sup>

### 2.6.5 Methods of catalyst preparation

Different synthetic methods can be used to develop systems for catalytic reforming of methane. However, the synthesis process can strongly influence the physical characteristics of the finally obtained catalytic system. Thus, one must choose the synthesis method based on the required physical characteristics of the material according to the desired reaction. It has been shown by Blanchard et al. that the catalyst preparation protocol can determine the surface density of Ni particles, the catalyst activity and its life span.<sup>[185]</sup> They found that, for the catalyst prepared via

impregnation of ceramic support by nitrate solutions, the initial concentration of parent solution as well as duration of the impregnation and the surface area of the ceramic greatly influence the size of deposited Ni particles, which in turn, affects the level of carbon deposition on DRM reaction. Extensive range of conventional and novel preparation techniques have been used in heterogeneous catalyst preparation. Among them templating, impregnation and atomic layer deposition were used in our work to prepare suitable types of catalysts to operate DRM reaction in a full temperature window from low to high temperatures (500-900 °C).

## 2.7 Results and discussion

### 2.7.1 Nickel manganese oxides

From an industrial standpoint, it is more practical to use non-noble metal catalyst in order to avoid the high cost and limited availability of noble metals. In this respect nickel has received significant attention because of its high activity and availability.<sup>[204]</sup> However Ni-based catalysts suffer from deactivation due to sintering and coke formation<sup>[175,204]</sup>. In recent decades many attempts have been made to decrease carbon formation during the dry reforming of methane reaction. It has been reported that the addition of Cr<sup>[205,206]</sup> and Mn<sup>[201,207]</sup> can significantly suppress carbide formation, which is believed to be an intermediate in the carbon formation process. Takanahe et al.<sup>[208]</sup> reported that a homogenous alloy of Co and Ni showed good activity and also stability. As a result it has been suggested that bimetallic catalysts may exhibit superior performance compare to monometallic ones in the dry reforming of methane. Recently Xie et al.<sup>[207]</sup> reported the preparation of silica supported nickel manganese oxide solid solution as catalyst for the DRM reaction. Ni<sub>0.2</sub>Mn<sub>0.8</sub>O-SiO<sub>2</sub> showed improvement in stability as well as activity. It is assumed that Ni<sup>0</sup> particles, formed during the first reduction step, are the active sites for methane conversion. The formation of small and highly dispersed nanocrystallites of nickel manganese oxide is beneficial for the formation of small Ni<sup>0</sup> particles on the surface of the catalyst during the reaction period, which results in higher activity and stability. It was furthermore seen that the strong metal-support interaction (SMSI) between Ni<sup>0</sup> and MnO is important for the observed high catalytic activity and stability of the nickel manganese catalyst. It has been found that this interaction between Group VIII NPs and reducible transition metal oxides (MOs) drastically suppress the chemisorption of H<sub>2</sub> and CO on the metal surface.<sup>[209,210]</sup> This suppression occurs because of the coverage of the active site surface by the overlayer of partial reduced metal oxides. By reduction in the adsorption of H<sub>2</sub> and CO, the equilibrium of the DRM reaction is shifted to the production of synthesis gas. Moreover both Ni and Mn are abundant and cheap metals, more suitable than the active noble metals for industrial application. It has been proven that the surface manganese shows a stronger CO<sub>2</sub> adsorption which accelerates the reverse

## Results and discussion

---

Boudouard reaction and removes the surface carbon formed via methane dissociation and therefore prevents catalyst deactivation. Based on the factors mentioned above, nickel and manganese have been chosen as candidates to be used in catalyst preparation for the DRM reaction.

As it has been shown in the previous chapter, the cyanamide protocol is a facile method to prepare high surface area binary and ternary metal oxides. Therefore in a first attempt, nickel manganese oxides were prepared using the same protocol as shown for calcium manganese oxides as water oxidation catalysts. Aqueous solutions of nickel and manganese precursors were mixed with an aqueous solution of cyanamide. This mixture was dried and then calcined at 400 °C. The resulted porous nickel manganese oxide was tested as catalyst for DRM reaction.

### 2.7.2 Synthesis and characterization of porous nickel manganese oxide

From the results presented in chapter 2.2 and 2.2.3, among the series of ternary CaMn oxides prepared via utilization of cyanamide with varied amounts (0-8 g) and calcination at different temperatures (300-1000 °C), the oxide prepared with 0.8 g cyanamide and calcined at 400 °C showed foam-like porous structure with high catalytic activity. Here the same synthetic protocol was applied for the preparation of nickel manganese oxide, in order to achieve porous foam-like metal oxide material to be utilized as catalyst in the DRM reaction. The first nickel manganese oxide sample was prepared with the ratio of 1:2 between nickel and manganese.

The XRD pattern of  $\text{NiMn}_2\text{O}_x$  showed the formation of a compound of a mixed-phase nickel manganese oxide (Fig. 6.11). A foam-like structure can be observed in the TEM images (Fig. 2.25). The surface area of  $\text{NiMn}_2\text{O}_x$  was determined by  $\text{N}_2$  physisorption measurement to be  $120 \text{ m}^2 \cdot \text{g}^{-1}$ .

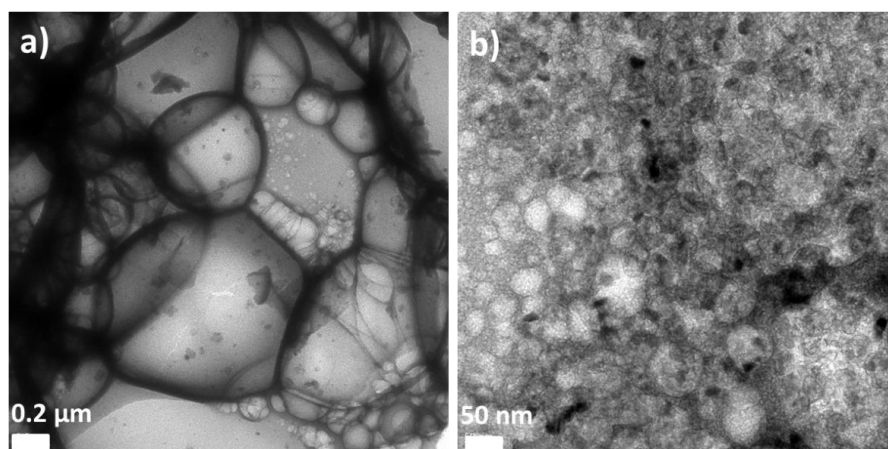


Fig. 2.23: TEM images of  $\text{NiMn}_2\text{O}_x$  prepared with 0.8 g cyanamide at 400 °C.

Table 2.8: Characterization of nickel manganese oxides.

Name	$S_{\text{BET}}^{\text{a}}$	Phase <sup>b</sup>
NiMn <sub>2</sub> O <sub>x</sub>	120.5	mixed-phase (NiO-Mn <sub>2</sub> O <sub>3</sub> )
NiMn <sub>6</sub> O <sub>x</sub>	110.3	mixed-phase (NiO-Mn <sub>2</sub> O <sub>3</sub> )
NiMn <sub>8</sub> O <sub>x</sub>	123.0	mixed-phase (NiO-Mn <sub>2</sub> O <sub>3</sub> )

<sup>a</sup>Surface area of the oxides ( $\text{m}^2 \cdot \text{g}^{-1}$ ), <sup>b</sup>Crystalline phase as deduced from XRD patterns.

### 2.7.3 Catalytic test on NiMn<sub>2</sub>O<sub>x</sub>

All catalytic tests were carried out by Patrick Littlewood in the group of Prof. R. Schomaecker at TU Berlin. Here just optimized protocols for the catalytic tests are shown. Further information on the influence of reaction parameters on the DRM reaction will be presented in the PhD thesis of P. Littlewood.

NiMn<sub>2</sub>O<sub>x</sub> was tested as catalyst in the DRM reaction in a fixed-bed reactor made of quartz with an inner diameter of 5mm and a length of 40mm. The experiment starts from 500 °C and ramps to 600 °C, with an increasing rate of 1 °C.min<sup>-1</sup>. The reaction was performed for 5 h at each temperature. At 500 °C, NiMn<sub>2</sub>O<sub>x</sub> was stable and showed 31% methane conversion during 5 h time on stream. Because of the thermodynamic barrier of the DRM reaction, the methane conversion is limited to 31% at 500 °C. To increase the conversion, higher temperatures must be applied.

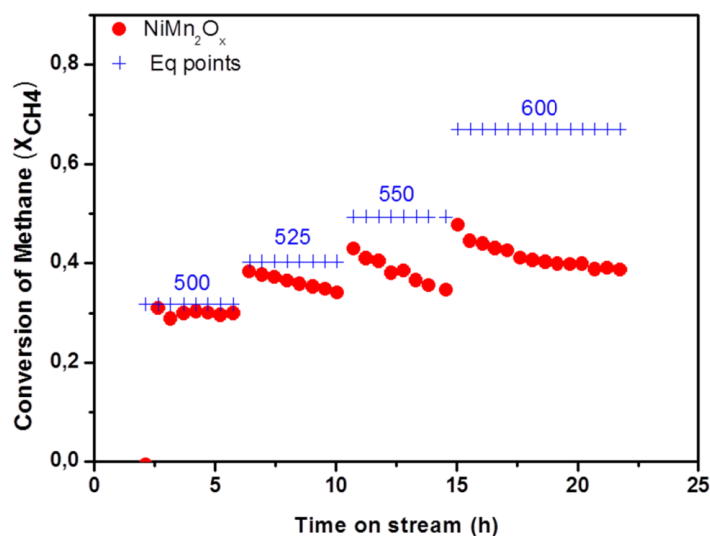


Fig. 2.24: CH<sub>4</sub> conversion as a function of time on stream over catalysts NiMn<sub>2</sub>O<sub>x</sub> GHSV= 36 L h<sup>-1</sup>gcat<sup>-1</sup>.

The catalytic results at low temperatures (500 °C) show that the activity of porous NiMn<sub>2</sub>O<sub>x</sub> is better compared to nickel manganese solid solution Ni<sub>0.2</sub>Mn<sub>0.8</sub>O<sub>cp</sub> prepared by Xiao et al. via coprecipitation method<sup>[207]</sup> and much more active than other reported Ni-based catalysts, including Pt doped NiMgO solid solution.<sup>[211]</sup> While NiMn<sub>2</sub>O<sub>x</sub> shows stable full methane conversion (31%) during 5 h time on stream, the Ni<sub>0.2</sub>Mn<sub>0.8</sub>O<sub>cp</sub> catalyst just reaches 20% conversion. This higher activity could be the result of the high surface area of porous nickel manganese oxide. The NiMn<sub>2</sub>O<sub>x</sub> showed high catalytic activity at each ramp but slowly started to deactivate at higher temperatures (525-600 °C ) over time on stream (Fig.2.26). Thus it can be concluded that like Ni<sub>0.2</sub>Mn<sub>0.8</sub>O<sub>cp</sub>, NiMn<sub>2</sub>O<sub>x</sub> benefits from the strong metal-support interaction (SMSI) between Ni and MnO which suppresses the adsorption of CO and H<sub>2</sub> and increase the activity of the catalyst. However the catalyst still suffers from deactivation over time at elevated temperatures (See section 2.7.4.2).

### 2.7.4 Synthesis and characterization of NiMn<sub>6</sub>O<sub>x</sub> and NiMn<sub>8</sub>O<sub>x</sub>

Ni<sup>0</sup> or Ni<sup>0</sup> clusters are assumed to be the active sites for a nickel-based catalyst. Therefore the concentration of surface Ni atoms which determines the size of reduced Ni<sup>0</sup> particles is a crucial factor: in general it can be expected that a high concentration results in high activity but also stronger tendency to Ni clusters agglomeration which then leads to deactivation with time especially at elevated temperatures. This is one probable reason for the observation of deactivation in NiMn<sub>2</sub>O<sub>x</sub>-foams. Lower concentrations can suppress Ni<sup>0</sup> clusters agglomeration/sintering and the interactions between reduced Ni and the support MnO help to stabilize Ni<sup>0</sup> on the surface. Therefore to prepare a catalyst with highly dispersed active sites, two more nickel manganese oxides with lower Ni content, NiMn<sub>6</sub>O<sub>x</sub> and NiMn<sub>8</sub>O<sub>x</sub>, were prepared using the same synthetic protocol. NiMn<sub>6</sub>O<sub>x</sub> and NiMn<sub>8</sub>O<sub>x</sub> also showed mixed-phase (Fig. 2.27) porous foam-like structure with high surface area of 110.3 and 123 m<sup>2</sup>.g<sup>-1</sup> respectively (Fig. 2.28, table 2.8)

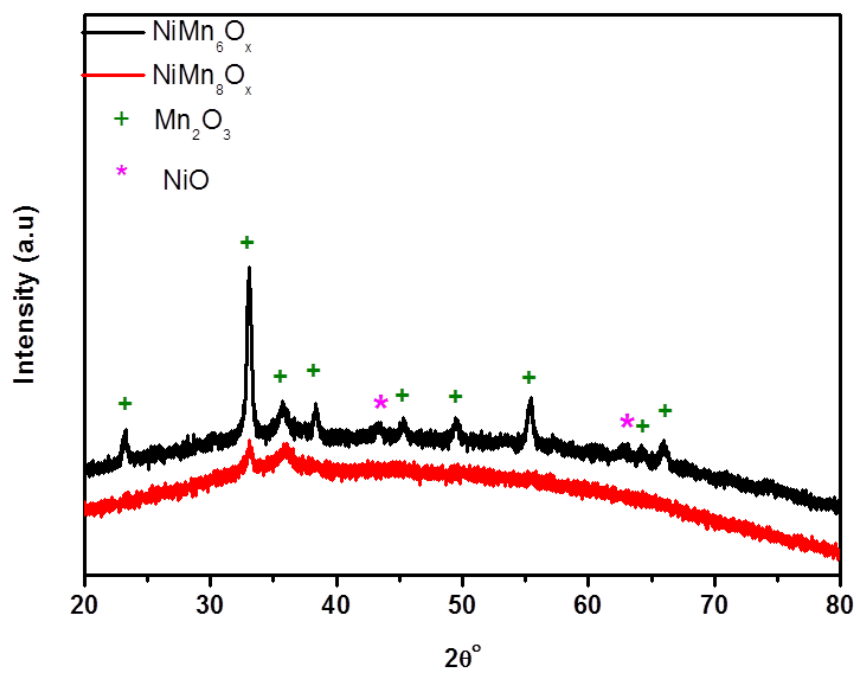


Fig. 2.25: XRD patterns of  $\text{NiMn}_6\text{O}_x$  and  $\text{NiMn}_8\text{O}_x$ .

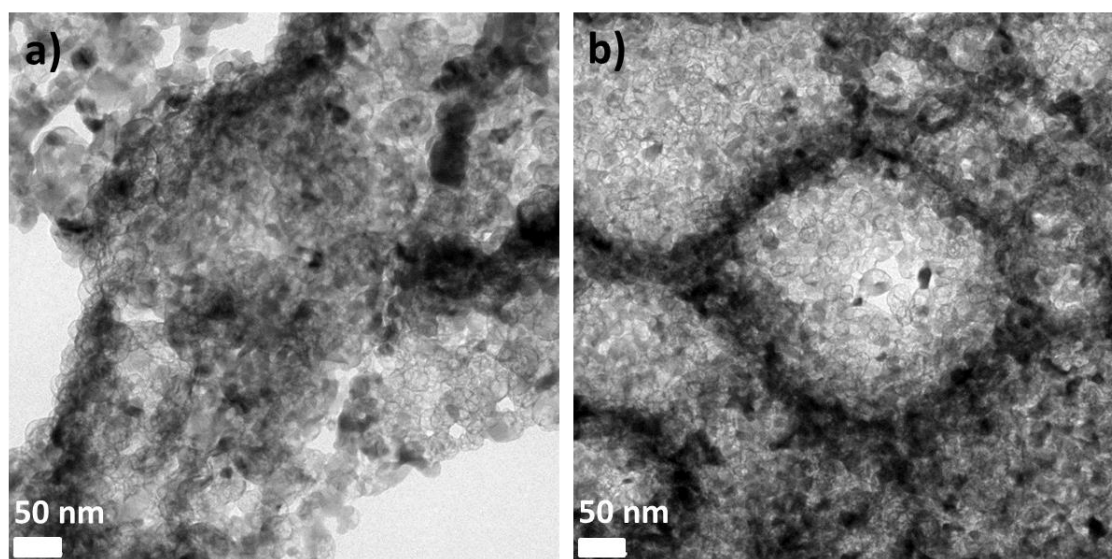


Fig. 2.26: TEM images of a)  $\text{NiMn}_6\text{O}_x$  and b)  $\text{NiMn}_8\text{O}_x$ .

### 2.7.4.1 Catalytic activity of $\text{NiMn}_6\text{O}_x$ and $\text{NiMn}_8\text{O}_x$

Fig. 2.29 presents the screening results of the DRM reaction over the catalysts  $\text{NiMn}_6\text{O}_x$  and  $\text{NiMn}_8\text{O}_x$ . For both catalysts, the methane conversion increases with increasing reaction temperature due to the endothermic nature of the DRM reaction. As can be expected, at 500 °C methane conversion was lower for both catalysts than for  $\text{NiMn}_2\text{O}_x$  resulting from the lower amount of active Ni species in these catalysts. The Ni content as well as conversion trend is  $\text{NiMn}_2\text{O}_x > \text{NiMn}_6\text{O}_x > \text{NiMn}_8\text{O}_x$ . However, the situation changes already at 525 °C. The conversion is initially higher for the catalysts with higher Ni amount ( $\text{NiMn}_2\text{O}_x$  and  $\text{NiMn}_6\text{O}_x$ ) but decrease strongly during the reaction. After 5 h time on stream, the more stable catalysts,  $\text{NiMn}_8\text{O}_x$ , still shows constant conversion and finally reaches the same activity level as the Ni-rich catalyst. At higher temperatures this catalyst then even outperforms the Ni-rich catalysts ( $\text{NiMn}_2\text{O}_x$  and  $\text{NiMn}_6\text{O}_x$ ) in terms of activity.

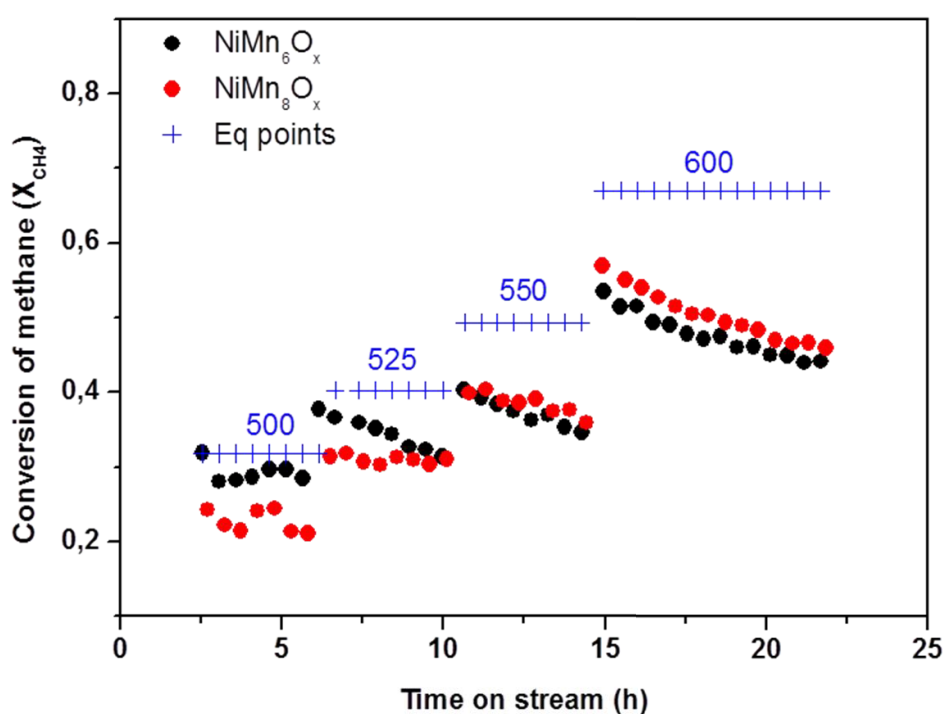


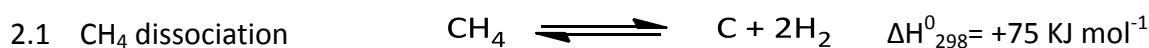
Fig. 2.27  $\text{CH}_4$  conversion as a function of time on stream over catalysts  $\text{NiMn}_6\text{O}_x$ -0.8-400 and  $\text{NiMn}_8\text{O}_x$ -0.8-400,  $\text{GHSV}=36 \text{ L}\cdot\text{h}^{-1}\cdot\text{g}^{-1}$ .

As mentioned before, an optimum loading of Ni in Ni-based catalysts is necessary to achieve satisfactory catalytic performance. Here it is clearly shown that an initial high catalytic activity is not a crucial factor for evaluating the feasibility of a catalyst, but the catalyst stability is of even higher

importance. Thus a catalyst with lower initial activity might in course of reaction, outperforms a highly active catalyst, as it is shown here for the series of nickel manganese oxide foams. However, it is noted that all nickel manganese oxide foam catalysts, made by the cyanamide route, deactivate to an insufficient amount at even higher temperature (>525 °C). This also shows that the desired temperature window, in which the reaction has to be carried out, must be considered when judging about catalyst performance.

### 2.7.4.2 The source of catalyst deactivation

Carbon deposition in dry reforming reaction takes place via two different pathways. Thus could be a result of methane dissociation and Boudouard reaction.<sup>[212]</sup>



Several investigators including Reitmeier<sup>[213]</sup>, Sacco<sup>[214]</sup> and Gadalla et al.<sup>[30]</sup> have reported calculations, which revealed the potential carbon formation during DRM reaction in presence of gas mixture containing CH<sub>4</sub>, CO<sub>2</sub>, H<sub>2</sub> and H<sub>2</sub>O. It has been suggested that carbon deposition is thermodynamically favored at temperatures lower than 1000 °C, CO<sub>2</sub>/CH<sub>4</sub> in equal ratio and at reactor pressures around 1 atm or temperature around 1100 °C, at pressures around 10 atm and CO<sub>2</sub>/CH<sub>4</sub> ratio far from equal.<sup>[215]</sup> However it is more desirable to operate at lower temperature with CO<sub>2</sub>/CH<sub>4</sub> ratio near unity (See below).

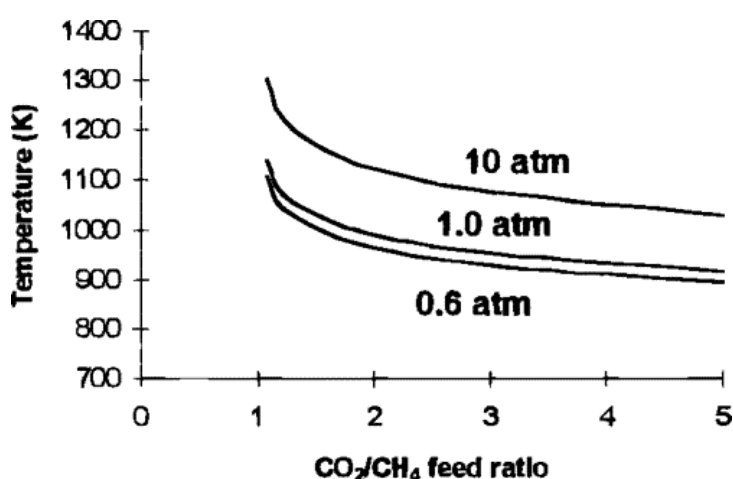


Fig. 2.28: Effects of feed ratio and pressure of CO<sub>2</sub>/CH<sub>4</sub> on limiting temperatures below which carbon deposition is observed.<sup>12</sup>

## Results and discussion

---

The CO disproportionation is exothermic; therefore the Boudouard reaction occurs at lower temperatures. On the other hand methane dissociation is endothermic and the equilibrium constant increases with increasing temperature. Reitmeier et al.<sup>[213]</sup> showed that based on their calculation, at thermodynamic equilibrium, carbon deposition decreases at higher performance temperatures. Their finding suggests that the main origin of carbon formation is CO disproportionation. In order to clarify this Swaan et al.<sup>[216]</sup> and Tsipouriari et al.<sup>[217]</sup>, by means of isotope labeling and temperature programmed oxidation (TPO), showed that carbon deposition originates from both CH<sub>4</sub> and CO<sub>2</sub>, but more from the latter one, suggesting that methane dissociation is not the major cause of coke formation. The deposited carbon can have different reactivity, structure and morphology, which depend on the catalyst nature and reaction conditions.

Catalyst deactivation can occur not only via carbon deposition but also by changes in the catalyst morphology, such as sintering and agglomeration of active sites or, especially for high surface area materials, collapsing of the porous support structure. Sintering is a complicated process, which depends on different factors such as reaction situation, the type of active site, support and their interaction. Generally sintering happens in supported metal catalyst when the temperature is roughly half of the active metal melting point<sup>[218]</sup>; therefore it is a common phenomenon during high temperature DRM reaction.

However in this case the observed stability trend for nickel manganese oxides can be also explained by morphological and structural changes in the catalysts at increasing temperatures. As we previously observed, the porous foam-like structure of the CaMn oxides is collapsing by heating the materials higher than 550 °C which might be also the case for NiMn oxides. In order to identify possible changes in the structure of the catalyst, XRD measurements were carried out on the materials NiMn<sub>2</sub>O<sub>x</sub> and NiMn<sub>8</sub>O<sub>x</sub> after the DRM reaction, shown in Fig. 2.31. XRD patterns of the corresponding materials indicate the formation of Ni<sub>x</sub>Mn<sub>1-x</sub>O<sup>[219]</sup> solid solution. Moreover extra peaks corresponding to Ni<sup>0</sup> and carbon fibers indicate the formation of large ensembles of metallic nickel and carbon deposition during catalytic performance. These peaks are more intense in case of NiMn<sub>2</sub>O<sub>x</sub> than NiMn<sub>8</sub>O<sub>x</sub>, reflecting the higher amount of Ni used in the former.

As described before the porous nickel manganese oxide materials are better described as pre-catalysts which are converted to the actual catalyst during pretreatment (reduction while heating at 500 °C). From XRD it can be seen that lower amounts of Ni in the formed porous nickel manganese catalyst precursor, yield smaller nanoparticles during reduction/reaction which is most probably the main reason for the higher stability and lower carbon formation of the nickel manganese oxide catalyst with lower amount of active species at low temperatures. However, as shown before all catalysts deactivate at higher temperatures. TEM images of the materials after reaction at 600 °C

## Results and discussion

show larger particles and carbon deposition in agreement with the XRD pattern (Fig. 2.32). As assumed the foam like porous structure has entirely collapsed at temperatures around 550 °C, yielding larger NiMn oxide particles with presumably lower surface area.

These images revealed the formed carbon consists of nanofibers with a whiskerlike morphology. Some of the fibers contain metal nanoparticles. A typical model for the formation of carbon nanofibers involves the decomposition of carbon sources such as CH<sub>4</sub> or CO on the catalyst surface, then diffusion of the formed carbon into the metal particles and precipitation as graphitic layers. When the rate of carbon diffusion into the metal catalyst particles is slower than the carbon formation on the surface, carbon accumulates on the surface as carbon fibers and eventually encapsulates the metal particle.<sup>[220,221]</sup> Encapsulation of the metal particles has a greater effect on the catalyst activity than the fiber formation itself. After fibers formation some active sites of the particle may be still available to the reactant gasses but encapsulation will make them entirely nonaccessible.

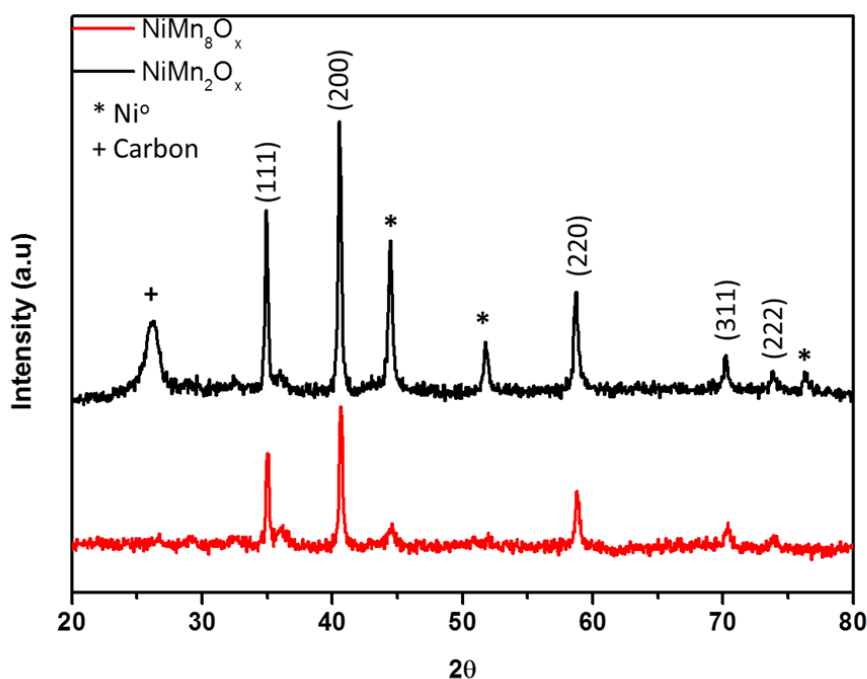


Fig. 2.29: XRD pattern of NiMn<sub>2</sub>O<sub>x</sub>-0.8-400 and NiMn<sub>8</sub>O<sub>x</sub>-0.8-400 after reaction.

Therefore it can be concluded that even though a high surface area, porous nickel manganese oxide was initially used, the catalytic reaction yields the formation of larger metal oxide/metal particles, which eventually results in carbon deposition and catalyst deactivation. The changes in structure and surface composition of the catalyst become more severe by increasing the temperature. Moreover it

## Results and discussion

---

has been observed that there is an optimum amount of active Ni species for each catalytic system, therefore the catalytic activity cannot be further enhanced by simply increasing the amount of respective active material. In case of porous nickel manganese oxide, at low temperature, catalyst with more Ni content shows higher conversion while at higher temperatures the one with lower Ni content is more active, due to its higher stability. Therefore in order to evaluate catalysts regarding their activity and stability performance, the desired temperature window must be taken to account.

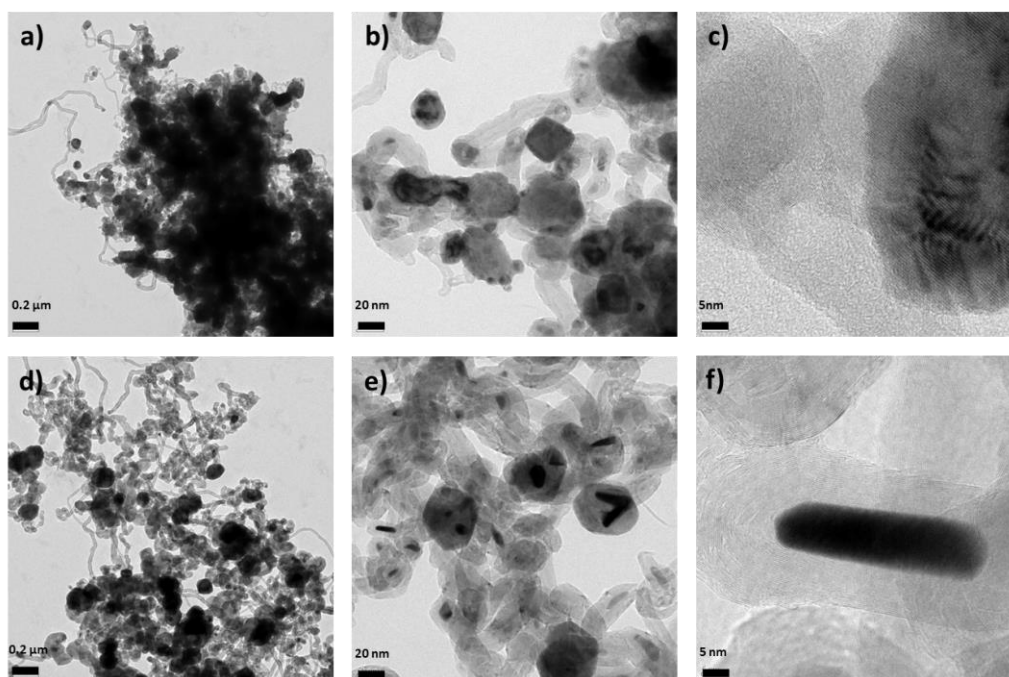


Fig. 2.30: TEM images of a-c) NiMn<sub>2</sub>O<sub>x</sub> after reaction and d-f) NiMn<sub>2</sub>O<sub>x</sub> after reaction at 600 °C.

### 2.8 Supported nickel oxide nanoparticles

As it was shown in the previous chapter, a good catalyst for DRM should be composed of high amount of very small Ni particles, which should be highly dispersed on a robust, high surface area support and thus are stable against agglomeration and sintering. One approach to generate such a catalyst is to start from NiMn oxide solid solution, which forms Ni particles during reaction conditions.

However, a more controlled approach for further studies could start from preformed NiO nanoparticles supported on an inert, preformed high surface area material. Unfortunately, already small metal (Ni) particles of sizes around  $\sim 10$  nm show severe carbon formation, and the synthesis of even smaller NiO or Ni<sup>0</sup> particles is still challenging. However an interesting option would be to start from certain organometallic precursors, which orient/locate a defined amount of Ni atoms in close proximity. Metal cubane molecules are therefore intriguing starting compounds for the preparation of novel DRM catalysts. "Ni<sub>4</sub> cubane" is a tetranuclear complex with di-2-pyridyl ketone [(C<sub>5</sub>H<sub>4</sub>N)<sub>2</sub>CO, dpk] as ligand. Dpk is hydrolyzing into its diol [(C<sub>5</sub>H<sub>4</sub>N)<sub>2</sub>C(OH)<sub>2</sub>, dpd] in aqueous solution. The core of this complex consists of a Ni<sub>4</sub>O<sub>4</sub> cubane, as shown in Fig. 2.23 and 6.12. Therefore this Ni<sub>4</sub> cubane could be described as smallest possible ligand stabilized NiO nanoparticle. Attaching these cubane structures on the surface of the preformed high-surface area supports should, after calcination, yield 4 Ni atoms in close proximity on the supports surface (See Fig. 2.33), which then during catalysis are able to form very small Ni-clusters. (The Ni<sub>4</sub> cubane molecule was synthesized by Johannes Pfrommer, AK Drieß, TU Berlin)

To investigate a possible beneficial influence of the pre-organization of Ni-atoms in the precursor molecule, in a second set of experiments nickel acetate (Ni(OAc)<sub>2</sub>) was used as conventional precursor.

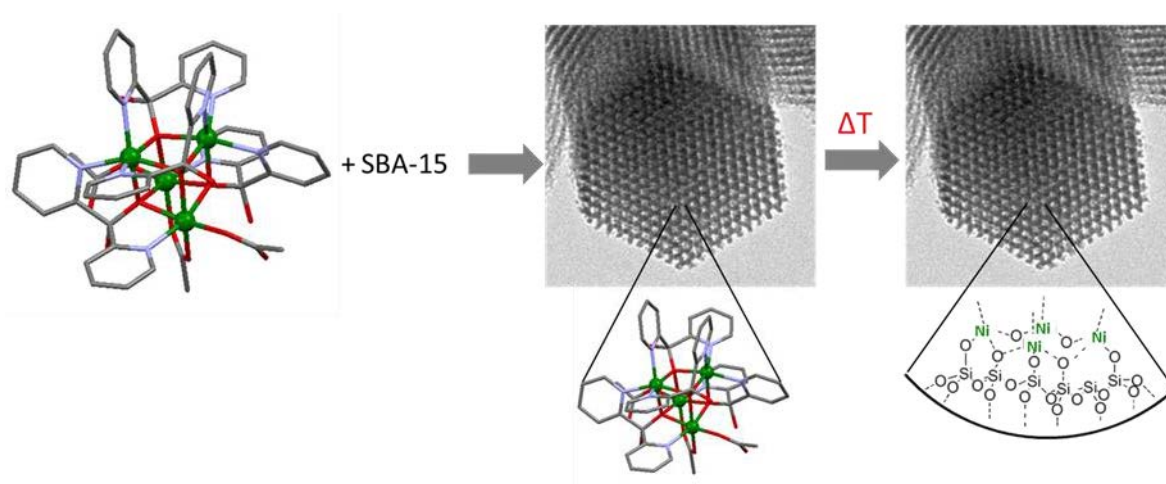


Fig. 2.31: Schematic illustration of the catalyst Ni<sub>4</sub>/SBA-15.

As described elsewhere<sup>[222]</sup>, cubanoid clusters were synthesized by reacting dipyranyl ketone (dpk) with Ni(OAc)<sub>2</sub> under nitrogen atmosphere. The resulting compound was used as precursor for preparation of Ni-based catalyst.

In this study, two series of catalysts, A-Ni<sub>4</sub>/SBA-15 and A-Ni/SBA-15 were prepared using either the Ni<sub>4</sub> cubane molecule or nickel acetate as precursor (A= w% of Ni<sub>4</sub> and Ni). SBA-15 support was impregnated by an aqueous solution of these precursors. The concentration of the precursors in aqueous solution was varied to understand the effect of nickel loading on the morphology and activity of the catalyst. All obtained materials were treated likewise, thus first dried at room temperature, then calcined at 550 °C for 4 h and finally subjected to an in-situ reducing atmosphere (Pure H<sub>2</sub>) at 500 °C for 1 h. The actual metal content of samples was determined by ICP and is presented in table 2.9. Almost in all cases the actual content is lower than the nominal one due to the washing step after impregnation. It must be further noted that the different molecular weight of the Ni precursors does not allow for a straightforward comparison of catalysts prepared from the same initial precursor amount. Therefore in a first step the Ni<sub>4</sub>/SBA-15 and Ni/SBA-15 with increasing Ni amount are separately compared regarding their catalytic performance in DRM, while a comparison between Ni<sub>4</sub>/SBA and Ni/SBA is just made on the later evaluated Ni amount by ICP.

## Results and discussion

**Table 2.9: Characterization and catalytic test results of Ni4/SBA-15 catalyst**

Sample	Ni% <sup>a</sup>	Activity <sup>b</sup>			C% <sup>c</sup>
		500 °C	550 °C	600 °C	
1-Ni4/SBA-15	0.525	3.17449	5.99652	13.89009	0.30
2-Ni4/SBA-15	0.807	3.49341	5.53953	9.72162	1.05
3-Ni4/SBA-15	0.951	3.56432	6.48619	9.68276	1.00
5-Ni4/SBA-15	1.670	3.06177	3.78693	5.31782	5.56

<sup>a</sup>Metal content (wt%) from ICP measurement, <sup>b</sup>Reaction rate of the catalyst based on mole CH<sub>4</sub> converted per mole Ni per time on stream (min), <sup>c</sup>carbon content from elemental analysis.

**Table 2.10: Characterization and catalytic test results of Ni/SBA-15 catalyst.**

Sample	Ni%	Activity		
		500 °C	550 °C	600 °C
1-Ni/SBA-15	0.510	3.84638	3.92656	
2-Ni/SBA-15	0.970	3.00307	5.01469	8.27134
3-Ni/SBA-15	1.306	3.76926	5.25823	6.89796
5-Ni/SBA-15	2.53	1.44247	2.64018	3.41391

<sup>a</sup>Metal content (wt%) from ICP measurement, <sup>b</sup>Reaction rate of the catalyst based on mole CH<sub>4</sub> converted per mole Ni per time on stream (min), <sup>c</sup>carbon content from elemental analysis

## Results and discussion

The powder XRD pattern at low angle provides information about the support structure after impregnation and calcination (Fig. 2.34). Patterns show similar peaks at  $2\theta = 0.98, 1.58$  and  $1.78$ , which are characteristics of the planes (1 0 0), (1 1 0) and (2 0 0) of the hexagonal pore structure of SBA-15 material<sup>[223]</sup>. This shows that the ordered mesoporous structure has been maintained during the metal oxide phase formation.

The wide angle XRD patterns of the samples Ni4/SBA-15 and Ni/SBA-15 after calcination but before reduction are presented in Fig. 2.35. The characteristic peaks for NiO species at  $2\theta = 37.2^\circ, 43.1^\circ$  and  $62.8^\circ$ , corresponding to the planes (111), (200) and (220) of cubic NiO species respectively,<sup>[224,225]</sup> are just observed for sample 5-Ni4/SBA even though the actual Ni-content is smaller (1.67 wt%) than e.g. in sample 5-Ni/SBA (2.53 wt%). Still the observed peaks are very weak and broad pointing to the formation of very small NiO NPs. For the samples with lower loading, hardly any crystal phase can be recognized which might be a sign of the formation of small, highly dispersed Ni species.

Nitrogen physisorption measurements were carried out for the calcined fresh catalysts. Corresponding isotherms show a type IV with characteristic H1-type hysteresis loop for mesoporous materials. These results indicate that the mesoporous structure of SBA-15 was kept in the catalysts after impregnation and calcination (Fig. 2.36).

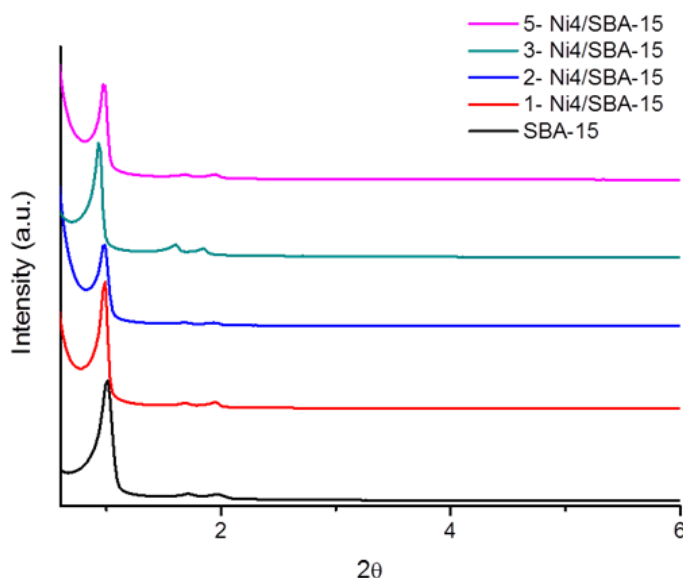


Fig. 2.32: SAXS patterns of Ni4/SBA-15 compounds.

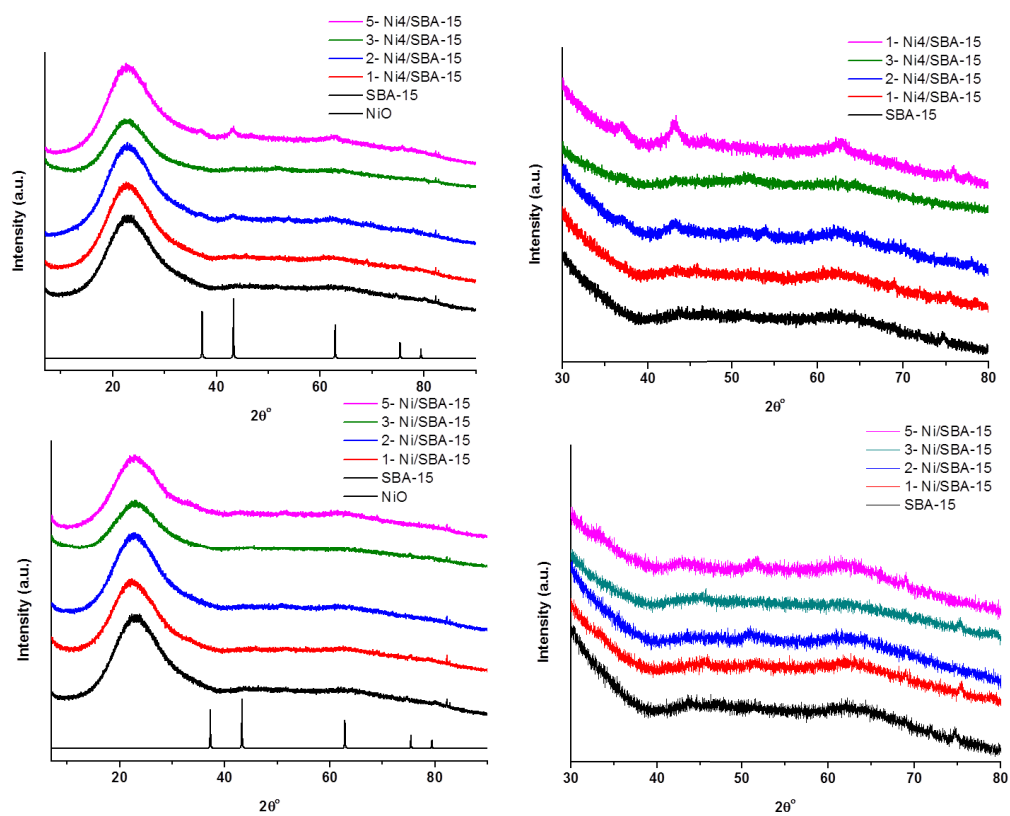


Fig. 2.33: a-b) XRD patterns of Ni<sub>4</sub>/SBA-15 and c-d) Ni/SBA-15.

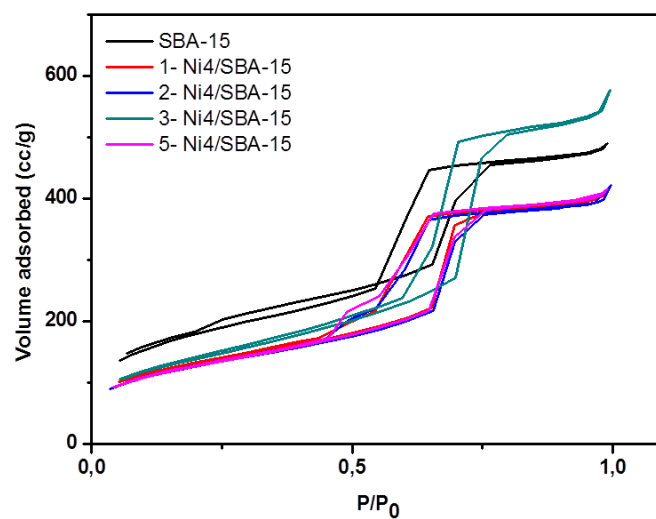
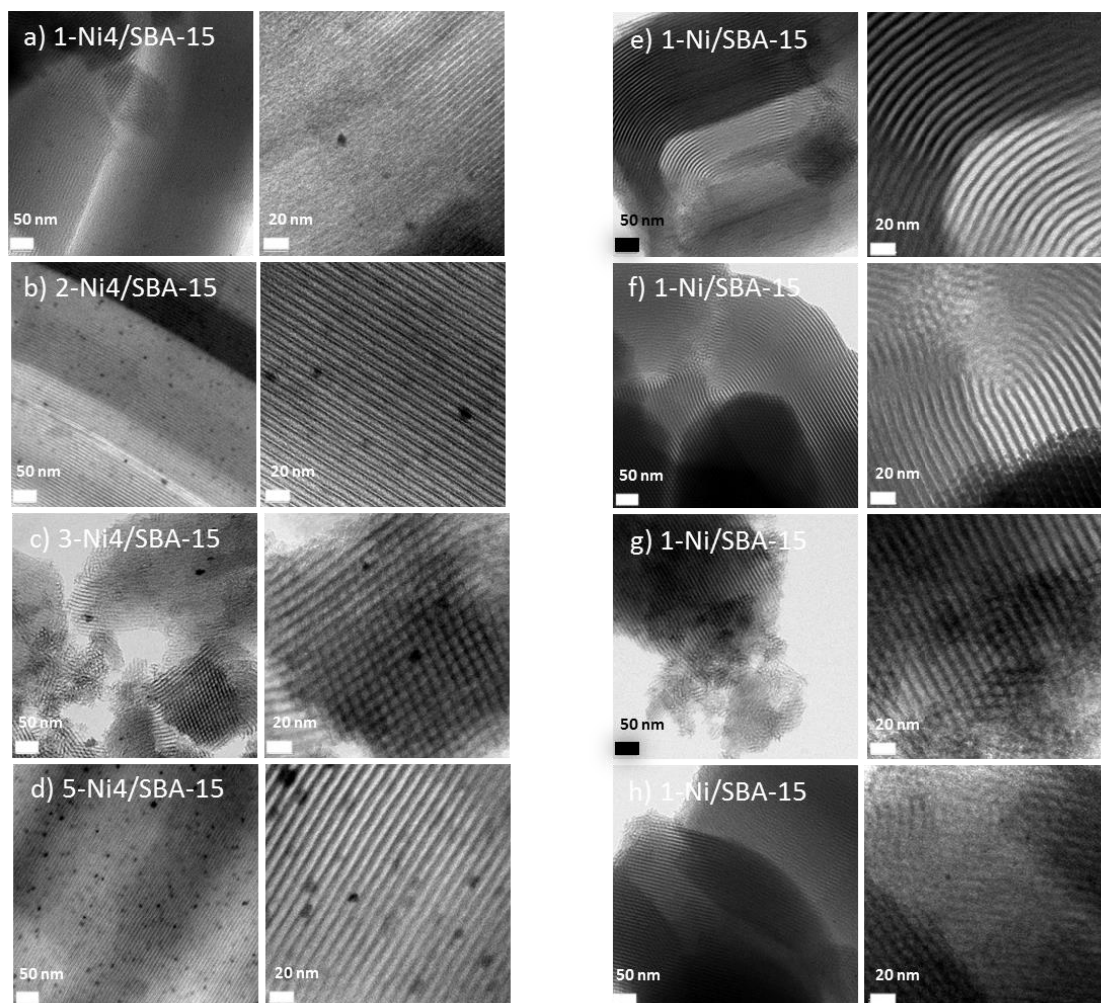


Fig. 2.34: N<sub>2</sub> physisorption isotherm of Ni<sub>4</sub>/SBA-15 series.



**Fig. 2.35:** TEM images of a-d) 1-Ni<sub>4</sub>/SBA-15, 2-Ni<sub>4</sub>/SBA-15, 3-Ni<sub>4</sub>/SBA-15 and 5-Ni<sub>4</sub>/SBA-15, e-h) 1-Ni/SBA-15, 2-Ni/SBA-15, 3-Ni/SBA-15 and 5-Ni/SBA-15 respectively.

Fig 2.37 shows TEM images of the catalysts prepared from different precursors and metal contents. Formation of metal oxide particles can be observed already for the lowest concentration in the Ni<sub>4</sub>/SBA-15 series, while for Ni/SBA-15 metal oxide NPs can just be spotted for the highest concentration (5-Ni/SBA-15). However, only for 5-Ni<sub>4</sub>/SBA-15 a larger amount of small NiO particles are seen which are highly dispersed on the silica support, also supporting the results from the XRD measurements. Most of these metal particles show an irregular shape that might be adapted to the porous structure, formed on the wall or intersection of the support.

### 2.8.1 Catalytic performance of Ni4/SBA-15 and Ni/SBA-15 in DRM reaction

All prepared materials were applied as catalyst for the DRM reaction. Fig. 2.38. shows the methane conversion over Ni4/SBA-15 and Ni/SBA-15 at four different temperatures; 500 °C, 525 °C, 550 °C and 600 °C.

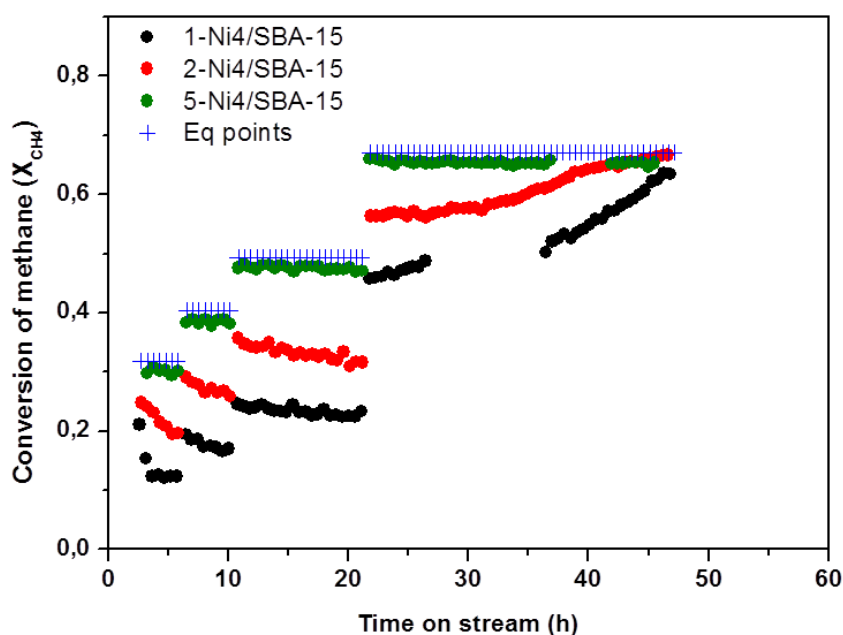


Fig. 2.36: Catalysis result of the 1-Ni4/SBA-15, 2-Ni4/SBA-15, and 5-Ni4/SBA-15 based on methane conversion per gram catalyst, GFSV= 36 L.h<sup>-1</sup>.g<sup>-1</sup>.

The theoretical thermodynamic equilibrium was also calculated by minimizing the Gibbs free energy of all species in the system (See appendix). It should be mentioned that in the presented catalytic results, the conversion of CH<sub>4</sub> is sometimes exceeds the thermodynamic equilibrium limitation due to small differences between the experimental conditions and the theoretical ones. Therefore since the equilibrium is affected by sources of experimental error, it is given here to act only as a practical guideline to determine if the reaction rate is catalytically controlled.

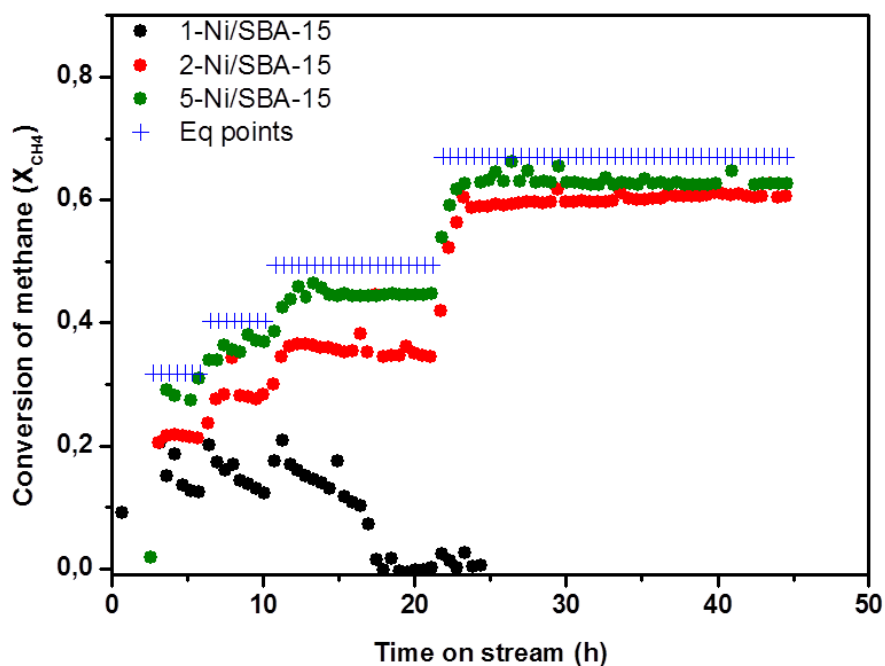


Fig. 2.37: Catalysis result of the 1-Ni/SBA-15, 2-Ni/SBA-15 and 5-Ni/SBA-15 based on methane conversion per gram catalyst, GFSV= 36 L.h<sup>-1</sup>g<sup>-1</sup>.

For the Ni<sub>4</sub>/SBA materials at 500 and 525 °C, the activity is proportional to the amount of nickel in the catalyst. It can be seen that 5-Ni<sub>4</sub>/SBA is an exceptional good catalyst for the DRM reaction reaching thermodynamic equilibrium already at low temperature (500°C) and also shows a stable performance at higher temperature (600°C). Notably, the other Ni<sub>4</sub>/SBA catalysts show initially lower performance and stability, however seemed to get again activated at higher temperatures, especially seen for 1-Ni<sub>4</sub>/SBA. It can be therefore concluded that a certain Ni-cluster size has to be reached to show sufficient catalytic performance in DRM and that for the catalysts with highly dispersed Ni catalysts a certain temperature is needed to form this critical size by particle sintering. As seen from the TEM pictures a considerable amount of particles is just formed in 5-Ni<sub>4</sub>/SBA explaining its high catalytic activity already at low temperatures.

For the Ni/SBA series a similar trend is observed. Just the catalysts with higher amounts of Ni show sufficient activity for DRM reaction. 2-Ni/SBA and 5-Ni/SBA show stable performance even though the thermodynamic equilibrium is not fully reached (Fig. 2.39). Also no further activation at higher temperatures can be observed. Thus comparing these data already a first assumption can be made, that the pre-organization of Ni in the Ni<sub>4</sub>/SBA catalysts has a beneficial effect on the catalytic performance, comparing for example the methane conversions of catalysts 3-Ni<sub>4</sub>/SBA and 2-Ni/SBA which from the ICP measurement have a quite similar Ni amount. Also it can be noted that 5-Ni/SBA

## Results and discussion

which has a much larger Ni content from ICP, still show little lower methane conversion than the best catalyst, 5-Ni4/SBA.

To compare the two catalyst series better than in the above made qualitative assumptions, the reaction rates were presented as mole methane conversion per mole Ni per minute (Fig 2.40, table 2.9 and 2.10). The rate for each catalyst was calculated by averaging over all the activity values at each ramp excluding the first point. The catalysts with the highest loadings showed the lowest rate both in the Ni4/SBA-15 and Ni/SBA-15 series. This can be expected as it has been seen that the largest particles are formed in these catalysts and assuming that just surface Ni atoms are taking part in the catalytic reaction, this will decrease the rate. Moreover a larger deposition of carbon is found for the catalysts with higher Ni amount which also can yield to a lower accessibility of the Ni atoms and thus also lower the reaction rate.

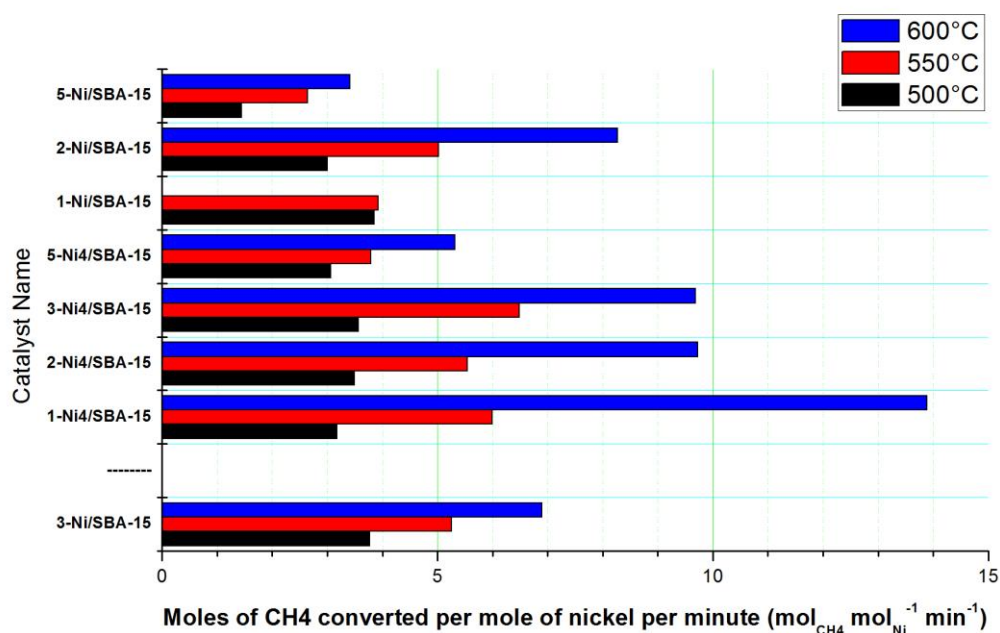


Fig. 2.38: Catalysis result based on mole methane converted per mol catalyst per minute.

For the same reasons the catalysts with lower Ni amount show higher rates especially seen for 1-Ni4/SBA. The rate especially at higher temperatures of the Ni4/SBA series are much higher than for the Ni/SBA series, proving the beneficial effect of the application of the pre-organized Ni-precursor, which faster forms small but highly, dispersed NiO and later Ni-clusters. It can thus be assumed that a certain metal cluster size has to be reached to yield high methane conversions. The Ni4O4 cubane precursor seems to combine two advantages, by first allowing the fast formation of first Ni-clusters,

which are however still highly dispersed on the support and thus quite stable during the catalytic reaction.

As the here discussed catalysts are based on Ni, which is a cheap and abundant metal, the results for the reaction rate are of course important for elucidation of the influences of particle amount and sizes on the catalytic activity, but not so much for practical applications. Thus it can be concluded that especially catalysts 5-Ni4/SBA and to a somewhat lesser extent 5-Ni/SBA are very active and stable catalysts for the DRM reaction within the temperature window of 500-600°C.

### 2.9 Coated Ni-based catalysts

As mentioned before from a practical and industrial point of view catalyst deactivation must be avoided, as otherwise they must be regenerated or replaced. Moreover, in this case the whole processes have to be shut down while these steps are taken<sup>[226]</sup> which makes the whole process very costly. Therefore tremendous efforts have been undertaken to enhance the stability of metal catalysts. Passivating the active metal with traces of sulfur, triphenylphosphites, tin, bismuth<sup>[227-231]</sup>, formation of alloys<sup>[228,229,232-234]</sup> or coke removal through gasification<sup>[182,229]</sup> are the techniques applied so far to decrement coke formation during hydrocarbon reactions. There are a few reports presenting strategies such as chemical vapor deposition, dendrimer encapsulation, or grafting to form a shell out of mesoporous silica,<sup>[77,78]</sup> tin oxide,<sup>[235]</sup> zirconia,<sup>[82]</sup> or ceria,<sup>[236]</sup> around metal NPs to prevent them from sintering, particularly above the Tammann temperature (half of the bulk melting point in degrees kelvin). These examples, usually leads in the formation of a metal oxide shell with poorly controlled thickness (usually tens of nanometers thick), around the metal NPs. All these methods can inhibit coke formation and sintering of metal NPs however often on cost of catalytic activity. Thus catalytic activity, most of the time, decreases after shell formation (usually thicker than desired) due to hindered access of the active metal sites, i.e. mass transfer limitations.

As mentioned before the catalytic performance of a metal catalyst, including reactivity and stability, could be influenced by the nature of the oxide supports<sup>[175,237-239]</sup>. The role of the metal/oxide interface sites in heterogeneously catalyzed reactions can be studied via comparing the reactivity of metal NPs supported on different metal oxides (regular catalysts) or by dispersing metal oxide NPs on large area metal surfaces (inverse catalysts)<sup>[240-242]</sup>. Moreover the less traditional inverse catalysts may give the opportunity to tune the catalytically active sites of the bulk metal oxides by partially coverage of their surface with protecting layers and utilize them as catalyst instead of supported, well dispersed nanoparticles which are usually hard to prepare and maintain in reactions perform at elevated temperatures such as DRM. Therefore in this part of the thesis commercially available nickel

nanoparticles (Ni) and nickel oxide (NiO) nanopowder were used as precursors for preparation of coated Ni-based catalysts for DRM reaction.

For DRM, Al<sub>2</sub>O<sub>3</sub> was considered to be an excellent supporting material due to its basicity, promoting a high conversion of CO<sub>2</sub>. Here, two series of alumina coated Ni-based catalysts were prepared using atomic layer deposition (ALD), and catalytic DRM reactions at four different temperatures over uncoated and Al<sub>2</sub>O<sub>3</sub>-coated catalyst were investigated using a fixed-bed reactor (Catalytic tests were done by Patrick Littlewood in the group of Prof. Schomaeker). The Al<sub>2</sub>O<sub>3</sub> overcoats were synthesized using sequential exposures to trimethyl aluminum (TMA) and water vapors. Different numbers of Al<sub>2</sub>O<sub>3</sub> ALD cycles (5-20) were performed to generate protective layers of progressively increasing thickness on the NiO nanopowder and Ni NPs catalysts.

### 2.9.1 ALD-formed alumina overcoat

Al<sub>2</sub>O<sub>3</sub> ALD performed using TMA and water is one of the most investigated and successful ALD procedures.<sup>[243–247]</sup> The mechanism of Al<sub>2</sub>O<sub>3</sub> ALD on oxide surfaces is well understood (Fig. 2.41):

1. TMA reacts with hydroxyl groups on the starting surface forming Al(CH<sub>3</sub>)<sub>x</sub>\* (x =1–2, where the asterisk designates a surface species) and CH<sub>4</sub>.
2. A purge or evacuation by an inert gas like nitrogen to remove the nonreacted reactants and the gaseous reaction by-products.
3. the Al(CH<sub>3</sub>)<sub>x</sub>\* terminated surface transforms to an Al(OH)<sub>x</sub>\* (x =1–2) terminated surface after the following H<sub>2</sub>O exposure and again releases CH<sub>4</sub>
4. After the formation of a monolayer on the substrate, excess precursors are purged by the inert gas.

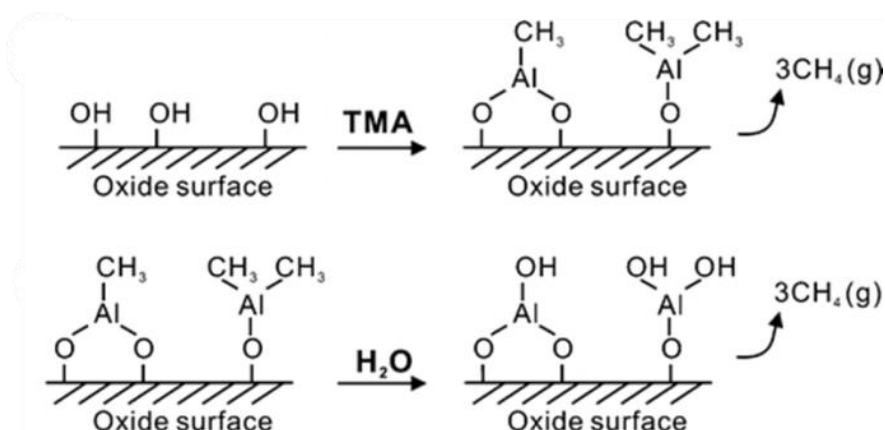


Fig. 2.39: Schematic illustration of one  $\text{Al}_2\text{O}_3$  ALD cycle on a metal oxide surface.<sup>[248]</sup>

The film growth occurs in a layer by layer mode. TMA reacts with surface hydroxyl groups; the reaction stops after the complete coverage of the surface and the excess TMA is removed during the purging process. Then,  $\text{H}_2\text{O}$  reacts with surface methyl groups until all of them have reacted to hydroxyl group and the surface reaction is completed. These cycles are repeated until the target film thickness is achieved. Recently ALD  $\text{Al}_2\text{O}_3$  protective layers with precise thicknesses were utilized to inhibit the sintering of supported ALD formed Pd NPs. The catalytic performance of the resulted material was tested in the methanol decomposition reaction.<sup>[63]</sup> The catalytic activity of the  $\text{Al}_2\text{O}_3$  protected Pd NPs was maintained or even slightly enhanced up to a certain thickness. Using CO as a probe molecule, Stair et al. found out that the ALD alumina overcoats prefer to nucleate at corners, steps, and edges of the Pd NPs. Therefore the uncovered Pd(111) facets are accessible for methanol conversion. It has been shown that catalyst deactivation due to sintering or coke formation could be effectively prevented by alumina overcoats with thickness of 8 nm.<sup>[248]</sup> The same process might be applicable for the protection of other supported/unsupported nanoparticles or porous materials with catalytic application in reactions performed at elevated temperatures.

### 2.9.2 Alumina overcoated Ni nanoparticles

Commercially available Ni nanoparticles (20-100 nm, based on TEM images) were purchased and used as source of nickel and covered by 5, 10, 15 and 20 cycles of  $\text{Al}_2\text{O}_3$  ALD. Although the mechanism for alumina ALD on oxide surfaces requires surface hydroxyls, there are some reports presenting growth of alumina ALD on noble metal surfaces. For instance, subnanometer thick ALD-formed alumina layer were formed on Ag NPs by Zhang et al.<sup>[249]</sup> It has been suggested by Whitney et al. that the alumina ALD initiates when TMA decomposes on the Ag surface.<sup>[250]</sup> Although this reaction

## Results and discussion

has not been studied in detail, it has been found that TMA reacts with Ni(111) to form a monolayer of  $\text{Al}(\text{CH}_3)_2$  and  $\text{CH}_3$  surface species even at a low temperature of 110 K.<sup>[251]</sup>

XRD patterns of uncoated and coated Ni NPs showed the typical peaks for Ni metal phase (Fig. 2.42). The gradual change in aluminum content of the coated Ni NPs by increasing the number of alumina ALD can be observed by ICP and is presented in table 2.11. The commercial Ni NPs have a surface area of  $14.3 \text{ m}^2 \cdot \text{g}^{-1}$  based on  $\text{N}_2$  physisorption measurement. The surface did not change after coating even with 20 cycles of alumina ALD, suggesting the formation of thin layer of alumina around the particles and probably no agglomeration during the coating process. TEM images show the presence of a thin ( $\sim 4 \text{ nm}$ ) alumina layer around Ni particles after 20 cycles of ALD (Fig 2.43).

**Table 2.11: Characterization of uncoated and coated Ni NPs.**

Name	Number of cycles	SBET ( $\text{m}^2 \cdot \text{g}^{-1}$ )	Crystal phase <sup>a</sup>	Al%c
Ni	-	14.3	Ni	0
Ni-5	5	14.2	Ni	2.29
Ni-10	10	13.7	Ni	2.96
Ni-15	15	13.9	Ni	5.65
Ni-20	20	13.3	Ni	7.19

<sup>a</sup>Crystallin phase as deduced from XRD patterns, <sup>c</sup>Metal content (wt%) based on ICP results

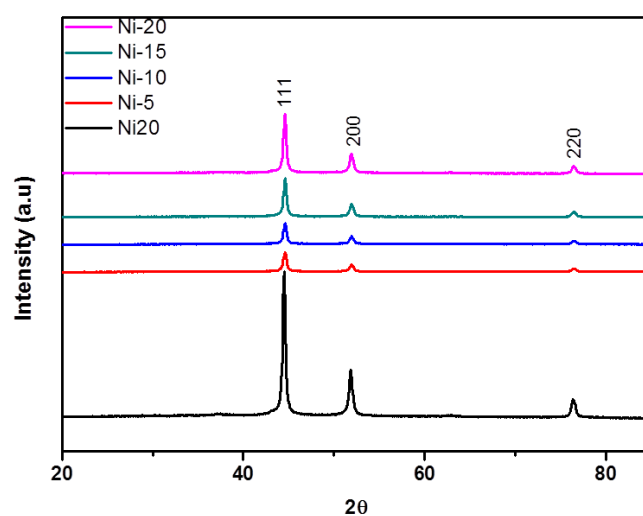


**Fig. 2.40: XRD patterns of uncoated and coated Ni NPs.**

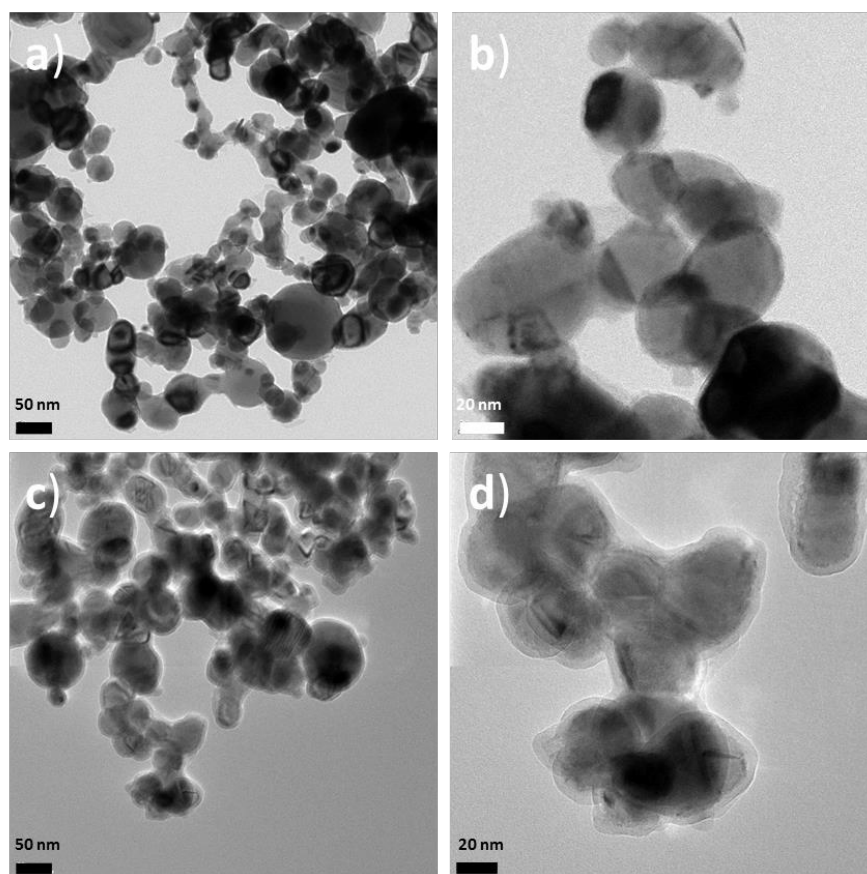


**Fig. 2.41:** TEM images of a,b) uncoated Ni NPs, c,d) Ni NPs coated with 20 cycles of alumina ADL.

### 2.9.2.1 Catalytic test on alumina coated Ni NPs

DRM experiments of uncoated and alumina coated Ni NPs were carried out in a fixed-bed reactor with a reagent gas mixture ( $\text{CH}_4:\text{CO}_2:\text{He} = 1:1:8$ ). The catalytic reaction was performed at four different temperatures, 500, 600, 700 and 800 °C over 10 mg catalyst. The reactor temperature was kept constant for one hour at each ramp. Every 10 min, change in volume ratio of each gas ( $\text{CH}_4$ ,  $\text{CO}_2$  or  $\text{CO}$ ) in the outlet of the reactor was monitored using an on-line GC system. Catalytic activity was observed in terms of conversion of reactant gases and stability was monitored in terms of activity drop over time. The effect of the number of alumina ALD cycles and temperature on the activity and stability of the catalysts were studied. Subsequent analysis of carbon formation on the surface of the catalyst material after the reaction was also conducted.

It has been described before that DRM reaction is accompanied by methane dissociation above 640 °C. On the other hand above 820 °C RWGS and Boudouard reactions do not occur. Methane dissociation and Boudouard reactions are the responsible reactions for the carbon formation in the

## Results and discussion

temperature range of  $\sim 550\text{--}700\text{ }^{\circ}\text{C}$ .<sup>[252]</sup> Therefore carbon deposition will be decreased in the DRM reaction at temperatures higher than  $700\text{ }^{\circ}\text{C}$ . However, particle sintering is a major problem at this temperature range ( $>700\text{ }^{\circ}\text{C}$ )

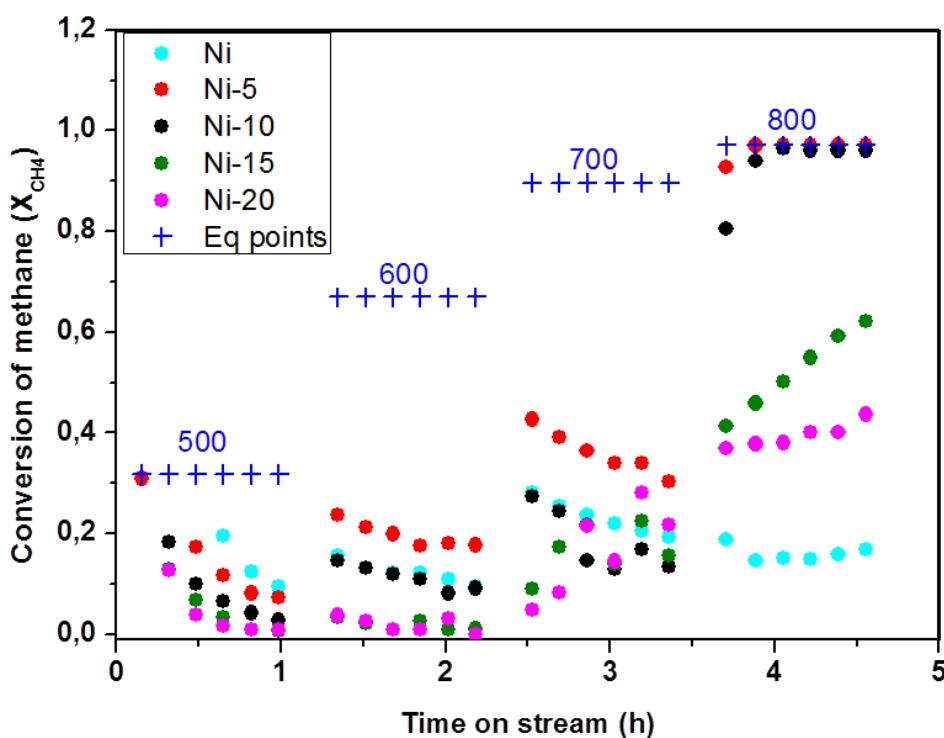


Fig. 2.42: CH<sub>4</sub> conversion over 10 mg of uncoated Ni, Ni-5, Ni-10, Ni-15 and Ni-20 at 500, 600, 700 and 800 °C, GHSV =  $180\text{ Lh}^{-1}\text{g}_{\text{cat}}^{-1}$ .

Uncoated Ni nanoparticles showed high catalytic activity at the beginning of the reaction, but deactivated strongly by time on stream especially at higher temperatures (700 and 800 °C). Alumina coated Ni NPs showed low catalytic activity and stability at the temperature range of 500-700 °C probably due to severe carbon formation on the large Ni-NPs. However, as expected, all catalysts showed enhanced catalytic activity at 800 °C (Fig 2.44). In case of Ni-5 and Ni-10 the activity reached the equilibrium limiting point for DRM reaction at 800 °C. At lower temperature (500-700 °C) CO<sub>2</sub> conversion ratio was higher than that of CH<sub>4</sub> over alumina overcoated catalyst, whereas consumption of each reagent gas (CO<sub>2</sub> and CH<sub>4</sub>) was almost the same on Ni-5 and Ni-10 at 800 °C. A higher consumption of CO<sub>2</sub> than CH<sub>4</sub> on alumina covered NiO catalyst at lower temperatures may be due to the reverse water-gas shift (RWGS:  $\text{CO}_2 + \text{H}_2 \rightarrow \text{CO} + \text{H}_2\text{O}$ ) reaction over the surface of the catalyst, which is a well-known side reaction in the DRM. Ni-10 and Ni-20 also showed increasing trend

## Results and discussion

---

despite their lower catalytic activity compared to Ni-5 and Ni-10. The lower activity of the coated Ni NPs with higher number of layers, most probably results from mass transfer limitations caused by the thicker alumina overcoat.

### 2.9.3 Alumina coated NiO nanopowder

Overcoats with 5, 10, 15 and 20 cycles were also applied to NiO nanopowders because they are commercially available as high surface area powder with smaller particles (~50nm) than the former used Ni particles and are transformed anyway during pre-treatment into Ni-particles. XRD patterns of the nanopowders before and after coating showed the typical pattern of nickel oxide phase (Fig. 2.45). N<sub>2</sub> physisorption was performed on the uncoated and coated samples (Table 2.12). The BET measurements on the uncoated nanopowder yield a surface area of 99.2 m<sup>2</sup>.g<sup>-1</sup>. After 5 cycles of alumina ALD, the surface area reduced to 51 m<sup>2</sup>.g<sup>-1</sup>. Decrease in the surface area becomes more pronounced by increasing the number of alumina ALD cycles. This gradual decrease by increasing of ALD cycles as well as alumina content of the samples (Table 2.12) could be a consequence of partial filling of the nanopowder voids by alumina layers. The morphology of the Ni nanopowders before and after coating was studied by transmission electron microscopy (TEM). Alumina overcoat with the thickness around 8 nm for NiO-20 sample which has been covered by 20 cycles of alumina ALD can be observed from the TEM images (Fig. 2.46 and 2.47).

**Table 2.12: Characteriation of the alumina coated Ni nanopowder.**

Name	Number of cycles	S <sub>BET</sub>	Crystal phase	Al%
NiO	0	99.2	NiO	0
NiO-5	5	51.0	NiO	9.30
NiO-10	10	31.9	NiO	14.85
NiO-15	15	23.6	NiO	17.25
NiO-20	20	16.2	NiO	20.40

<sup>a</sup>Surface area of oxides ( m<sup>2</sup>.g<sup>-1</sup>), <sup>b</sup>Crystalline phase as deduced from XRD patterns, <sup>c</sup>Metal content based on ICP results

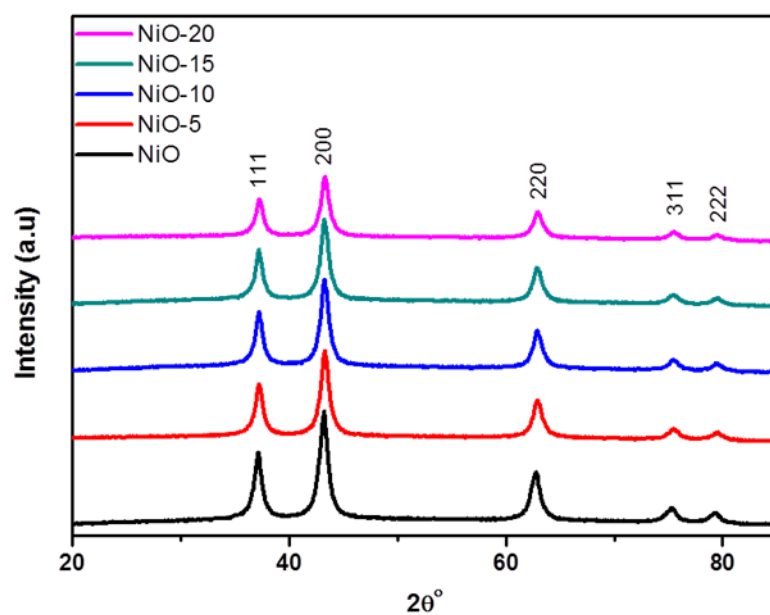


Fig. 2.44: XRD patterns of uncoated and coated Ni nanopowders.

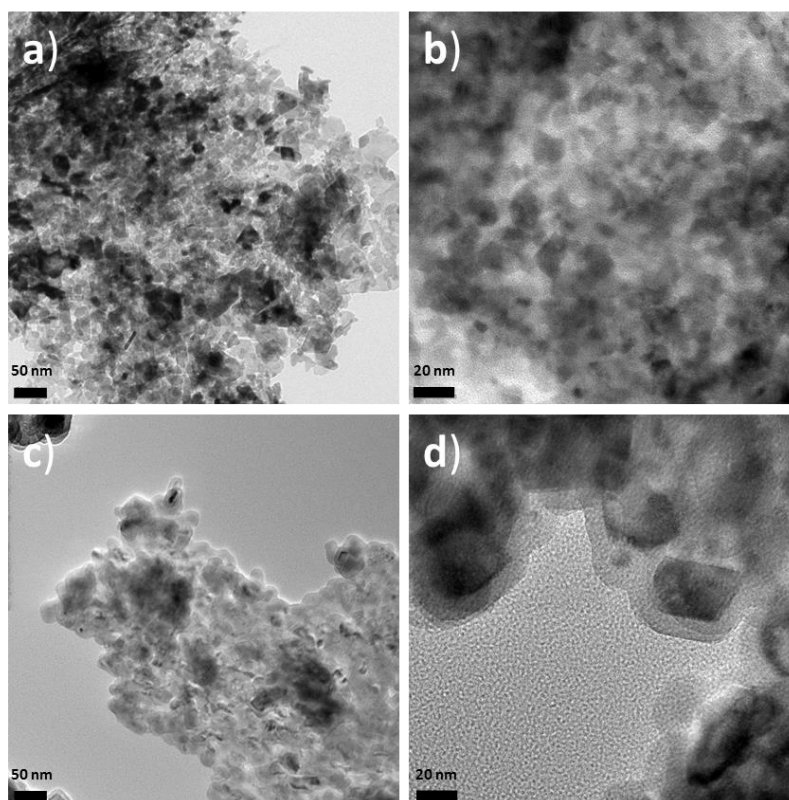


Fig. 2.43: TEM images of a,b) uncoated NiO nanopowder, e,f) coated with 20 cycles of alumina ALD (Ni-20).

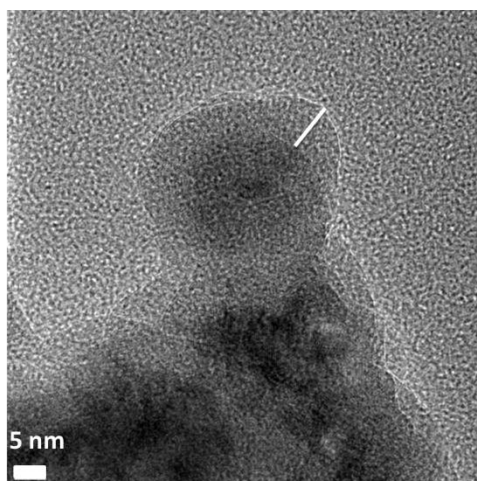


Fig. 2.45: TEM image of ALD-formed alumina overcoat on Nickel oxide (NiO-20) with the thickness of around 8 nm.

### 2.9.3.1 Catalytic test on NiO nanopowder

The uncoated NiO sample (20 mg) showed sharp decrease in conversion just after 30 min time on stream and the conversion stayed low till the end of the reaction. As shown in fig. 2.48, 1 mg NiO-5, which is the nickel nanopowder coated with 5 cycles of alumina ALD, showed 26% CH<sub>4</sub> conversion at the beginning, but decreased to 15% over one hour reaction. By increasing the temperature to 600 and 700 °C, the methane conversion also increased to 51% and 82% respectively. The catalyst again showed some signs of deactivation at 600 but was almost stable at 700 °C. The highest catalytic conversion and also stability was seen at 800 °C.

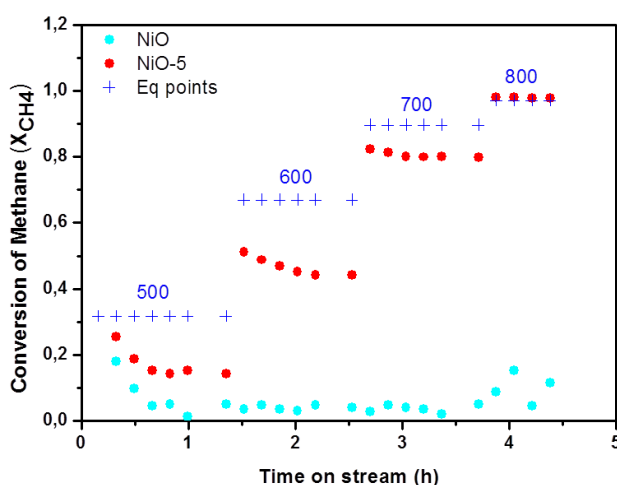


Fig. 2.46: CH<sub>4</sub> conversion over uncoated NiO nanopowder (20 mg) and alumina coated NiO-5 sample (1 mg) at 500, 600, 700 and 800 °C, GHSV= 3600 Lh<sup>-1</sup>g<sub>cat</sub><sup>-1</sup>.

## Results and discussion

In order to find out the main source of NiO-5 deactivation at lower temperature as well as its high activity and stability at higher temperature, long-term DRM reaction at 525 °C and 800 °C were carried out for this catalyst. Fig. 2.49 shows the screening result of 1.94 mg of NiO-5 catalyst at 525 °C. A CH<sub>4</sub> conversion of 35% was seen at the beginning but it dropped down to 20% during 12 h. Based on TPO (temperature programmed oxidation) result, 19.9 mg carbon was produced per mg catalyst suggesting that severe carbon deposition is the main reason for catalyst deactivation at 525 °C. The DRM reaction at 800 °C was also performed for 12 h in presence of 0.55 mg NiO-5 as catalyst (Fig. 2.50). It is observed that even in presence of such a low amount of catalyst (0.55 mg) the conversion reached the thermodynamic equilibrium point of DRM reaction at 800 °C.

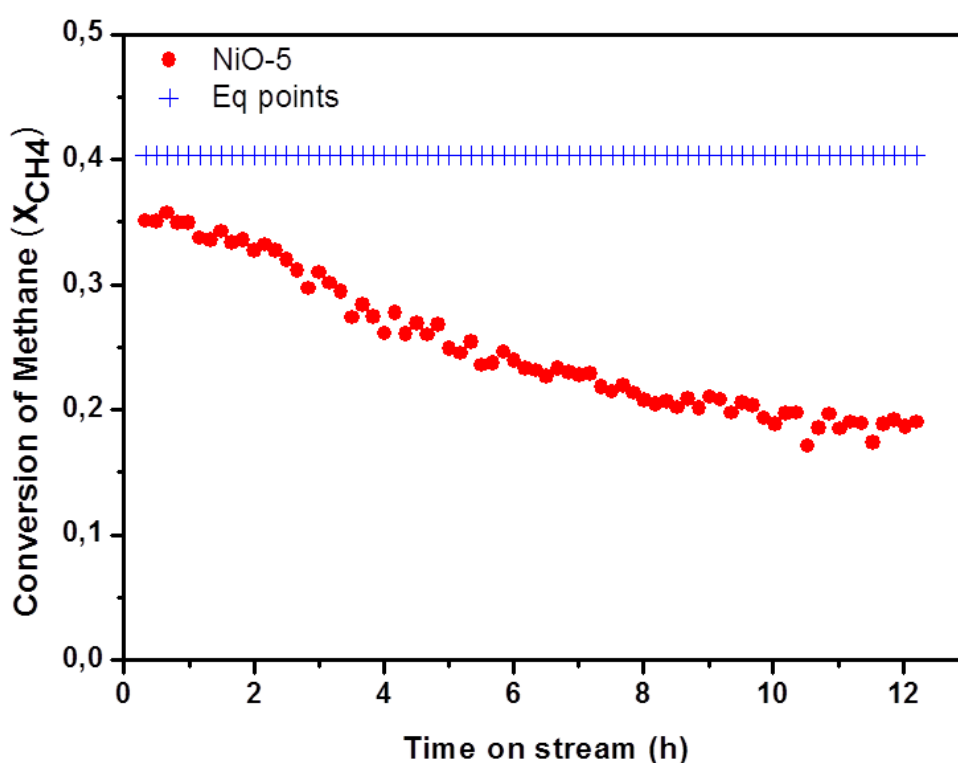


Fig. 2.47: CH<sub>4</sub> conversion over NiO-5 (1.94 mg) at 525 °C, GHSV= 928 Lh<sup>-1</sup>g<sub>cat</sub><sup>-1</sup>.

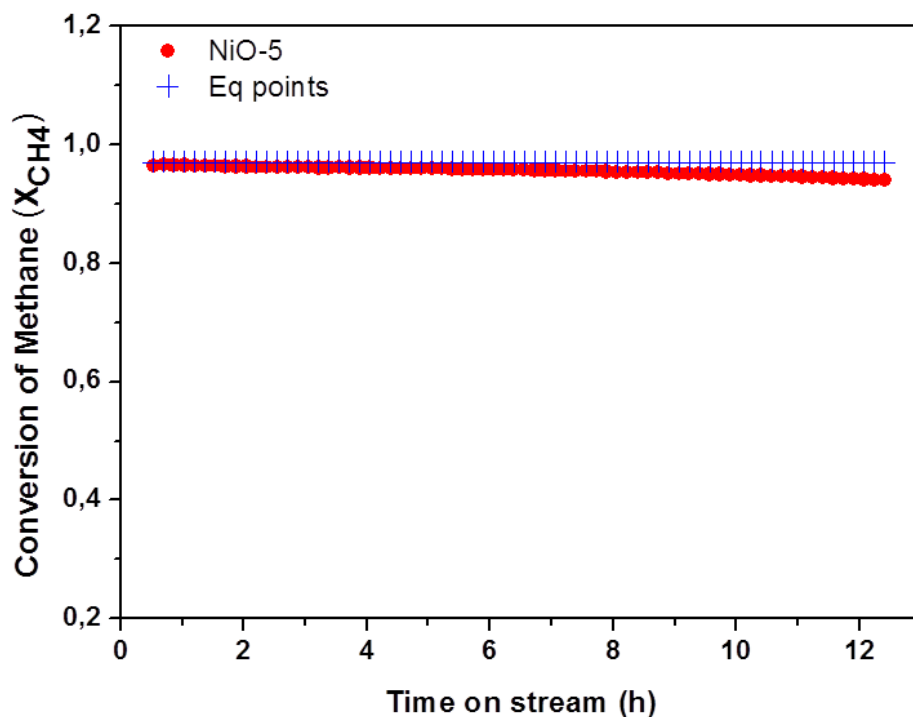


Fig. 2.48: CH<sub>4</sub> conversion over NiO-5 (0.55 mg) at 800 °C, GHSV= 6545 Lh<sup>-1</sup>kg<sub>cat</sub><sup>-1</sup>.

Therefore, it can be concluded that 5 cycles of ALD-formed alumina overcoat can protect Ni nanoparticles formed in the NiO-5 catalyst from sintering at temperature as high as 800 °C and result in high as well as stable methane conversion.

The methane conversion results obtained using alumina overcoated NiO catalysts prepared with different number of alumina ALD cycles are presented in Fig. 2.51. The catalyst prepared with 10 cycles, NiO-10, achieved a lower methane conversion at 600 and 700 °C but similar conversion at 500 and 800 °C in comparison to NiO-5. At 500 °C and 800 °C severe carbon deposition and thermodynamic equilibrium control the activity of both catalysts respectively, therefore no difference can be seen in their activity. But at 600 and 700 °C, NiO-10 with a thicker alumina overcoat shows lower activity, most probably due to mass transfer limitations.

NiO-20 showed lower conversion at 525 °C compared to NiO-5, however only 0.42 mg carbon per mg catalyst were produced during the 12 h time on stream, showing that the alumina overcoat can also prevent carbon formation besides the protection against sintering.

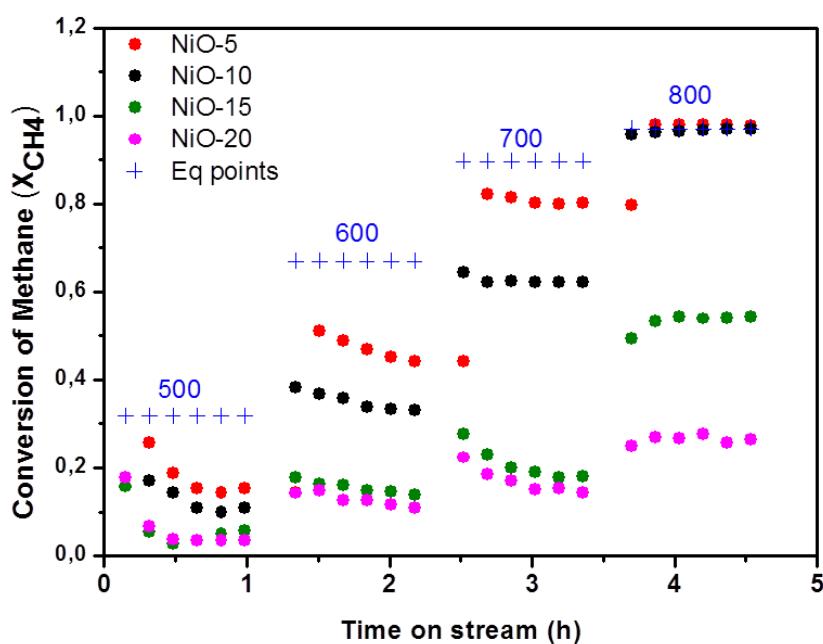
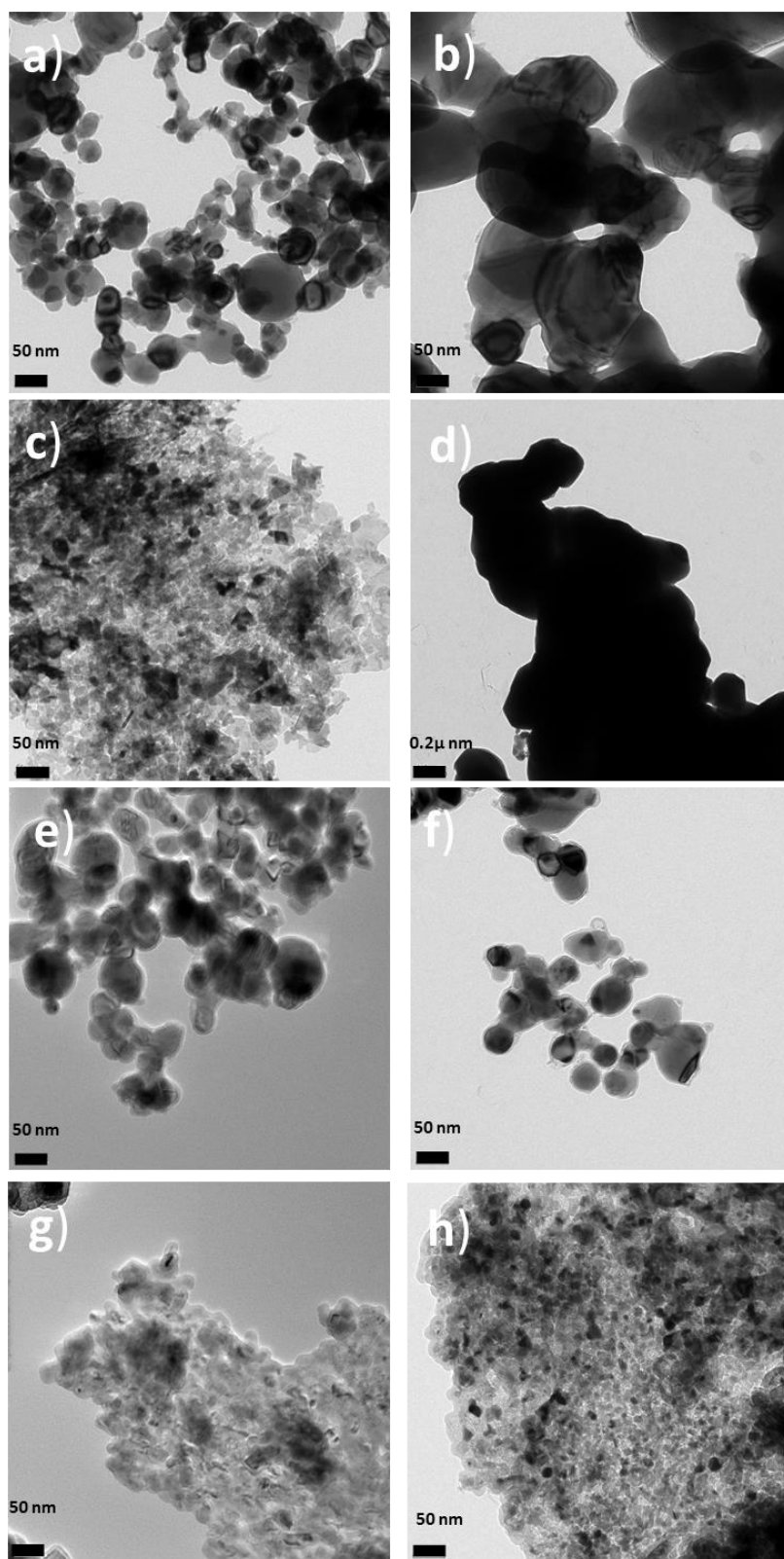


Fig. 2.49 CH<sub>4</sub> conversion over 1mg of NiO-5, NiO-10, NiO-15 and NiO-20 at 500, 600, 700 and 800 °C, GHSV= 3600 Lh<sup>-1</sup>g<sub>cat</sub><sup>-1</sup>.

The fact that the Ni surfaces are still accessible to the methane and the CO<sub>2</sub> molecules even after 5 to 20 ALD cycles indicates that the Al<sub>2</sub>O<sub>3</sub> overcoats are porous. Experimental and theoretical (DFT calculations) studies showed that in case of alumina overcoat on Pd NPs with TMA, -CH<sub>3</sub>\* surface species formed after TMA deposition inhibit further TMA chemisorption. This inhibition results in discontinuities in the alumina film and introduces porosity.<sup>[248,253–255]</sup> The porosity of the ALD-formed alumina overcoats could be enhanced via high temperature treatment or prolonged reaction at elevated Temperatures. Therefore nickel-based catalyst might be modified by modulating the porosity of the alumina overcoats.

From the catalytic activity trend it can be seen that for NiO and Ni NPs, 5 cycles of alumina ALD is the optimum number of cycles to cover the nanostructures and protect them from sintering at elevated temperatures, while maintaining their high catalytic activity. Fig. 4.52 proofs this assumption showing the morphology changes in NiO and Ni NPs, with and without alumina layers occurring after a reduction step under hydrogen while heating at 500 °C for 1 h. While the particle size of alumina coated Ni and NiO remained almost unchanged, severe agglomeration and sintering happened in uncovered Ni and NiO materials.



**Fig. 2.50:** images of Ni-NPs a) before and b) after reduction, NiO NPs c) before and d) after reduction, Ni-20 e) before and f) after reduction, NiO-20, g) before and h) after reduction.



### 3. Summary and outlook

The research presented in this thesis investigated the use of varied types of synthetic approaches to form metal oxides nanostructures capable of catalyzing water oxidation reaction and dry reforming of methane.

Calcium manganese oxides were prepared by templating method. Using cyanamide as porogen resulted in porous CaMn oxides. Different amounts of cyanamide and varied calcination temperatures were tried in order to find the optimum synthetic parameters. Moreover the feasibility of the cyanamide-based protocol for the preparation of binary transition metal oxides was investigated. A detailed analysis showed that:

- Cyanamide or more probably one of its condensation and decomposition products acts as porogen and foam-like porous CaMn oxides are formed.
- Analysis of crystal and atomic structure of the resulting CaMn oxides show that besides pore formation and surface area, cyanamide strongly influences also the prevalent Mn oxidation state, the atomic structure, and the level of amorphicity.
- The prepared calcium manganese oxide materials feature an amorphous birnessite-like structure. This structure is build up from layers of edge-sharing  $\text{MnO}_6$  octahedra with calcium cations intercalated in between. This structure contains a large number of layer defects.
- Mn ions in oxidation states between  $\text{Mn}^{3+}$  and  $\text{Mn}^{4+}$  are interconnected by  $\mu$ -oxido and  $\mu$ -hydroxido bridges.
- Open coordination sites which are present in the amorphous structure may act as binding sites for substrate water molecules.

It is generally assumed that all the above mentioned factors (Mn oxidation states, the atomic structure and the level of amorphicity) can influence the catalytic activity of CaMn oxides for water oxidation, while the surface area seems to be no decisive factor for the activity of amorphous materials (Fig 6.13).

Cyanamide–base protocol was also successfully employed for the preparation of nickel, manganese and cobalt oxides. The resulting porous metal oxides were active catalysts for water oxidation reaction.

In summary, the presented findings show that porous manganese-based oxides (calcium manganese and manganese oxides) are outstanding catalysts for water oxidation reaction. These materials are

## Summary and outlook

---

composed of cheap and abundant elements, which make them also promising candidates to catalyze the water-oxidation half-reaction in an artificial photosynthetic process. However, in this case the use of oxidant like  $\text{Ce}^{4+}$  should be replaced with multi-junction semiconductors to perform light-driven water splitting. First step towards this target would be the preparation of catalytically active electrodes which then be coupled to the light-harvesting units. Some promising results on deposition of manganese-based materials have recently been published.<sup>[152,260,261]</sup>

In the second part of the project, the same templating protocol based on cyanamide as well as other synthetic routes, such as impregnation and atomic layer deposition were used for the preparation of nickel-based materials as catalyst for dry reforming of methane.

Cyanamide-based method resulted in porous nickel manganese oxides with significant catalytic activity. Three catalysts were prepared with different amount of Ni content,  $\text{NiMn}_2\text{O}_x$ ,  $\text{NiMn}_6\text{O}_x$  and  $\text{NiMn}_8\text{O}_x$ . Catalytic test results showed that there is an optimum amount of active Ni species for each catalytic system; therefore the catalytic activity cannot be further enhanced by simply increasing the amount of respective active material.

Supported nickel oxides were prepared via impregnation of SBA-15 support by aqueous solution of Ni precursors. It has been demonstrated that highly dispersed Ni NPs which has been formed using a tetranuclear cubane molecule as a pre-organized Ni-precursor is a very active and stable catalyst for DRM reaction at low temperature (500-600 °C).

For performing DRM reaction at elevated temperatures with high conversion, coated Ni/NiO nanostructures were prepared employing atomic layer deposition (ALD) technique. Alumina overcoated Ni-based materials showed impressive activity and stability at elevated temperatures (700-800 °C). It has been shown that, the stabilization against sintering at high temperature is a crucial factor explaining the high catalytic activity of alumina coated Ni-NPs in comparison to the non-coated samples. Although the role of alumina cover in producing active carbon-based intermediates which can be converted into CO cannot be ruled out.

Considering the high activity and stability of the dry reforming catalysts studied in this research the possibility for further exploration into these new materials is numerous, including:

- Further research into the use of various dopants in Ni-based materials, and the beneficial effects that these may have on activity and stability within the dry reforming reaction, through improving the distribution and Ni-support interaction of the materials.
- Using heterobimetallic cubane molecules as single-source precursors instead of monometallic ones to spontaneously deposit both active species and dopants, on the

supports with high surface area. The deposition of Ni<sub>3</sub>Mn cubane molecule on SBA-15 is already under investigation and some promising results have been achieved.

- The interesting beneficial coating effects of the alumina should be explored across various other previously reported materials that show promise as catalyst support within the dry reforming reaction. One candidate would be zirconia which already showed positive effects on the performance of Ni-based catalysts as both dopant and support. Zirconia coated Ni structure could be prepared via forming a zirconia shell around a Ni@SiO<sub>2</sub> core-shell material, and then leaching the silica core leaves the Ni@ZrO<sub>2</sub> behind. Fig. 3.1 presents the TEM images of Ni NPs and Ni@SiO<sub>2</sub> nanostructures which have been prepared in the Thomas group so far. This route gives us the opportunity to use Ni NPs with the size as small as 5 nm. Zirconia coating and removing the silica shell is under investigation. Recently Kawi et al. presented the Ni-core@Ni@SiO<sub>2</sub> nanocomposite as catalyst for the DRM reaction at 800 °C. This result suggests that replacing silica by zirconia with better thermal stability and neutral nature may leads in a more active and stable catalyst.<sup>[262]</sup>

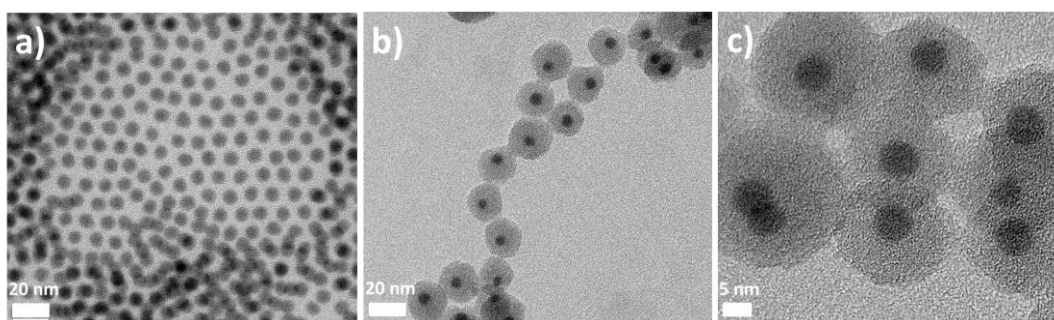


**Fig. 3.1:** TEM images of a) Ni NPs, b) and c) Ni@SiO<sub>2</sub> nanostructures.

## 4. Experimental

### 4.1 Synthesis of $\text{CaMn}_2\text{O}_x\text{-A-B}$

0.687 g of  $\text{Mn}(\text{NO}_3)_2 \cdot 4\text{H}_2\text{O}$  and 0.32 g of  $\text{Ca}(\text{NO}_3)_2 \cdot 4\text{H}_2\text{O}$  were dissolved in 2 ml distilled water. To this solution an aqueous solution of different amounts of cyanamide (0.8, 4.0 and 8.0 g, conc.  $1.0 \text{ g ml}^{-1}$ , "A" denotes the amount of cyanamide used) was added and the resulting mixture was stirred for 3 h under air ( $\text{pH} = 1$ ). The final solution was poured into a Petri dish and heated at  $100 \text{ }^\circ\text{C}$  for 30 h. The resulting brown-grey solid is scratched from the Petri dish and calcined under ambient conditions at different temperatures ( $T_{\text{calc}} = 300 \text{ }^\circ\text{C}$ ,  $400 \text{ }^\circ\text{C}$ ,  $550 \text{ }^\circ\text{C}$ ,  $700 \text{ }^\circ\text{C}$ ,  $1000 \text{ }^\circ\text{C}$ , "B" denotes the applied calcination temperature). A heating ramp with the rate of  $3 \text{ }^\circ\text{C min}^{-1}$  was used until the final temperature was reached and then the samples were heated for 4 h at this temperature.

Two reference materials were also prepared, one without cyanamide ( $A = 0$ ) and the other without calcium.

**Table 4.1: List of the CaMn oxides prepared at fixed amount of cyanamide but with different calcination temperatures.**

Sample's name ( $\text{CaMn}_2\text{O}_x\text{-A-B}$ )	Cyanamide (g)	$\text{Mn}(\text{NO}_3)_2 \cdot 4\text{H}_2\text{O}$ (g)	$\text{Ca}(\text{NO}_3)_2 \cdot 4\text{H}_2\text{O}$ (g)	Calcination temperature ( $^\circ\text{C}$ )
$\text{CaMn}_2\text{O}_x\text{-0.8-300}$	0.800	0.678	0.320	300
$\text{CaMn}_2\text{O}_x\text{-0.8-400}$	0.800	0.678	0.320	400
$\text{CaMn}_2\text{O}_x\text{-0.8-550}$	0.800	0.678	0.320	550
$\text{CaMn}_2\text{O}_x\text{-0.8-700}$	0.800	0.678	0.320	700
$\text{CaMn}_2\text{O}_x\text{-0.8-1000}$	0.800	0.678	0.320	1000
$\text{Mn}_2\text{O}_3\text{-0.8-550}$	0.800	0.678	0.00	550

## Experimental

**Table 4.2:** List of the CaMn oxides prepared at fixed calcination temperatures but with different amount of cyanamide.

Sample's name (CaMn <sub>2</sub> O <sub>x</sub> -A-B)	Cyanamide (g)	Mn(NO) <sub>3</sub> .4H <sub>2</sub> O (g)	Ca(NO <sub>3</sub> ) <sub>2</sub> .4H <sub>2</sub> O (g)	Calcination temperature (°C)
CaMn <sub>2</sub> O <sub>x</sub> -8-550	8.0	0.678	0.320	550
CaMn <sub>2</sub> O <sub>x</sub> -4-550	4.0	0.678	0.320	550
CaMn <sub>2</sub> O <sub>x</sub> -0.8-550	0.8	0.678	0.320	550
CaMn <sub>2</sub> O <sub>x</sub> -0-550	0.0	0.678	0.320	550

### 4.2 Synthesis of CaMn<sub>2</sub>O<sub>x</sub>-A-400

0.687 g of Mn(NO<sub>3</sub>)<sub>2</sub>.4H<sub>2</sub>O and 0.32 g of Ca(NO<sub>3</sub>)<sub>2</sub>.4H<sub>2</sub>O were dissolved in 2 ml distilled water. To this solution an aqueous solution of different amounts of cyanamide (0.4, 0.8, 4.0 and 8.0 g, "A" denotes the amount of cyanamide used) was added and the resulting mixture was stirred for 3 h under air (pH = 1). The final solution was poured into a Petri dish and heated at 100 °C for 30 h. The resulting brown-grey solid is scratched from the Petri dish and calcined under ambient condition. A heating ramp with the rate of 3 °C min<sup>-1</sup> was used until 400 °C was reached (3h) and then the samples were heated for 4 h at this temperature.

**Table 4.3:** List of CaMn oxides prepared at 400 °C but with different amount of cyanamide.

Sample's name (CaMn <sub>2</sub> O <sub>x</sub> -A-B)	Cyanamide (g)	Mn(NO) <sub>3</sub> .4H <sub>2</sub> O (g)	Ca(NO <sub>3</sub> ) <sub>2</sub> .4H <sub>2</sub> O (g)	Calcination temperature (°C)
CaMn <sub>2</sub> O <sub>x</sub> -0.4-400	0.4	0.678	0.320	400
CaMn <sub>2</sub> O <sub>x</sub> -0.8-400	0.8	0.678	0.320	400
CaMn <sub>2</sub> O <sub>x</sub> -4-400	4.0	0.678	0.320	400
CaMn <sub>2</sub> O <sub>x</sub> -8-400	8.0	0.678	0.320	400

## Experimental

---

### 4.3 Synthesis of M-A

Other metal oxides such as manganese, nickel, cobalt, copper, iron, chromium and tin oxides were prepared with the same protocol, with 0.8 g cyanamide, at fixed temperature (400 °C) but with different ramp time 3, 4, 6 and 8 hours.

**Table 4.4: List of the metal oxides prepared at fixed temperature but with different ramp rate.**

Sample name	Metal Precursor (g)	Ramp-time
Mn-2	Mn(NO <sub>3</sub> ) <sub>2</sub> .4H <sub>2</sub> O (0.990 )	2
Mn-3		3
Mn-4		4
Mn-6		6
Mn-8		8
Co-3	Co(NO <sub>3</sub> ) <sub>2</sub> .4H <sub>2</sub> O (1.1645)	2
Co-3		3
Co-4		4
Co-6		6
Co-8		8
Ni-2	Ni(OAc) <sub>3</sub> .4H <sub>2</sub> O (0.999)	2
Ni-3		3
Ni-4		4
Ni-6		6
Ni-8		8
Cu-2		2
Cu-3		3

## Experimental

---

Cu-4	CuSO <sub>4</sub> .5H <sub>2</sub> O (0.990)	4
Cu-6		6
Cu-8		8
Cr-2	CrBr <sub>3</sub> .6H <sub>2</sub> O (0.160)	2
Cr-3		3
Cr-4		4
Cr-6		6
Cr-8		8
Fe-2	FeCl <sub>2</sub> .4H <sub>2</sub> O (0.796)	2
Fe-3		3
Fe-4		4
Fe-6		6
Fe-8		8
Sn-2	SnCl <sub>3</sub> .2H <sub>2</sub> O (0.902)	2
Sn-3		3
Sn-4		4
Sn-6		6
Sn-8		8

### 4.4 Synthesis of porous nickel manganese oxides

These oxides were prepared with the same synthetic route as calcium manganese oxides, with fixed amount of cyanamide and calcination temperature. Three different oxides with varied ratio between nickel and manganese were synthesized.

## Experimental

**Table 4.5: Synthetic parameters which have been applied for nickel manganese oxides preparation.**

Name	Cyanamide (g)	Mn(NO <sub>3</sub> ) <sub>2</sub> .4H <sub>2</sub> O (g)	Ni(NO <sub>3</sub> ) <sub>2</sub> .4H <sub>2</sub> O (g)	Calcination temperature (°C)
NiMn <sub>2</sub> Ox	0.8	1.305	0.597	400
NiMn <sub>6</sub> Ox	0.8	1.305	0.199	400
NiMn <sub>8</sub> Ox	0.8	1.305	0.150	400

### 4.5 Supported Ni particles on SBA-15

#### 4.5.1 Syntheses of Ni precursor

Ni<sub>4</sub>(dpd-H)<sub>4</sub>(OAc)<sub>3</sub>(H<sub>2</sub>O)ClO<sub>4</sub>. Was prepared as described elsewhere<sup>[222]</sup> In a 100 ml Schlenck flask 2.488 g (10 mmol) of Ni(OAc)<sub>2</sub>.4H<sub>2</sub>O were dissolved in 50 ml of water and stirred under nitrogen atmosphere at 5 °C. After dissolution of the acetate, a solution of 0.911 g (5mmol) di-2-pyridilketone in 10 ml Acetonitrile was added dropwise over 15 min. The reaction mixture was cooled to room temperature and a solution of 1.40 g NaClO<sub>4</sub>.H<sub>2</sub>O (10mmol) in 1 ml H<sub>2</sub>O was added. The crystalline product (1.634 g) was collected after two days from the supernatant by filtration and dried on air.

#### 4.5.2 Preparation of SBA-15

SBA-15 was prepared according to the previously reported method.<sup>[223]</sup> Pluronic P123 triblock copolymer (M<sub>av</sub>=5800) was dissolved in a mixture of distilled water and a 2M hydrochloric acid solution before the addition of tetraethyl orthosilicate (TEOS). The above mixture was stirred for 24 h at 35 °C, and subsequently treated hydrothermally at 100 °C for 24 h. Finally the precipitate product was filtered, dried at 100 °C and calcined at 500 °C for 4 h.

#### 4.5.3 Synthesis of Ni<sub>4</sub>/SBA-15 and Ni/SBA-15 catalysts

Incipient wetness impregnation (IWI) method was used to introduce the Ni cubane molecule and Ni nitrate precursors into the SBA-15 pores. A-Ni<sub>4</sub>/SBA-15 and A-Ni/SBA-15 (A represents the nominal content of Ni) was prepared by impregnation with a Ni<sub>4</sub> molecule and Ni nitrate aqueous solutions with different concentrations. All samples were vacuum-dried at room temperature and calcined at 550 °C for 4 h.

### 4.6 Alumina overcoated Ni and NiO nanostructures

Ni oxide nanopowder (~ 50 nm particle size (TEM), 99.8% trace metals basis) was purchased from Sigma Aldrich and Ni nanoparticles (99.9%, average size: 20 nm but based on TEM images particles as big as 100 nm also were seen) from Skysprig nanomaterial Inc.

ALD was performed using a viscous flow reactor system similar to one previously described<sup>[263]</sup> and a stainless steel fixed-bed powder sample holder.<sup>[264]</sup> Ultrahigh purity nitrogen (99.999%) was used as the carrier gas with a mass flow rate of 360 sccm. The system pressure was between 1 and 2 Torr. In traditional ALD, two precursors, A and B, are alternately dosed and purged through the reactor. The purge gas used was ultrahigh purity nitrogen. The ALD time sequence for one AB cycle can be expressed as  $t_1-t_2-t_3-t_4$  where  $t_1$  is dose time for A;  $t_2$  is purge time for A;  $t_3$  is dose time for B; and  $t_4$  is purge time for B. Here ALD  $\text{Al}_2\text{O}_3$  was performed using alternating exposures to trimethyl aluminum (TMA, Aldrich, 99%) and deionized water with the timing sequence 300-300-300-300 s. Due to the porous or curved nature of the substrates, the applied dose and purge times were drastically longer than when depositing on flat substrates.<sup>[264]</sup> The over-coated samples were prepared using 5, 10, 15, and 20 cycles of  $\text{Al}_2\text{O}_3$  ALD at 50 °C to generate the protective layers.

### 4.7 Catalytic tests

#### 4.7.1 Chemical water oxidation test with Clark electrode

For a typical catalytic experiment, oxides were suspended in water in a Schlenk tube. Then these solutions were made anaerobic by nitrogen purging ( $[\text{O}_2] < 1 \mu\text{mol/l}$ ) and the oxygen level was monitored by a Clark electrode. After an equilibration time of 2 min, an anaerobic solution of Ce(IV) was injected into the tube using a nitrogen-purged syringe. The dissolved oxygen produced during the reaction was monitored by a Clark electrode. The initial oxygen evolution rates as shown in Table 2.1. and 2.2. were determined by a linear fit of the Clark cell data of the first three minutes and divided by the amount of the overall manganese content in the oxide suspended in the 2 ml reaction solution. In pursuing these experiments, it was been considered that the Clark electrode can detect dissolved oxygen reliably only below the  $\text{O}_2$ -saturation point of water (258  $\mu\text{mol/l}$ , T=25 °C).

**Table 4.6: Amount of dissolved oxides (mg/ml) in solution (0.5M Ce<sup>4+</sup>).**

Sample	Oxide amount (mg/ml)
CaMn <sub>2</sub> O <sub>x</sub> -0.8-300	0.5
CaMn <sub>2</sub> O <sub>x</sub> -0.8-400	0.05
CaMn <sub>2</sub> O <sub>x</sub> -0.8-550	0.5
CaMn <sub>2</sub> O <sub>x</sub> -0.8-700	0.5
CaMn <sub>2</sub> O <sub>x</sub> -0.8-1000	0.5
CaMn <sub>2</sub> O <sub>x</sub> -8-550	0.5
CaMn <sub>2</sub> O <sub>x</sub> -4-550	0.5
CaMn <sub>2</sub> O <sub>x</sub> -0-550	0.5
Mn <sub>2</sub> O <sub>3</sub> -0.8-550	0.45

#### 4.7.2 Chemical water oxidation test with Gas Chromatography

An Agilent 7890A gas chromatograph was used to determine the oxygen content in the headspace of the reactor. The GC was equipped with a carboxen-1000 column and a thermal conductivity detector (TCD). The carrier gas was argon (30 mL min<sup>-1</sup>). Calibration was done with oxygen gas mixture of defined concentrations (1, 10 vol%).

The long-term experiments were carried out as follows: Millipore water was sonicated under reduced pressure for 1 h. Afterwards the water solution was flushed with argon for 1 h to remove all oxygen. The catalyst (100 mg) and the magnetic stir bar were placed into the reaction chamber and the reactor was closed. Subsequent oxygen was removed by applying vacuum and flushing the reactor with argon. This procedure was repeated 3 times. The reaction mixture, consisting of Ce<sup>4+</sup> in water (0.5 M), with a total volume of 38 mL, was prepared in an oxygen evacuated flask. Then the reaction solution was added to the reaction chamber under reverse argon flow using a dosing valve. After closing the dosing valve, thermostat, magnetic stirrer, and the online measurement software were started. For the second injection the reactor has been opened under Argon, flushed with this gas, and then closed after the injection. The data after oxidant addition was added to the first graph assuming that flushing the reactor with Ar removed all oxygen produced in the first step<sup>[265]</sup>

## Experimental

Recycling experiments have been done for the most active catalyst,  $\text{CaMn}_2\text{O}_x$ -0.8-400. After each run the catalyst was recovered by filtration, washed several times with water, dried and then used again. The TOF has been calculated based on the oxygen amount (in mmol) produced in the first 30 min of the reaction and divided by the amount of manganese of the catalyst (in mol).

### 4.7.3 Catalytic test for DRM reaction

Catalyst testing was carried out in a fixed-bed quartz tube reactor (internal diameter 5 mm). The catalyst mass was diluted in quartz sand or glass balls with a total volume of 1.25 ml. The reactor was heated using an external furnace (HTM Reetz) controlled by a temperature probe within the catalyst bed. Each catalyst was reduced in-situ in pure  $\text{H}_2$  for 1 h at  $500^\circ\text{C}$  before testing. Typical reaction conditions were: 30 ml/ min reaction gas with composition  $\text{CH}_4:\text{CO}_2:\text{He} = 1:1:8$  at atmospheric pressure. Outlet gases were analyzed (typically every 10-30 minutes) using an Agilent 7890A gas chromatograph equipped with thermal conductivity and flame ionization detectors.

#### 4.7.3.1 Thermodynamic equilibrium of the DRM reaction under the standard conditions

Equilibrium calculations were carried out using the CHEMKIN Equilibrium Reactor model at constant pressure and temperature, for gas mixtures  $\text{CH}_4:\text{CO}_2:\text{He} = 1:1:8$  and possible products  $\text{CH}_4$ ,  $\text{CO}_2$ ,  $\text{H}_2$ ,  $\text{H}_2\text{O}$ ,  $\text{CO}$  and  $\text{He}$ , by minimizing the Gibbs free energies of all species (independent of reaction details).

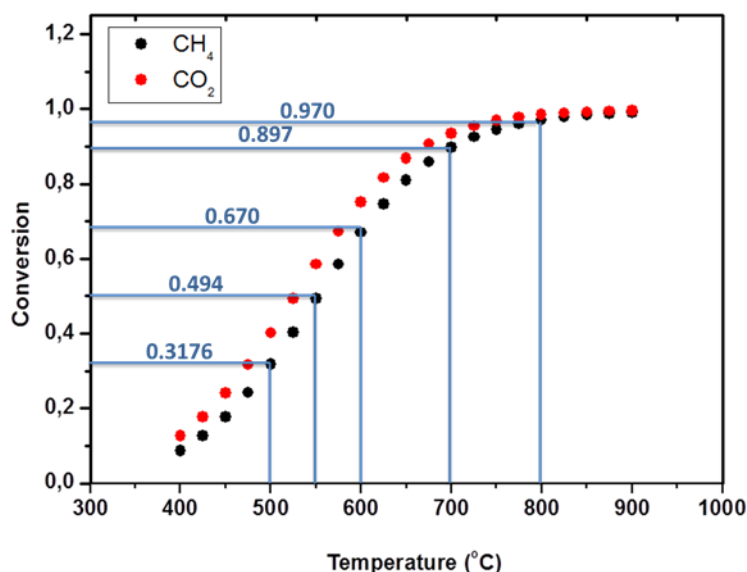


Fig. 4.1: Thermodynamically limited conversion of the DRM reaction with the reaction temperature range of 400-900 °C.

### 5. Characterization methods

In this thesis, various methods were used to characterize the prepared materials regarding their structure, morphology and composition as well as their crystallinity. Therefore a brief introduction into the different characterization techniques is presented in this chapter. Instrumental details and experimental parameters are also mentioned.

#### 5.1 Electron microscopy (EM)

Electron microscopy is a class of imaging technique that uses a focused electron beam to collect information about the structure and morphology of a sample as well as its composition and crystallinity. Resolution which is the ability to recognize two closely placed objects as two distinct structures is given by the Ernst Abbe formula:

$$d = \frac{0.612 * \lambda}{n \sin \alpha} \quad 5.1$$

With  $\lambda$  the wavelength of the radiation,  $n$  the refraction index of the medium and  $\alpha$ , the half aperture angle in radians. For light microscopes ( $\lambda = 400\text{-}700$  nm), resolution range is  $\sim 300\text{-}700$  nm. By using electrons instead of visible light as imaging radiation a much better resolution can be obtained. In 1924 De Broglie described moving particles as wave-like (wave-particle dualism). Therefore their wavelength is linked to their mass  $m$ , their velocity  $v$  and the Planck's constant  $h$  by the De Broglie equation:

$$\lambda = \frac{h}{p} = \frac{h}{mv} \quad 5.2$$

In an electron microscope the energy of the electrons and hence their momentum depends on the accelerating voltage. This energy can be determined by equating the potential energy and the kinetic energy by equation 5.3.

$$E = eV = \frac{1}{2} mv^2 \quad 5.3$$

With  $e$  as the charge of one electron,  $V$  the acceleration voltage and  $m$  the mass of one electron,  $\lambda$  can be calculated combined with De Broglie equation:

$$\lambda = \frac{h}{\sqrt{2meV}} \approx \sqrt{\frac{1.5}{V}} \text{ (nm)} \quad 5.4$$

Relativistic corrections are required due to fast movement of an electron which causes its speed to approach light velocity:

$$\lambda = \frac{h}{2a\sqrt{2meV(1 + \frac{eV}{2mc^2})}} \quad 5.5$$

In electron microscope techniques (regardless the type), electrons are generated and accelerated toward the sample. Magnetic lenses are used to focus the electron beam onto the sample. Each lens has its own set of aberration and distortions that determine the practical final obtained resolution of the image which is resulted from the interaction between beam and the object.

Two major types of EM are the scanning electron microscope (SEM) and the transmission electron microscope (TEM). Both were used in this work to investigate the morphology and structure of the synthesized materials.

### 5.1.1 Scanning electron microscopy (SEM)

Scanning electron microscopy (SEM) is based on the scattering of electrons from the surface of the sample. The schematic presentation of an SEM set-up is presented in Figure 5.1.

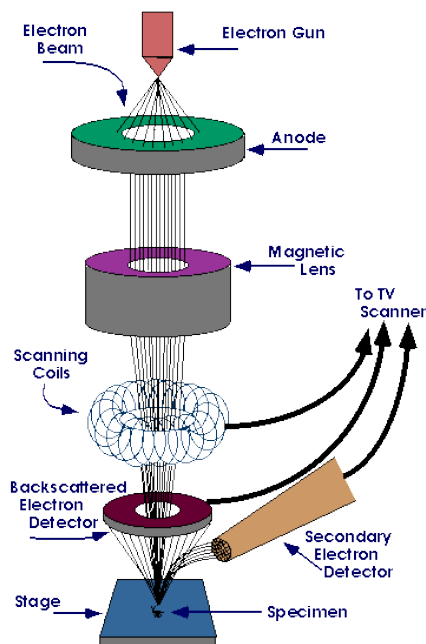


**Fig. 5.1: Schematic description of the optics of an SEM set-up.** <sup>[269]</sup>

A beam of electrons is produced at the top of the microscope by an electron gun. The electron beam follows a vertical path through the microscope, which is held within a vacuum. The beam travels through electromagnetic fields and lenses, which focus the beam down toward the sample. Once the beam hits the sample the electrons interact with its surface and if their energy is higher than the ionization potential of the elements on the surface, secondary electrons are emitted (SE). The surface of the sample (typically 1-5 nm in size), is scanned in a raster fashion, by electromagnetic deflection coils.

These electrons are relatively slow with low energy (< 50 eV) and are attracted towards the detector, through a grid held at a low positive potential. The electron detector counts the number of secondary electrons arriving per unit time and transfers them into an electric signal. The number of electrons collected from each point of the sample is used to build up the final image. The surface geometry of the sample determines the release of SEM. The edges or convex surfaces within the sample appear brighter, because of the increasing number of counted electrons, while concave surfaces appear darker. Because of this mechanism the obtained images appears spatial and rich in contrast with structural and topographic details of the sample's surface.

### **5.1.2 Transmission electron microscopy (TEM)**

A higher resolution can be obtained with the transmission electron microscope compared to the scanning electron microscope. Here a very thin probe is required since the electron beam passes through the sample. The electron source (electron gun) is a heated cathode producing a stream of monochromatic electrons. Electrons are produced either by thermal emission or by a field emission gun and accelerated towards an anode. Then the produced electrons are focused into a coherent beam by first and second condenser lenses. When the beam reaches the sample, the electrons either transmit or interact with the material in varied way such as absorption, diffraction and elastic or inelastic scattering.

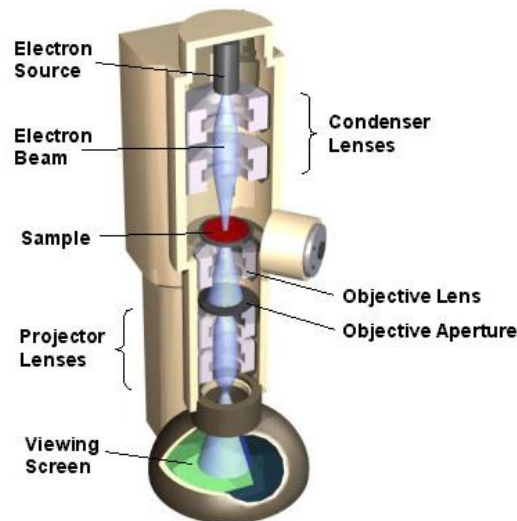


**Fig. 5.2: Schematic description of the optics of an SEM set-up.**<sup>[270]</sup>

The instrument can be operated in two basic modes: image mode or diffraction mode. In the image mode which is the most common one, the scattered electrons are blocked by an aperture under the sample and the transmitted portion of the beam passes the further lenses. Finally, it is focused by the objective lens into an image. The contrast in the final image is related to the variation of the transmitted electron beam intensity. Since the scattering processes is a consequence of interaction between electrons and the nuclei of the samples, heavy elements (high  $Z$ ) lead to higher scattering, which shows that fewer electrons are passing through the sample, therefore the sample regions containing heavy elements appear dark. On the other hand regions containing lighter elements, such as organic compound, causes lower scattering and appear much brighter. Moreover the thickness of the sample also can weaken the electron beam density, the thicker the sample is, the fewer electrons are transmitted. The contrast generally is proportional to  $Z^2$ . In the diffraction mode, selected area diffraction pattern (SAED) of the “illuminated” part of the sample is obtained by the elastic scattered electrons. The observed diffraction pattern is a representation of the reciprocal space. In a SAED pattern obtained from a single crystal, reflection spots appear on well-defined sites which are characteristics for the crystal structure and  $d$  value (lattice parameter). In a polycrystalline materials, the diffraction patterns of all the involving single crystals are superimposed, therefore, spots are located on the ring due to the same  $d$  values. As a consequence, the crystalline structure on a nanometer scale can be investigated via the diffraction mode.

### 5.1.3 Energy dispersive X-ray spectroscopy

(EDS or EDX) is a technique widely used to investigate the composition of a sample. This technique is based on the unique electronic structure of each element of the periodic table which results in a unique response to electromagnetic waves. X-rays are created when the electrons of the beam interact with the elements within the sample; Analysis of the emitted X-rays allows the determination of the elemental composition of the irradiated sample.

When an atom of the sample is hit by the electron beam, an electron from an inner shell gets excited, then ejected and leads in the formation of an electron hole within the atom's electronic structure. This causes the relaxation of an electron from an outer, higher-energy shell toward the depopulated shell, releasing the excess energy in the form of an X-ray. Highly specific spectral for each individual element are created by the release of X-rays and allows thus the elemental analysis of the sample.

### 5.2 X-Ray Diffraction

X-ray diffraction is a technique based on the interaction of short wavelength (around  $10^{-10}$  meter) electromagnetic radiation with matter. Three different types of scattering are emitted when matter is irradiated by X-rays: elastic scattering, inelastic scattering and fluorescence radiation. For elastic scattering, the outgoing X-rays have the same energy, so the same wavelength, as the incoming X- but with deviated direction. In contrast, inelastic scattering occurs when energy is transferred from to the crystal, e.g. by exciting an inner-shell electron to a higher energy level which makes the outgoing beam longer and less energetic. Fluorescence radiation can be produced by the relaxation of a high energy electron into a lower energy state which happens when the energy of the X-ray is higher than the ionization potential of the bombarded atoms. Only the elastic scattering is required for structural studies.

The X-rays are produced in a vacuum X-ray tube containing two electrodes: copper anode and tungsten cathode. The generation of X-rays is very similar to the EDX, meaning, a tungsten filament is heated up and electrons are emitted then attracted towards the copper anode. The copper atom loses an electron, the vacancy is filled with an electron from a higher energy level and X-rays are emitted. Usually, the X-ray collected is Cu K $\alpha$  which has a wavelength of 0.154 nm.

There are two types of XRD: reflective and transmission. For reflective XRD, the X-ray tube will direct the X-rays to the sample; the crystal structure will then divert the X-rays at an angle towards the detector. The detector, which rotates to different angles will then record the number of counts at a certain angle and relay this to the computer. Finally a spectrum is calculated, with intensity against angle ( $2\theta$ ). For transmission XRD, the X-rays, pass through the sample and then into the detector.

A crystalline sample will randomly scatter the X-rays after being hit by the beam. The secondary scattered waves interfere constructively if the spacing between scattering center is regular. This process is called diffraction which can be described by the Bragg law. The distance between a set of planes in a crystal ( $d$ ) and the angle ( $\theta$ ), can be related by the Bragg law.

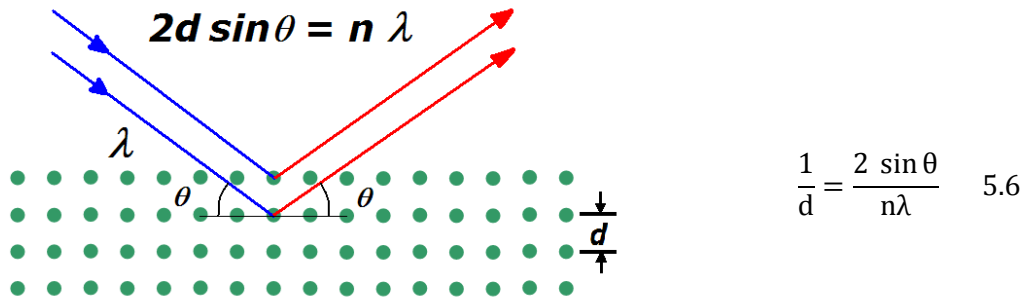


Fig. 5.3: Schematic diagram of the Bragg law.

Where  $n$  is the diffraction order and  $\lambda$  is the wavelength of the incident wave. Crystal size can also be calculated from the XRD pattern by using the Debye-Scherrer formula (5.7). The width of the peak increases by decreasing the size of the particle.

$$D_{hkl} = \frac{K\lambda}{\beta \cos \theta} \quad 5.7$$

$K$  is the shape factor,  $\lambda$ , the wavelength of the X-ray,  $\beta$ , the full width at half maximum and  $\theta$  is the angle of point of maximum diffraction. The shape factor tends to be in the region of 0.8-1.39, although will typically be 0.9. The wavelength for the copper X-rays will typically be 0.154 nm.

### 5.3 X-ray Absorption Spectroscopy XAS

When X-ray beam is hitting an atom, it can either be transmitted or absorbed. X-ray photon with the energy higher than the binding energy of a deep core-level electron is absorbed and an electron will be ejected from the atom. The kinetic energy of the ejected electron is equal to the energy of the incident X-ray minus the binding energy of the electron. The x-ray beam of intensity  $I_0$  passing through a sample of thickness  $x$  will get a reduced intensity  $I$  according to the Beer's Law:

$$I = I_0 e^{-\mu x} \quad \text{or} \quad \mu(E)x = \log\left(\frac{I_0}{I}\right) \quad 5.8$$

where  $I_0$  is the intensity of the incident X-rays,  $I$  is the intensity of X-rays transmitted through the sample,  $x$  is the sample thickness, and  $\mu$  ( $\text{cm}^{-1}$ ) is the absorption coefficient which is a smooth function of energy depends on the types of atoms and the density of the material:

$$\mu \approx \frac{\rho Z^4}{AE^3} \quad 5.9$$

Where  $\rho$  (g/cm<sup>3</sup>) is the density,  $Z$  the atomic number,  $A$  the atomic mass and  $E$  the energy of the X-ray. The absorption coefficient can also be written as a function of the X-ray cross section,  $\sigma$  (cm<sup>2</sup>/g), as

$$\mu = \sigma \cdot \rho \quad 5.10$$

The absorption increases drastically at certain energies, and gives rise to an absorption edge. Such a rise occurs when the energy of the incident photons is just sufficient to cause excitation of a core electron of the absorbing atom to a continuum state, i.e. to produce a photoelectron.

Thus, the energies of the absorbed radiation at these edges are related to the binding energies of electrons in the K, L, M, etc., shells of the absorbing elements. The absorption edges are named in the order of increasing energy, K, L<sub>I</sub>, L<sub>II</sub>, L<sub>III</sub>, ..., corresponding to the excitation of an electron from the 1s (<sup>2</sup>S<sub>1/2</sub>), 2s (<sup>2</sup>S<sub>1/2</sub>), 2p (<sup>2</sup>P<sub>1/2</sub>), 2p (<sup>2</sup>P<sub>3/2</sub>), ... orbitals (states), respectively. In a single-atomic system, when core level electrons are excited with X-ray energies at the binding energy ( $E_0$ ), there is a sharp rise in the absorption probability, or  $\mu$ . This rise is followed by a monotonic decrease until the next core level excitation. In case of multi-atomic compounds, when the photoelectron leaves the absorbing atom, its wave is backscattered by the neighboring atoms which result in subsequent constructive and destructive interference of the outgoing and scattered wave functions and hence the appearance of the fine structures. .

An x-ray absorption spectrum is generally divided into 2 sections:

- 1) X-ray absorption near edge structure (XANES); the near-edge region which extends from ~20 eV below to 50 eV above the absorption edge
- 2) Extended X-ray absorption fine structure (EXAFS), the extended region which extends from ~50 eV to 1000 eV above the absorption edge.

These sections are based on the difference in scattering behavior of the electron as a function of its kinetic energy. The electron transitions from the core level to the higher unfilled or half-filled orbitals (e.g,  $s \rightarrow p$ , or  $p \rightarrow d$ ) usually result in the minor features in the near-edge region.

In General, XAS is a very sensitive probe of the local chemical environment (oxidation state, unoccupied density of states, and local symmetry) of the absorbing atom. The position of the absorption edge is dependent on the atom type which is analyzed due to the presence of individual core level binding energy for each element. Furthermore, the shape of the XANES spectra is strongly

influenced by the available electronic states which are determined by the atomic species as well as the bonding conditions. Additionally, the XANES regime is influenced by multiple backscattering of the photoelectron by surrounding atoms. Thus, XANES spectra are providing information on the mean oxidation state and the coordination geometry of an examined element.

The EXAFS regime of a spectrum is addressing the absorption of X-rays of higher energies, well above the absorption edge ( $E_0$ ). The created photoelectron via the promotion of a core level electron by X-ray absorption can be scattered from a surrounding atom, back to the absorbing atom (Figure 7.6, right). The backscattering effect is strongly influenced by the type and the distance of the surrounding atoms therefore EXAFS regime is providing information on the distance and the type of neighboring atoms.

Fortunately we had the opportunity to collaborate with the group of Prof. Holger Dau from Freie University Berlin, in order to carry out XAS experiments. In this collaboration, XANES and EXAFS spectra of calcium manganese oxides were recorded at the Mn and CaK-edge.

### 5.4 Nitrogen sorption

A powerful technique that is commonly used to characterize the physical parameters of porous materials such as surface area, their pore volume and the size of the pores present is gas sorption, mainly nitrogen sorption.

In this method, the sample to be analyzed is heated at least at 120 °C under vacuum prior to physisorption in order to remove any other gas molecules adsorbed on the surface of the sample. Then the adsorbent is cooled to a constant temperature, by immersing the measuring cell in a liquid nitrogen bath ( $T_{\text{liquid N}_2} = 77 \text{ K}$ ). A known quantity of gas, the adsorbate, is then introduced into the measuring cell. The amount of adsorbed gas on the surface of the adsorbent can be calculated from the difference between the gas pressure inside the tube, before and after dosing. The plot of the adsorbed gas quantity as a function of the relative gas pressure  $p/p^0$  gives an adsorption isotherm. When the entire volume is filled, the following stepwise decrease of the pressure yield the desorption isotherm. Such an isotherm is classified in to six shapes by IUPAC. Type I isotherms are characteristic for pure microporous (Pore diameter (PD) less than 2 nm) materials with low external surface area. The micropores become filled at relatively low partial pressures ( $p/p_0 < 0.1$ ). Type II and type III isotherms describe the adsorption on macroporous (PD bigger than 50 nm) or non-porous adsorbents with strong and weak adsorbate-adsorbent interactions, respectively. Type IV isotherms are characteristic for mesoporous materials (PD between 2 and 50 nm). Their distinctive feature is the presence of a hysteresis loop, due to the deviation between capillary condensation of the gas in

the mesopores and its evaporation. Indeed the gas-liquid transition process is not reversible, leading to hysteresis between adsorption and desorption part of the isotherm. Finally type VI isotherms is a type of isotherm obtained for non-porous materials, represent the stepwise adsorption of several layers on a surface.

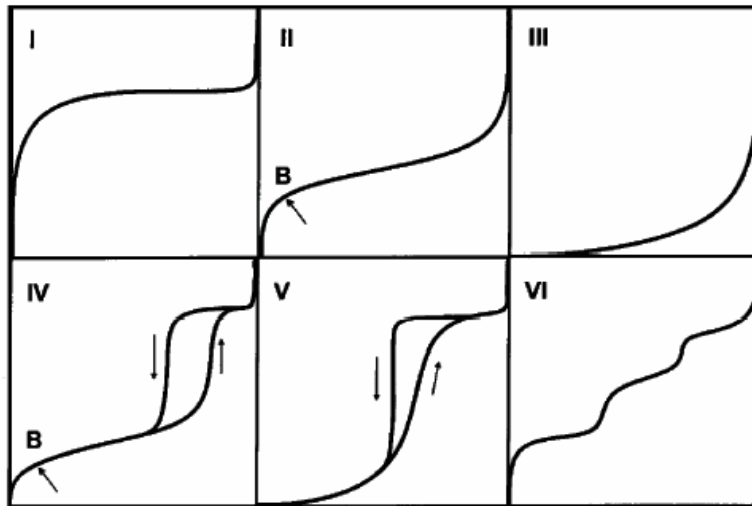


**Fig. 5.4: Classification of the isotherm types by IUPAC. The point B, highlighted with an arrow in represents the stage where the monolayer is completed and the multilayer formation begins.**

### 5.4.1 Determination of the surface area

Various mathematical models were developed to calculate key parameters of porous solids such as surface area and pore size distribution from the physisorption isotherms. One of the main methods to evaluate the specific surface area is the classical model, so called BET model, developed by Brunauer, Emmet and Teller in 1938.

The BET theory is based on the kinetics of gas adsorption, originally described by Langmuir. He assumed that :

1. Gaseous molecules behave ideally.
2. The surface of the solid consists of an arrangement of equivalent adsorption sites.
3. The system is in thermodynamic equilibrium, with equal adsorption and desorption rates of the gas molecules on the surface.
4. Only one monolayer is formed.

The Langmuir equation is obtained base on the above assumptions:

$$\frac{p/p_0}{n(1 - p/p_0)} = \frac{C - 1}{n_m C} (p/p_0) + \frac{1}{n_m C} \quad \text{with } C = e^{(H_1 - H_L)/RT} \quad 5.11$$

Where  $n$  is the total amount of adsorbed gas,  $n_m$  the amount of adsorbate molecule in the monolayer and  $p/p_0$  the relative pressure.  $C$  is associated to the  $H_1$  and  $H_L$ , the adsorption and condensation enthalpies respectively. By plotting the left side of the equation against  $p/p_0$  (usually in the range between  $p/p_0 = 0.1-0.3$ ) a straight line is observed from the slope of the plot and the axis intercept  $n_m$  and  $C$  can be derived. The specific surface area  $S_{\text{BET}}$  can be calculated from  $n_m$  and  $N_A$  (Avogadro number) by assuming an average area  $\sigma$  that each adsorbed molecule occupies in a monolayer on the surface area of the solid through the simple equation:

$$S = n_m \sigma N_A \quad 5.12$$

### 5.5 Instrumental details

**BET:** Nitrogen sorption isotherms were measured at liquid-nitrogen temperature (-196 °C) with an Autosorb-1. The samples were degassed at 150 °C overnight before the measurement. The BET surface area was calculated by multiple-point (five-point) measurement.

**ICP-MS:** The mass content of metals was measured by ICP-MS Element 2 (Varian Inc., USA), with sample gas flow 0.863 L/min and plasma power 1350 W.

**TEM:** TEM images were obtained on a Philips CM200 instrument, operated at 120 keV, using amorphous carbon-coated copper grids. The specimens were dispersed in ethanol with ultrasonication and loaded onto a copper grid.

**TPO:** Temperature programmed oxidation was carried out under 8 ml per min flow of 20% O<sub>2</sub> in He. Oxidation temperature was between room temperature to 800 °C with a heating ramp of 10 °C per minute. Outlet gas analyzed using a quadrupole mass spectrometer (Inprocess Instruments GAM 200)

**XRD:** XRD was performed using a Bruker D8 Advance X-ray diffractometer with Cu K $\alpha$  1 = 1.5418 Å radiation between 2° and 90° ( $2\theta$ ).

**X-ray absorption spectroscopy:** XAS of CaMn oxides were performed at the Mn and Ca K-edges at the BESSY synchrotron (Helmholtz-Zentrum Berlin, Germany). The measurements were acquired in transmission mode at the KMC-1 bending-magnet beamline at 20 K in a cryostat (Oxford-Danfysik) with a liquid helium flow system.

6. Appendix

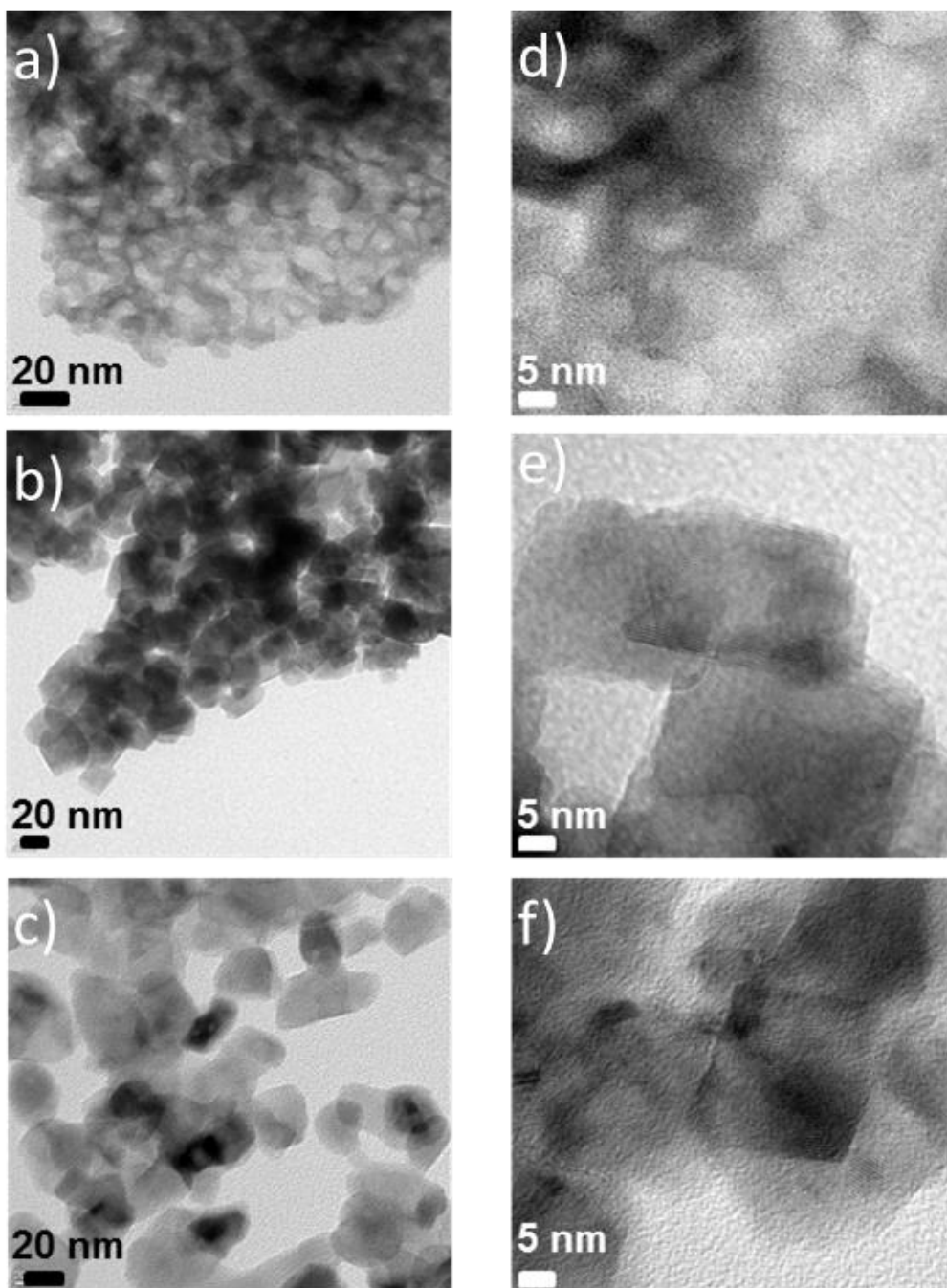
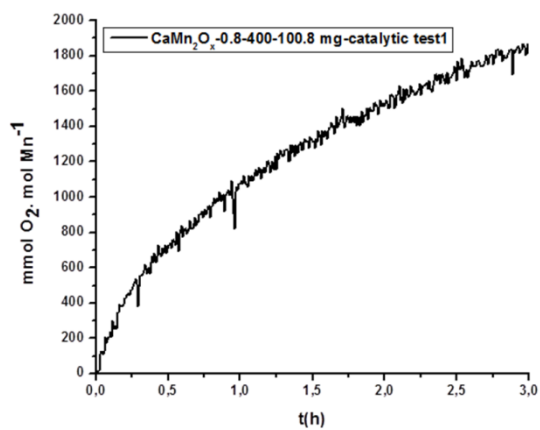
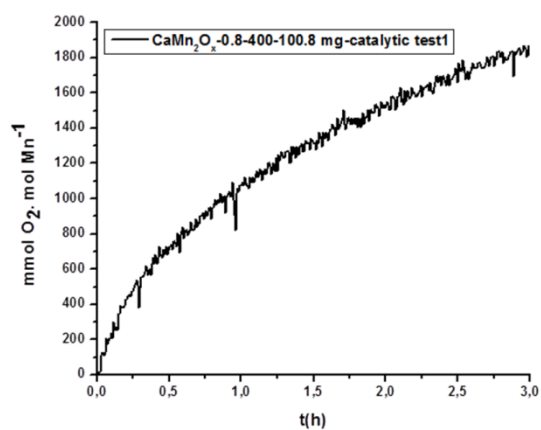


Fig 6.1: TEM images of a)  $\text{CaMn}_2\text{O}_x$ -0.8-550, b)  $\text{CaMn}_2\text{O}_x$ -4-550, c)  $\text{CaMn}_2\text{O}_x$ -8-550 and (HR)TEM images of d)  $\text{CaMn}_2\text{O}_x$ -0.8-550, e)  $\text{CaMn}_2\text{O}_x$ -4-550, f)  $\text{CaMn}_2\text{O}_x$ -8-550.

a)



b)



c)

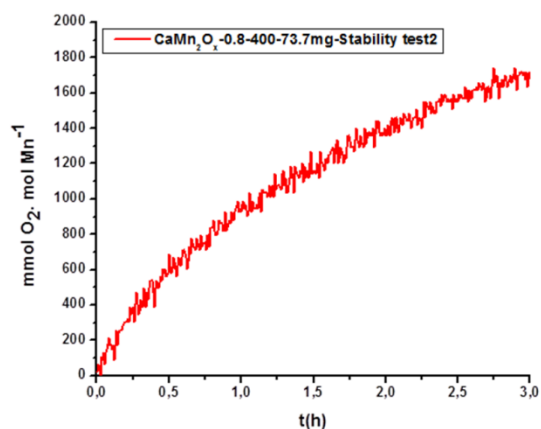


Fig 6.2: Recycling experiments using  $\text{CaMn}_2\text{O}_x\text{-0.8-400}$ ; a) first run, b) second and c) third run. After each run the catalyst was recovered by filtration, washed several times with water, dried and then used again.

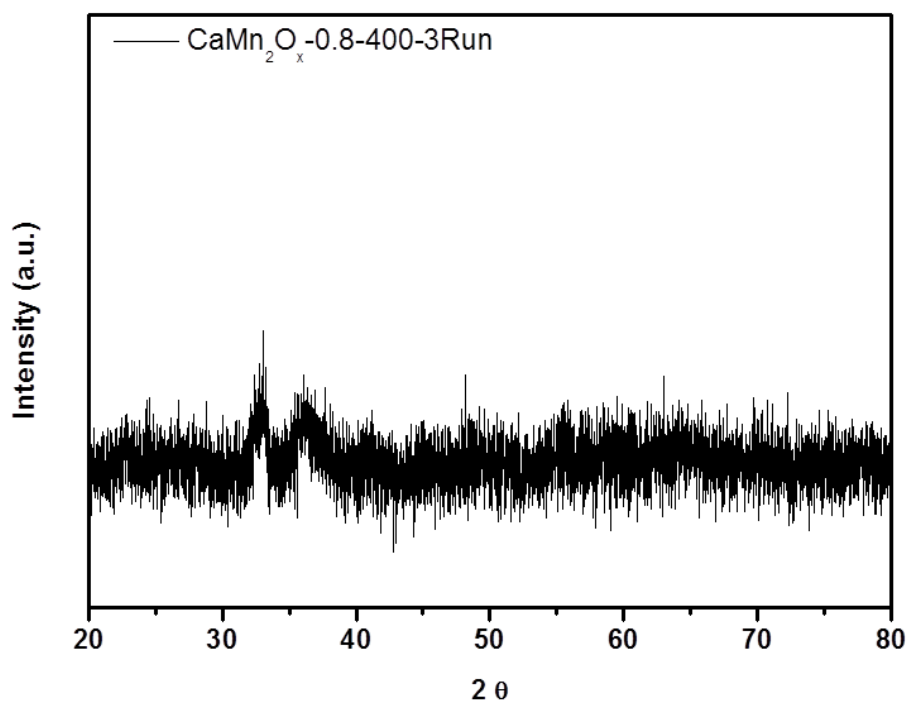


Fig 6.3: XRD pattern of the CaMn<sub>2</sub>O<sub>x</sub>-0.8-400 after third run of catalytic test.

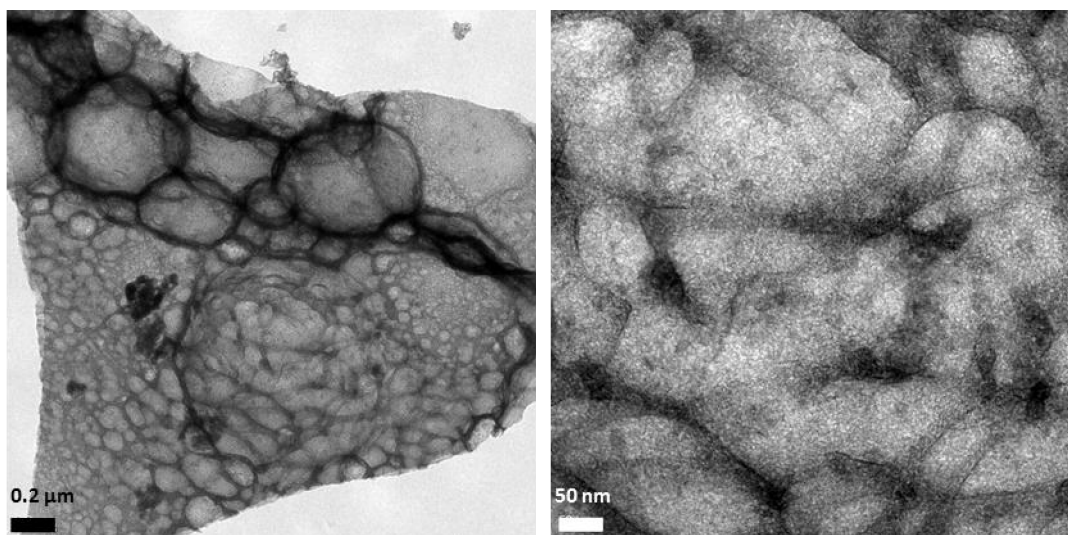


Fig 6.4: TEM image of CaMn<sub>3</sub>O<sub>x</sub>-0.8-400 after third run of catalytic test.

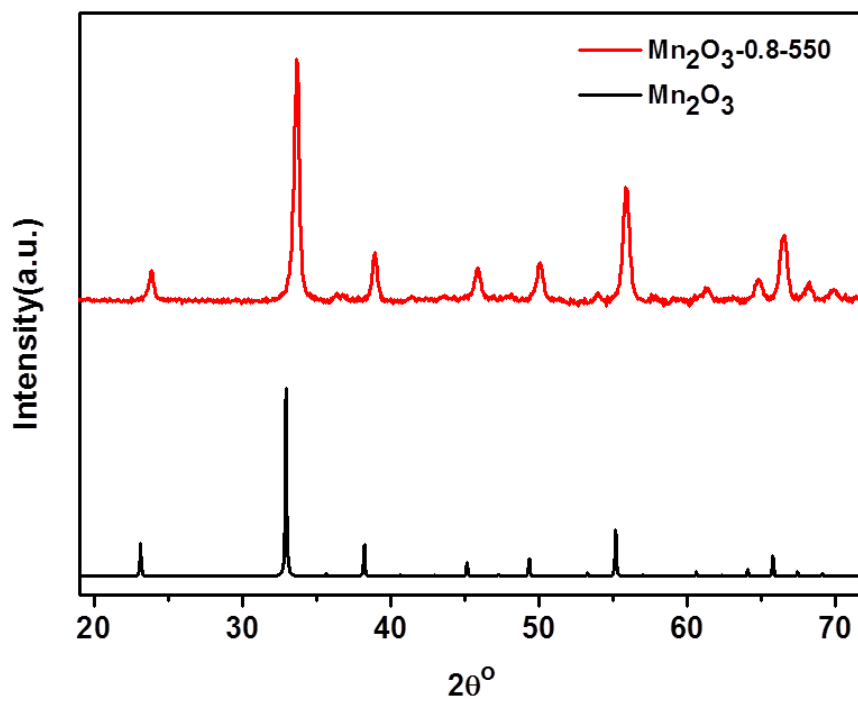


Fig 6.5: XRD pattern of  $\text{Mn}_2\text{O}_3\text{-0.8-550}$  and the reflection pattern of  $\text{Mn}_2\text{O}_3$  are shown for comparison.

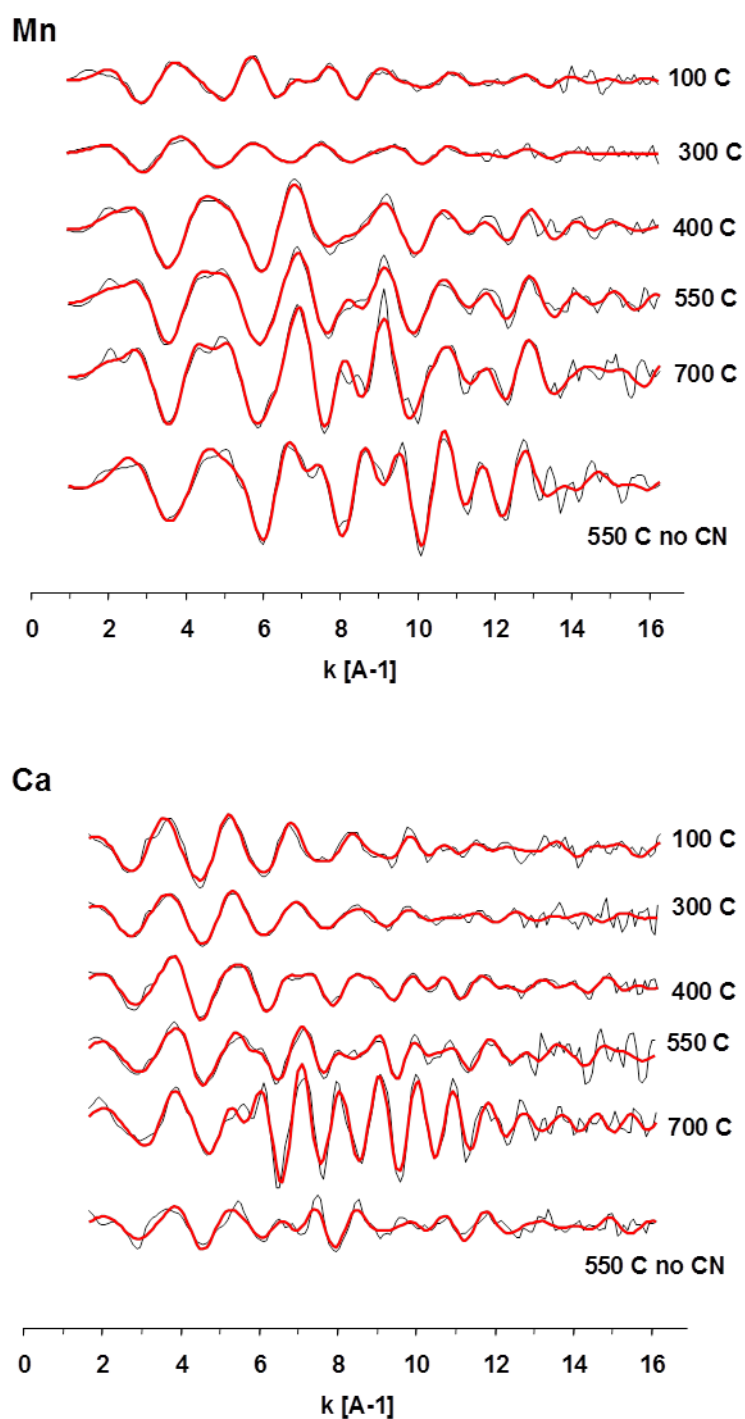


Fig 6.6:  $k^3$ -weighted EXAFS spectra measured at the Mn K-edge (top) and the Ca K-edge (bottom) from the CaMn material before annealing (labeled '100 oC') and after annealing for 4 h at the indicated temperature. Black: experimental curves, red, simulations. The simulation parameters are shown in table 6.4.

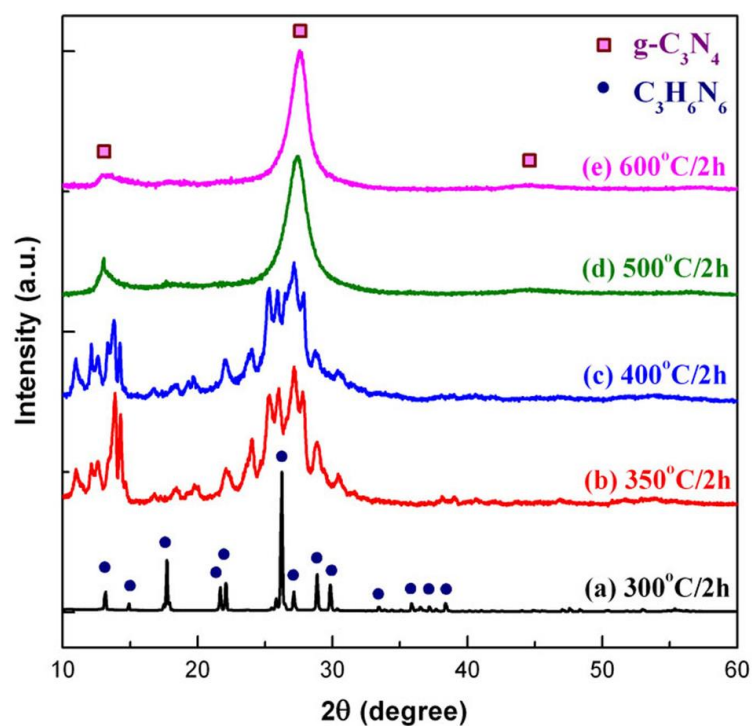


Fig 6.7: XRD patterns of the products synthesized via the thermal condensation of melamine at different temperatures for 2 h.<sup>[167]</sup>

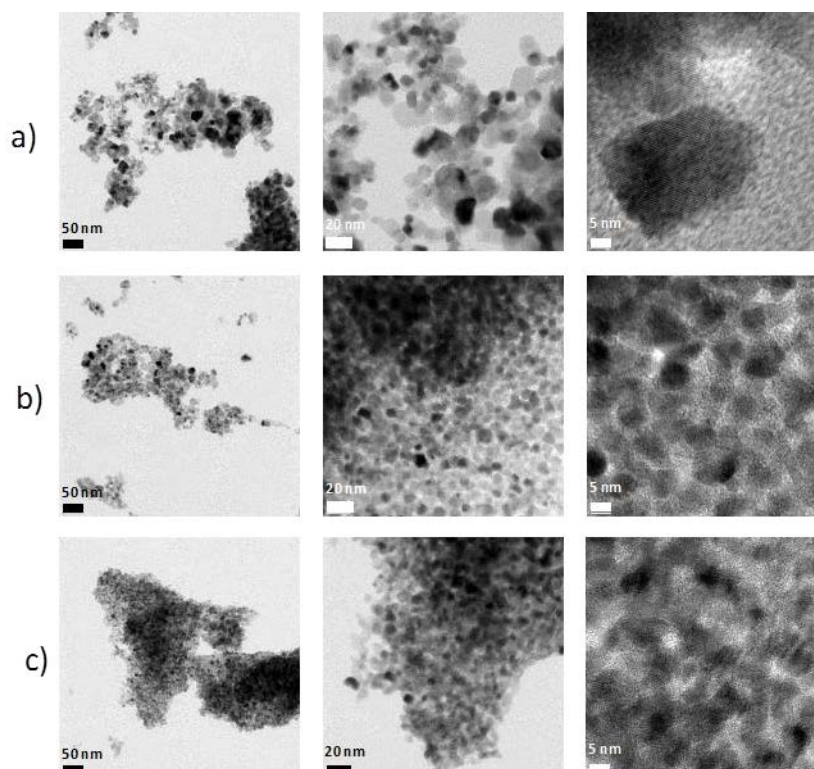


Fig 6.8: a) TEM images of Ni-4, b) Ni-6 and c) Ni-8.

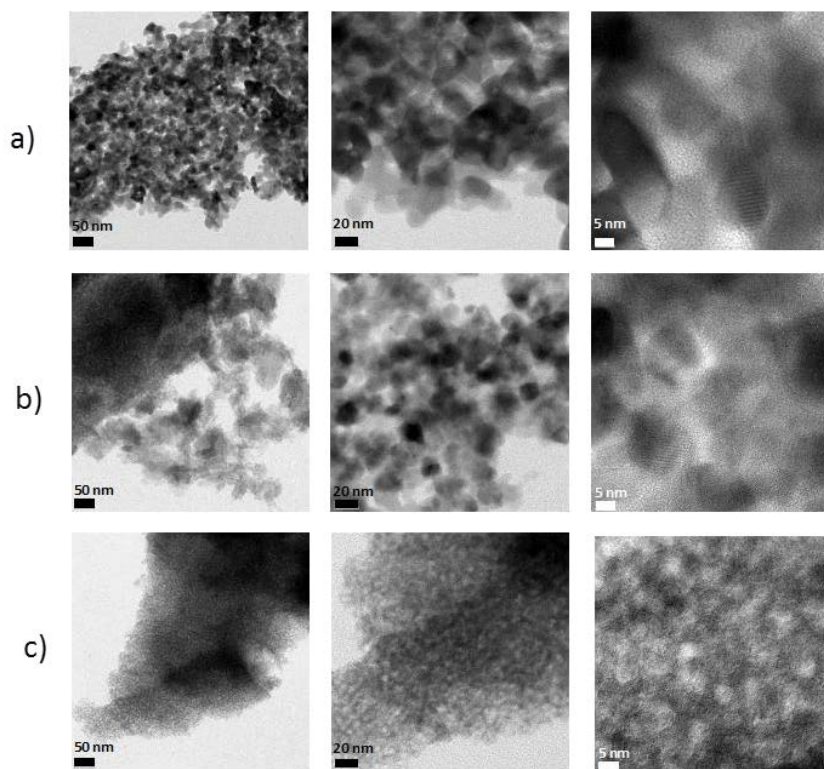


Fig 6.9: a) TEM images of a) Mn-4, b) Mn-6 and c) Mn-8.

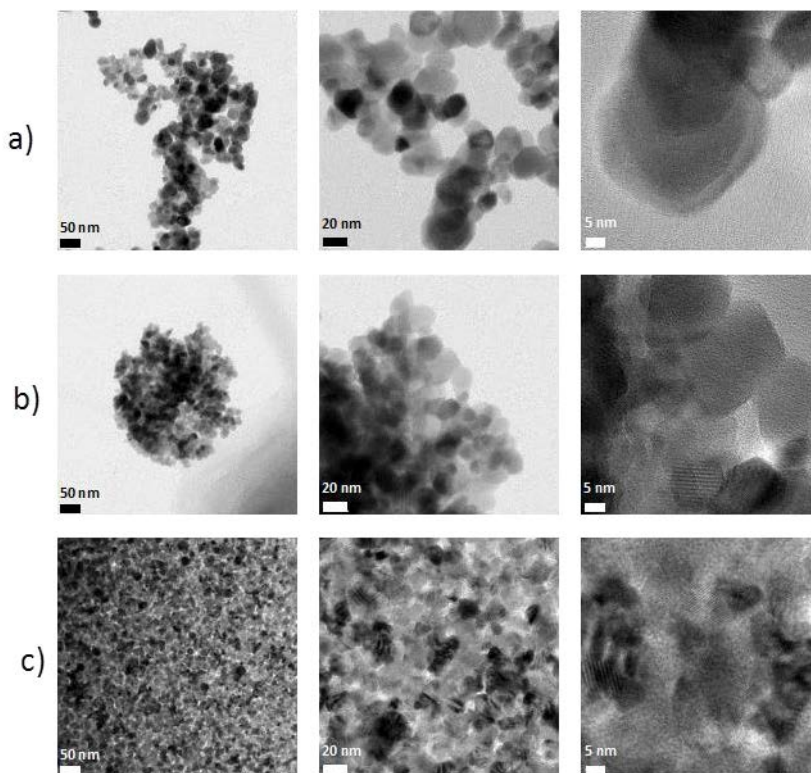


Fig 6.10: a) TEM images of Co-4, b) Co-6 and c) Co-8.

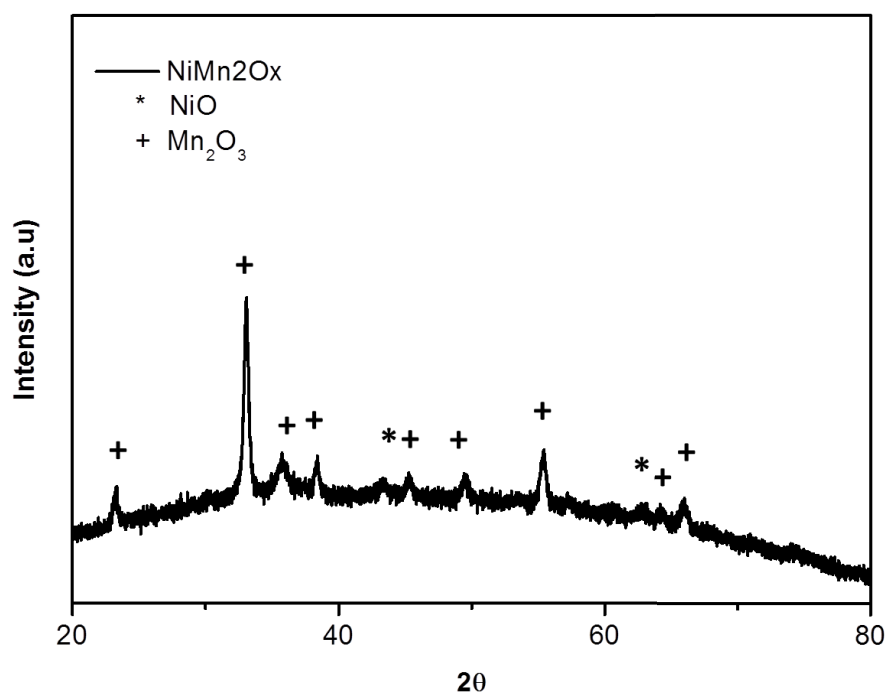


Fig 6.11: XRD patterns of NiMn<sub>2</sub>O<sub>x</sub>

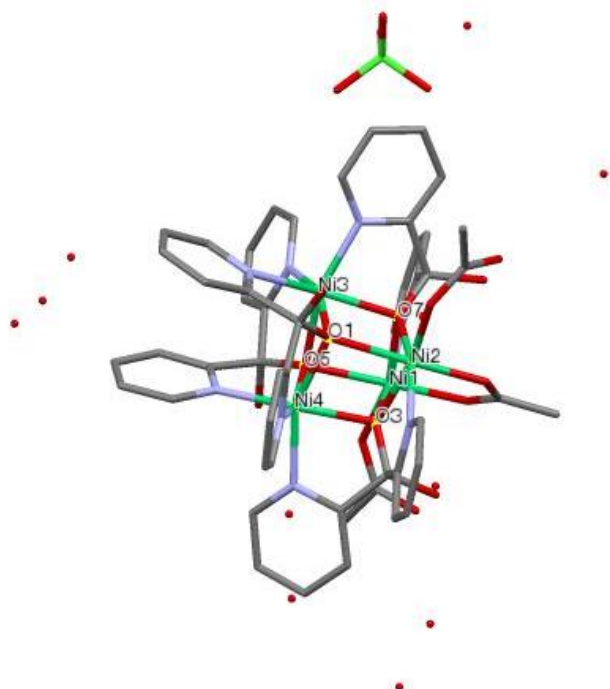


Fig 6.12: Perspective view of the cubane core of Ni<sub>4</sub> cluster.

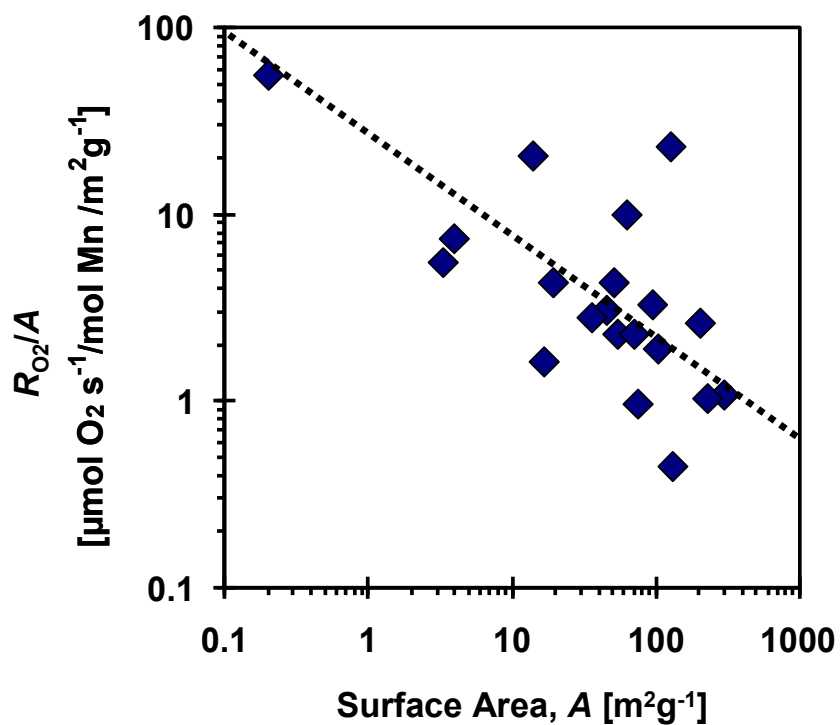


Fig 6.13: Rate of  $\text{O}_2$ -formation ( $R_{O_2}$ ) per surface area ( $A$ ) derived from the values in Table 6.3. If  $\text{O}_2$ -rate were proportional to the surface area,  $R_{O_2}/A$  should be independent on the surface ( $A$ ). Instead, a decreased activity per surface area by two orders of magnitude is observed meaning that the surface area is not the decisive determinant of the rate of catalysis (see dotted line drawn to guide the eye) (table 6.3).

**Table 6.1: ICP data of CaMn<sub>2</sub>O<sub>x</sub> samples (Mn% and Ca%).**

Sample	%Mn(w)	%Ca(w)
CaMn <sub>2</sub> O <sub>x</sub> -0.8-300	27.64	11.27
CaMn <sub>2</sub> O <sub>x</sub> -0.8-400	40.71	14.75
CaMn <sub>2</sub> O <sub>x</sub> -0.8-550	50.40	18
CaMn <sub>2</sub> O <sub>x</sub> -4-550	52.35	18.63
CaMn <sub>2</sub> O <sub>x</sub> -8-550	54.3	18.77
CaMn <sub>2</sub> O <sub>x</sub> -0.8-700	41.82	21.95

**Table 6.2: ICP data of CaMn<sub>2</sub>O<sub>x</sub> samples (Ca:Mn).**

Sample	Ca:Mn
CaMn <sub>2</sub> O <sub>x</sub> -0.8-300	1:1.80
CaMn <sub>2</sub> O <sub>x</sub> -0.8-400	1:2.11
CaMn <sub>2</sub> O <sub>x</sub> -0.8-550	1:2.04
CaMn <sub>2</sub> O <sub>x</sub> -4-550	1:2.05
CaMn <sub>2</sub> O <sub>x</sub> -8-550	1:2.10
CaMn <sub>2</sub> O <sub>x</sub> -0.8-700	1:1.38

**Table 6.3: Oxygen evolution data from ref. 88 as well as 89 and as determined in the present investigation.**

Sample	Rate (mmol O <sub>2</sub> .mol Mn <sup>-1</sup> . s <sup>-1</sup> )
CaMn <sub>2</sub> O <sub>x</sub> -8-550	0,14
CaMn <sub>2</sub> O <sub>x</sub> -4-550	0,219
CaMn <sub>2</sub> O <sub>x</sub> -0.8-550	0,62
CaMn <sub>2</sub> O <sub>x</sub> -0-550	0,029
CaMn <sub>2</sub> O <sub>x</sub> -0.8-300	0,011
CaMn <sub>2</sub> O <sub>x</sub> -0.8-400	3
CaMn <sub>2</sub> O <sub>x</sub> -0.8-700	0,082
CaMn <sub>2</sub> O <sub>x</sub> -0.8-100	0,018
Mn <sub>2</sub> O <sub>3</sub> -0.8-550	0,101
α-Mn <sub>2</sub> O <sub>3</sub>	0,027
CaMn <sub>2</sub> O <sub>4</sub> .4H <sub>2</sub> O(2)	0,325
CaMn <sub>2</sub> O <sub>4</sub> .H <sub>2</sub> O(3)	0,54
CaMn <sub>2</sub> O <sub>4</sub> .4H <sub>2</sub> O(5)	0,29
Ca <sub>0.14</sub> -birnessite	0,311
Ca <sub>0.27</sub> -birnessite	0,239

## Appendix

Table 6.4: EXAFS simulation parameters and  $1\sigma$  uncertainty ranges in the EXAFS fit parameters. Parameters marked by \* were constrained. All Mn-Ca distances were constrained to be equal in the Mn and Ca spectra, e.g., equal Mn-Ca distances in the Mn-EXAFS and the Ca-EXAFS (joint-fit approach). For simulation of the first manganese coordination sphere, two shells of backscattering atoms were used and the sum of the two coordination numbers was constrained to be equal to six. In the two-shell simulation of the first Ca and Mn coordination sphere, the values of the Debye-Waller parameter (denoted as  $\sigma$  or  $s$ ) were constrained to be equal.

	N	R, Å	s, Å		N	R, Å	s, Å	
	Mn-O				Ca-O			
100 oC	0.9 ± 0.2	1.91 ± 0.026	0.09 ± 0.005		3.4 ± 0.2	2.36 ± 0.006	0.05 ± 0.005	
300 oC	1.4 ± 0.1	1.90 ± 0.009	0.09 ± 0.003		2.0 ± 0.2	2.30 ± 0.011	0.07 ± 0.007	
400 oC	5.5 ± 0.1	1.88 ± 0.00	0.08 ± 0.00		3.7 ± 0.4	2.35 ± 0.01	0.06 ± 0.01	
550 oC	5.4 ± 0.2	1.89 ± 0.00	0.07 ± 0.00		3.4 ± 0.3	2.33 ± 0.01	0.05 ± 0.01	
700 oC	5.5 ± 0.2	1.89 ± 0.00	0.06 ± 0.00		3.0 ± 1.1	2.28 ± 0.03	0.08 ± 0.02	
550 oC no CN	5.2 ± 0.2	1.89 ± 0.00	0.06 ± 0.00		2.6 ± 0.3	2.37 ± 0.01	0.0632* ± 0.00	
	Mn-O				Ca-O			
100 oC	5.14* ± 0.0	2.17 ± 0.01	0.0911* ± 0.00		3.8 ± 0.3	2.50 ± 0.006	0.0541* ± 0.00	
300 oC	4.61* ± 0.0	2.15 ± 0.01	0.0933* ± 0.00		3.9 ± 0.4	2.44 ± 0.01	0.0698* ± 0.00	
400 oC	0.52* ± 0.0	2.29 ± 0.04	0.0797* ± 0.00		2.1 ± 0.2	2.48 ± 0.01	0.0622* ± 0.00	
550 oC	0.641* ± 0.0	2.29 ± 0.03	0.0732* ± 0.00		1.8 ± 0.2	2.48 ± 0.01	0.0548* ± 0.00	
700 oC	0.529* ± 0.0	2.31 ± 0.04	0.0605* ± 0.00		3.0 ± 1.0	2.39 ± 0.03	0.0818* ± 0.00	
550 oC no CN	0.849* ± 0.0	2.21 ± 0.02	0.0624* ± 0.00		1.4 ± 0.3	2.55 ± 0.02	0.0632* ± 0.00	
	Mn-Mn				Ca-Ca			
100 oC	0.3 ± 0.1	2.90 ± 0.026	0.0632* ± 0.00		1.3 ± 0.3	4.41 ± 0.013	0.0632* ± 0.00	
300 oC	0.2 ± 0.1	2.87 ± 0.02	0.0632* ± 0.00		0.8 ± 0.6	3.61 ± 0.08	0.0632* ± 0.00	
400 oC	1.5 ± 0.1	2.87 ± 0.00	0.0632* ± 0.00		2.4 ± 0.3	4.08 ± 0.01	0.0632* ± 0.00	
550 oC	1.8 ± 0.1	2.87 ± 0.00	0.0632* ± 0.00		1.1 ± 0.4	4.76 ± 0.02	0.0632* ± 0.00	
700 oC	2.7 ± 0.3	2.88 ± 0.00	0.0620 ± 0.00		2.9 ± 0.6	3.46 ± 0.01	0.0632* ± 0.00	
550 oC no CN	1.3 ± 0.2	2.87 ± 0.01	0.0632* ± 0.00		1.3 ± 0.3	4.07 ± 0.02	0.0632* ± 0.00	
	Mn-O/C/Mn				Ca-O/C			
100 oC	3.9 ± 1.0	3.22 ± 0.03	0.0632* ± 0.00		3.1 ± 1.1	3.73 ± 0.02	0.0632* ± 0.00	
300 oC	1.9 ± 0.4	3.11 ± 0.02	0.0632* ± 0.00		5.2 ± 1.2	3.73 ± 0.03	0.0632* ± 0.00	
400 oC	3.4 ± 1.0	3.52 ± 0.02	0.0632* ± 0.00		1.4 ± 0.7	3.66 ± 0.03	0.0387* ± 0.00	
550 oC	6.8 ± 2.3	3.487* ± 0.00	0.0387* ± 0.00		3.37 ± 0.9	3.707 ± 0.044	0.0632* ± 0.00	
700 oC	6.0 ± 0.0	3.58 ± 0.01	0.0632* ± 0.00		4.6 ± 1.6	3.69 ± 0.05	0.0632* ± 0.00	
550 oC no CN	3.9 ± 0.3	3.43 ± 0.00	0.0632* ± 0.00					
	Mn-Ca				Ca-Mn			
400 oC	0.2 ± 0.2	3.17 ± 0.01	0.0632* ± 0.00		0.4 ± 0.1	3.166* ± 0.00	0.0632* ± 0.00	
550 oC	2.8 ± 0.8	3.24 ± 0.01	0.0632* ± 0.00		0.3 ± 0.2	3.239* ± 0.00	0.0632* ± 0.00	
700 oC	0.2 ± 0.3	3.31 ± 0.01	0.0632* ± 0.00		1.6 ± 0.4	3.313* ± 0.00	0.0632* ± 0.00	
550 oC no CN	2.6 ± 0.3	3.18 ± 0.01	0.0632* ± 0.00		1.1 ± 0.2	3.18* ± 0.00	0.0632* ± 0.00	
	Mn-Mn				Ca-Ca			
100 oC	1.4 ± 0.3	3.35 ± 0.01	0.0632* ± 0.00		0.6 ± 0.2	3.549 ± 0.02	0.0632* ± 0.00	
300 oC	0.3 ± 0.1	3.38 ± 0.02	0.0632* ± 0.00		0.3 ± 0.6	3.50 ± 0.13	0.0632* ± 0.00	
400 oC	1.0 ± 0.3	3.38 ± 0.01	0.0632* ± 0.00		0.4 ± 0.3	3.53 ± 0.03	0.0632* ± 0.00	
550 oC	4.0 ± 1.4	3.36 ± 0.01	0.0632* ± 0.00		1.2 ± 0.3	3.46 ± 0.01	0.0632* ± 0.00	
	Mn-Ca				Ca-Mn			
400 oC	0.0 ± 0.2	3.84 ± 0.01	0.0632* ± 0.00		1.0 ± 0.3	3.84* ± 0.00	0.0632* ± 0.00	
550 oC	2.0 ± 0.5	3.68 ± 0.01	0.0632* ± 0.00		0.8 ± 0.7	3.679* ± 0.00	0.0632* ± 0.00	
700 oC	2.0 ± 0.4	3.70 ± 0.02	0.0632* ± 0.00		3.4 ± 0.7	3.701* ± 0.00	0.0632* ± 0.00	
					Ca-Ca			
400 oC					0.2 ± 0.7	4.45 ± 0.07	0.0632* ± 0.00	
550 oC					1.8 ± 0.9	5.42 ± 0.02	0.0632* ± 0.00	
700 oC					2.3 ± 0.4	4.34 ± 0.01	0.0632* ± 0.00	
550 oC no CN					0.2 ± 0.4	4.48 ± 0.12	0.0632* ± 0.00	



### 7. References

- [1] "US Census Bureau , International Data Base," can be found under <http://www.census.gov/population/international/data/idb/informationGateway.php>.
- [2] H. C. J. Godfray, J. R. Beddington, I. R. Crute, L. Haddad, D. Lawrence, J. F. Muir, J. Pretty, S. Robinson, S. M. Thomas, C. Toulmin, *Sci.* **2010**, *327*, 812–818.
- [3] T. P. Barnett, J. C. Adam, D. P. Lettenmaier, *Nature* **2005**, *438*, 303–309.
- [4] A. P. Kirilenko, R. A. Sedjo, *Proc. Natl. Acad. Sci.* **2007**, *104*, 19697–19702.
- [5] N. Armaroli, V. Balzani, *Energy for a Sustainable World*, Wiley-VCH, Weinheim, 2010.
- [6] C. K. Rofer-DePoorter, *Chem. Rev.* **1981**, *81*, 447–474.
- [7] R. B. Anderson, *The Fischer-Tropsch Synthesis*, Academic Press, New York, **1984**.
- [8] "Renewables 2013, global status report," can be found under [http://www.ren21.net/portals/0/documents/resources/gsr/2013/gsr2013\\_lowres.pdf](http://www.ren21.net/portals/0/documents/resources/gsr/2013/gsr2013_lowres.pdf).
- [9] N. S. Lewis, D. G. Nocera, *Proc. Natl. Acad. Sci.* **2006**, *103*, 15729–15735.
- [10] J. Dukes, *Clim. Change* **2003**, *61*, 31–44.
- [11] R. E. Blankenship, *Molecular Mechanisms of Photosynthesis*, Blackwell Science, Oxford, **2011**.
- [12] B. M. Griffin, J. Schott, B. Schink, *Sci.* **2007**, *316*, 1870.
- [13] J. Biesiadka, B. Loll, J. Kern, K.-D. Irrgang, A. Zouni, *Phys. Chem. Chem. Phys.* **2004**, *6*, 4733–4736.
- [14] Y. Umena, K. Kawakami, J.-R. Shen, N. Kamiya, *Nature* **2011**, *473*, 55–60.
- [15] H. Dau, M. Haumann, *Coord. Chem. Rev.* **2008**, *252*, 273–295.
- [16] H. Dau, P. Liebisch, M. Haumann, *Anal. Bioanal. Chem.* **2003**, *376*, 562–583.
- [17] P. E. M. Siegbahn, *Acc. Chem. Res.* **2009**, *42*, 1871–1880.
- [18] P. E. M. Siegbahn, *Chem. – A Eur. J.* **2008**, *14*, 8290–8302.
- [19] J. Barber, *Chem. Soc. Rev.* **2009**, *38*, 185–96.
- [20] G. Ciamician, *Sci.* **1912**, *36*, 385–394.
- [21] R. R. Hautala, B. R. King, C. Kotal, *Solar Energy: Chemical Conversion and Storage*, Humana Press, **1979**.
- [22] V. Balzani, L. Moggi, M. F. Manfrin, F. Bolletta, M. Gleria, *Sci.* **1975**, *189*, 852–856.
- [23] C. Collings, Anthony F., Critchley, *Artificial Photosynthesis*, Wiley-VCH, Weinheim., **2005**.

## References

---

- [24] A. J. Bard, L. R. Faulkner, *Electrochemical methods, fundamental and applications*, John Wiley & Sons, Ltd.
- [25] A. Singh, L. Spiccia, *Coord. Chem. Rev.* **2013**, *257*, 2607–2622.
- [26] M. A. Pen˜a, J. P. Gómez, J. L. G. Fierro, *Appl. Catal. A Gen.* **1996**, *144*, 7–57.
- [27] K. Aasberg-Petersen, J.-H. Bak Hansen, T. Christensen, I. Dybkjaer, P. S. Christensen, C. Stub Nielsen, S. E. Winter Madsen, J. Rostrup-Nielsen, *Appl. Catal. A Gen.* **2001**, *221*, 379–387.
- [28] J. R. Rostrup-Nielsen, *Catal. Today* **1993**, *18*, 305–324.
- [29] J. H. Lunsford, *Catal. Today* **2000**, *63*, 165–174.
- [30] A. M. Gadalla, B. Bower, *Chem. Eng. Sci.* **1988**, *43*, 3049–3062.
- [31] M. Beller, A. Renken, R. A. van Santen, Eds., *Catalysis, From Principles to Applications*, Wiley-VCH Verlag GmbH & Co. KGaA, **2012**.
- [32] N. Pal, A. Bhaumik, *Adv. Colloid Interface Sci.* **2013**, *189-190*, 21–41.
- [33] S. Jackson, J. S. J. Hargreaves, Eds., *Metal Oxide Catalysis*, Wiley-VCH Verlag GmbH & Co. KGaA, Weinheim, **2009**.
- [34] K. P. de Jong, Ed., *Synthesis of Solid Catalysis*, Wiley-VCH Verlag GmbH & Co. KGaA, **2009**.
- [35] Z. Li, M. Jaroniec, *J. Am. Chem. Soc.* **2001**, *123*, 9208–9209.
- [36] E. Flaigen, R. Patton, S. Wison, *Stud. Surf. Sci. Catal.* **1988**, *37*, 13–27.
- [37] C.-F. Cheng, Z. Luan, J. Klinowski, *Langmuir* **1995**, *11*, 2815–2819.
- [38] J. a. Schwarz, C. Contescu, A. Contescu, *Chem. Rev.* **1995**, *95*, 477–510.
- [39] A. Neimark, L. I. Kheifets, V. B. Fenelonov, *Ind. Eng. Chem. Prod. Res. Dev.* **1981**, *20*, 439.
- [40] S. Lee, R. Aris, *Catal. Rev. Sci. Eng.* **1985**, *27*, 207.
- [41] A. Lekhal, B. J. Glasser, J. G. Khinast, *Chem. Eng. Sci.* **2001**, *56*, 4473–4487.
- [42] V. B. Shevjakov, A. M., Kuznetsova, G. N., Aleskovskii, in *High Temp. Chem. Oxides*, Nauka, Leningrad, USSR, Leningrad, Russian, **1967**, pp. 149–155.
- [43] T. Suntola, in *AVS Top. Conf. At. Layer Depos. ALD*, Helsinki, Finland, **2004**.
- [44] T. Suntola, J. Antson, Method for producing compound thin films, US 4058430 A, **1977**.
- [45] T. Sontula, *Mater. Sci. Rep.* **1989**, *4*, 261.
- [46] S. P. DenBaars, P. D. Dapkus, *J. Cryst. Growth* **1989**, *98*, 195–208.
- [47] S. M. Bedair, B. T. McDermott, Y. Ide, N. H. Karam, H. Hashemi, M. A. Tischler, M. Timmons, J. C. L. Tarn, N. El-Masry, *J. Cryst. Growth* **1988**, *93*, 182–189.

## References

---

- [48] S. Witkowski, N. S. Gierałtowska, Ł. Wachnicki, B. S. Witkowski, M. Godlewski, E. Guziewicz *Opt. Appl.* **2013**, *XLIII*, 17-25.
- [49] E. Ghiraldelli, C. Pelosi, E. Gombia, C. Frigeri, L. Vanzetti, S. Abdullayeva, *Jpn. J. Appl. Phys.* **2008**, *47*, 8174–8177.
- [50] R. Xu, C. G. Takoudis, *ECS J. Solid State Sci. Technol.* **2012**, *1*, N107–N114.
- [51] M.-A. Nicolet, *Appl. Surf. Sci.* **1995**, *91*, 269–276.
- [52] J. S. Becker, R. G. Gordon, *Appl. Phys. Lett.* **2003**, *82*, 2239.
- [53] J. Y. Kim, H. K. Kim, Y. Kim, Y. Do Kim, W. M. Kim, H. Jeon, **2002**, *40*, 176–179.
- [54] T. Suntola, J. Hyvarinen, *Annu. Rev. Mater. Sci.* **1985**, *15*, 177–195.
- [55] R. L. Puurunen, *J. Appl. Phys.* **2005**, *97*, 121301.
- [56] S. M. George, *Chem. Rev.* **2009**, *110*, 111–131.
- [57] N. pinna, M. Knez, Atomic Layer Deposition of Nanostructured Materials, Wiley-VCH Verlag GmbH & Co. KGaA, **2011**.
- [58] J. D. Ferguson, A. W. Weimer, S. M. George, **2000**, 95–104.
- [59] J. Lu, B. Fu, M. C. Kung, G. Xiao, J. W. Elam, H. H. Kung, P. C. Stair, *Sci.* **2012**, *335*, 1205–1208.
- [60] J. S. King, A. Wittstock, J. Biener, S. O. Kucheyev, Y. M. Wang, T. F. Baumann, S. K. Giri, A. V Hamza, M. Baeumer, S. F. Bent, *Nano Lett.* **2008**, *8*, 2405–2409.
- [61] H. Feng, J. W. Elam, J. A. Libera, M. J. Pellin, P. C. Stair, *J. Catal.* **2010**, *269*, 421–431.
- [62] H. Feng, J. W. Elam, J. A. Libera, W. Setthapun, P. C. Stair, *Chem. Mater.* **2010**, *22*, 3133–3142.
- [63] H. Feng, J. Lu, P. C. Stair, J. W. Elam, *Catal. Letters* **2011**, *141*, 512–517.
- [64] S. T. Christensen, H. Feng, J. L. Libera, N. Guo, J. T. Miller, P. C. Stair, J. W. Elam, *Nano Lett.* **2010**, *10*, 3047–3051.
- [65] A. B. F. Martinson, J. W. Elam, M. J. Pellin, *Appl. Phys. Lett.* **2009**, *94*, -.
- [66] I. D. Scott, Y. S. Jung, A. S. Cavanagh, Y. Yan, A. C. Dillon, S. M. George, S.-H. Lee, *Nano Lett.* **2010**, *11*, 414–418.
- [67] C.-C. Chao, C.-M. Hsu, Y. Cui, F. B. Prinz, *ACS Nano* **2011**, *5*, 5692–5696.
- [68] Y. Du, S. M. George, *J. Phys. Chem. C* **2007**, *111*, 8509–8517.
- [69] N. M. Adamczyk, A. A. Dameron, S. M. George, *Langmuir* **2008**, *24*, 2081–2089.
- [70] D. W. Kim, K.-D. Kim, H. O. Seo, N. K. Dey, M. J. Kim, Y. D. Kim, D. C. Lim, K. H. Lee, *Catal. Letters* **2011**, *141*, 854–859.

## References

---

- [71] H. O. Seo, J. K. Sim, K.-D. Kim, Y. D. Kim, D. C. Lim, S. H. Kim, *Appl. Catal. A Gen.* **2013**, *451*, 43–49.
- [72] S. Hu, M. R. Shaner, J. a. Beardslee, M. Lichterman, B. S. Brunschwig, N. S. Lewis, *Science* **2014**, *344*, 1005–1009.
- [73] S. T. Christensen, J. W. Elam, F. A. Rabuffetti, Q. Ma, S. J. Weigand, B. Lee, S. Seifert, P. C. Stair, K. R. Poepfelmeier, M. C. Hersam, et al., *Small* **2009**, *5*, 750–757.
- [74] J. A. Enterkin, W. Setthapun, J. W. Elam, S. T. Christensen, F. A. Rabuffetti, L. D. Marks, P. C. Stair, K. R. Poepfelmeier, C. L. Marshall, *ACS Catal.* **2011**, *1*, 629–635.
- [75] H. Feng, J. A. Libera, P. C. Stair, J. T. Miller, J. W. Elam, *ACS Catal.* **2011**, *1*, 665–673.
- [76] J. Lu, P. C. Stair, *Langmuir* **2010**, *26*, 16486–16495.
- [77] S. H. Joo, J. Y. Park, C.-K. Tsung, Y. Yamada, P. Yang, G. A. Somorjai, *Nat Mater* **2009**, *8*, 126–131.
- [78] M. Seipenbusch, A. Binder, *J. Phys. Chem. C* **2009**, *113*, 20606–20610.
- [79] J.-N. Park, A. J. Forman, W. Tang, J. Cheng, Y.-S. Hu, H. Lin, E. W. McFarland, *Small* **2008**, *4*, 1694–1697.
- [80] S. Takenaka, H. Matsumori, K. Nakagawa, H. Matsune, E. Tanabe, M. Kishida, *J. Phys. Chem. C* **2007**, *111*, 15133–15136.
- [81] R. W. J. Scott, C. Sivadinarayana, O. M. Wilson, Z. Yan, D. W. Goodman, R. M. Crooks, *J. Am. Chem. Soc.* **2005**, *127*, 1380–1381.
- [82] P. M. Arnal, M. Comotti, F. Schüth, *Angew. Chemie Int. Ed.* **2006**, *45*, 8224–8227.
- [83] F. Cheng, J. Shen, B. Peng, Y. Pan, Z. Tao, J. Chen, *Nat Chem* **2011**, *3*, 79–84.
- [84] N. P. Luneva, V. Y. Shafirovich, A. E. Shilov, *J. Mol. Catal.* **1989**, *52*, 49–62.
- [85] Y. Gorlin, T. F. Jaramillo, *J. Am. Chem. Soc.* **2010**, *132*, 13612–4.
- [86] S. Trasatti, *J. Electroanal. Chem. Interfacial Electrochem.* **1980**, *111*, 125–131.
- [87] H. Dau, I. Zaharieva, M. Haumann, *Curr. Opin. Chem. Biol.* **2012**, *3*–10.
- [88] M. Wiechen, I. Zaharieva, H. Dau, P. Kurz, *Chem. Sci.* **2012**, *3*, 2330–2339.
- [89] M. M. M. Najafpour, T. Ehrenberg, M. Wiechen, P. Kurz, *Angew. Chem. Int. Ed. Engl.* **2010**, *49*, 2233–7.
- [90] L. Gucci, G. Stefler, O. Geszti, I. Sajó, Z. Pászti, a. Tompos, Z. Schay, *Appl. Catal. A Gen.* **2010**, *375*, 236–246.
- [91] J. A. Gilbert, D. S. Eggleston, W. R. Murphy, D. A. Geselowitz, S. W. Gersten, D. J. Hodgson, T. J. Meyer, *J. Am. Chem. Soc.* **1985**, *107*, 3855–3864.

## References

---

- [92] S. W. Gersten, G. J. Samuels, T. J. Meyer, *J. Am. Chem. Soc.* **1982**, *104*, 4029–4030.
- [93] V. Artero, M. Chavarot-Kerlidou, M. Fontecave, *Angew. Chemie Int. Ed.* **2011**, *50*, 7238–7266.
- [94] D. K. Dogutan, R. McGuire, D. G. Nocera, *J. Am. Chem. Soc.* **2011**, *133*, 9178–9180.
- [95] D. J. Wasylenko, C. Ganesamoorthy, J. Borau-Garcia, C. P. Berlinguette, *Chem. Commun.* **2011**, *47*, 4249–4251.
- [96] D. Hong, J. Jung, J. Park, Y. Yamada, T. Suenobu, Y.-M. Lee, W. Nam, S. Fukuzumi, *Energy Environ. Sci.* **2012**, *5*, 7606–7616.
- [97] N. S. McCool, D. M. Robinson, J. E. Sheats, G. C. Dismukes, *J. Am. Chem. Soc.* **2011**, *133*, 11446–11449.
- [98] S. Berardi, G. La Ganga, M. Natali, I. Bazzan, F. Puntoriero, A. Sartorel, F. Scandola, S. Campagna, M. Bonchio, *J. Am. Chem. Soc.* **2012**, *134*, 11104–11107.
- [99] D. Shevchenko, M. F. Anderlund, A. Thapper, S. Styring, *Energy Environ. Sci.* **2011**, *4*, 1284–1287.
- [100] W. Rüttinger, G. C. Dismukes, *Chem. Rev.* **1997**, *97*, 1–24.
- [101] K. Beckmann, H. Uchtenhagen, G. Berggren, M. F. Anderlund, A. Thapper, J. Messinger, S. Styring, P. Kurz, *Energy Environ. Sci.* **2008**, *1*, 668–676.
- [102] E. A. Karlsson, B.-L. Lee, T. Åkermark, E. V Johnston, M. D. Kärkäs, J. Sun, Ö. Hansson, J.-E. Bäckvall, B. Åkermark, *Angew. Chemie Int. Ed.* **2011**, *50*, 11715–11718.
- [103] C. W. Cady, R. H. Crabtree, G. W. Brudvig, *Coord. Chem. Rev.* **2008**, *252*, 444–455.
- [104] M. M. Najafpour, S. I. Allakhverdiev, *Int. J. Hydrogen Energy* **2012**, *37*, 8753–8764.
- [105] M. Yagi, K. V Wolf, P. J. Baesjou, S. L. Bernasek, G. C. Dismukes, *Angew. Chemie Int. Ed.* **2001**, *40*, 2925–2928.
- [106] W. Ruettinger, M. Yagi, K. Wolf, S. Bernasek, G. C. Dismukes, *J. Am. Chem. Soc.* **2000**, *122*, 10353–10357.
- [107] R. Brimblecombe, G. F. Swiegers, G. C. Dismukes, L. Spiccia, *Angew. Chemie Int. Ed.* **2008**, *47*, 7335–7338.
- [108] R. K. Hocking, R. Brimblecombe, L.-Y. Chang, A. Singh, M. H. Cheah, C. Glover, W. H. Casey, L. Spiccia, *Nat. Chem.* **2011**, *3*, 461–6.
- [109] A. Harriman, I. J. Pickering, J. M. Thomas, P. a. Christensen, *J. Chem. Soc. Faraday Trans. 1* **1988**, *84*, 2795.
- [110] M. Dincă, Y. Surendranath, D. G. Nocera, *Proc. Natl. Acad. Sci.* **2010**, *107*, 10337–10341.
- [111] D. K. Bediako, B. Lassalle-Kaiser, Y. Surendranath, J. Yano, V. K. Yachandra, D. G. Nocera, *J. Am. Chem. Soc.* **2012**, *134*, 6801–6809.

## References

---

- [112] M. W. Kanan, D. G. Nocera, *Sci.* **2008**, *321*, 1072–1075.
- [113] M. Risch, K. Klingan, J. Heidkamp, D. Ehrenberg, P. Chernev, I. Zaharieva, H. Dau, *Chem. Commun.* **2011**, *47*, 11912–11914.
- [114] M. W. Kanan, J. Yano, Y. Surendranath, M. Dincă, V. K. Yachandra, D. G. Nocera, *J. Am. Chem. Soc.* **2010**, *132*, 13692–701.
- [115] V. Parmon, G. Elizarova, T. Kim, *React. Kinet. Catal. ...* **1982**, *21*, 195–197.
- [116] F. Jiao, H. Frei, *Chem. Commun. (Camb)*. **2010**, *46*, 2920–2.
- [117] D. G. Nocera, *Acc. Chem. Res.* **2012**, *45*, 767–776.
- [118] S. Y. Reece, J. a Hamel, K. Sung, T. D. Jarvi, A. J. Esswein, J. J. H. Pijpers, D. G. Nocera, *Science* **2011**, *334*, 645–8.
- [119] J. Pfrommer, M. Lublow, A. Azarpira, C. Göbel, M. Lücke, A. Steigert, M. Pogrzeba, P. W. Menezes, A. Fischer, T. Schedel-Niedrig, et al., *Angew. Chemie* **2014**, *126*, 5283–5287.
- [120] H. Bode, K. Dehmelt, J. Witte, *Electrochim. Acta* **1966**, *11*, 1079–IN1.
- [121] M. R. Gennero de Chialvo, A. C. Chialvo, *Electrochim. Acta* **1988**, *33*, 825–830.
- [122] M. E. G. Lyons, M. P. Brandon, **2008**, *3*, 1386–1424.
- [123] B. S. Yeo, A. T. Bell, *J. Phys. Chem. C* **2012**, *116*, 8394–8400.
- [124] P. W. T. Lu, S. Srinivasan, *J. Electrochem. Soc.* **1978**, *125*, 1416–1422.
- [125] X. Wang, *Int. J. Hydrogen Energy* **2004**, *29*, 967–972.
- [126] K. Sun, N. Park, Z. Sun, J. Zhou, J. Wang, X. Pang, S. Shen, S. Y. Noh, Y. Jing, S. Jin, et al., *Energy Environ. Sci.* **2012**, *5*, 7872–7877.
- [127] M. Russell, A. Hall, *Mem. Soc. ...* **2006**, *80301*, DOI 10.1130/2006.1198(01).
- [128] H. Welfare, **1999**, *96*, 3447–3454.
- [129] M. Morita, C. Iwakura, H. Tamura, *Electrochim. Acta* **1977**, *22*, 325–328.
- [130] F. Zhou, A. Izgorodin, R. K. Hocking, L. Spiccia, D. R. MacFarlane, *Adv. Energy Mater.* **2012**, *2*, 1013–1021.
- [131] R. Brimblecombe, A. Koo, G. C. Dismukes, G. F. Swiegers, L. Spiccia, *J. Am. Chem. Soc.* **2012**, *132*, 2892–2894.
- [132] V. B. R. Boppana, F. Jiao, *Chem. Commun.* **2011**, *47*, 8973–8975.
- [133] M. M. Najafpour, F. Rahimi, M. Amini, S. Nayeri, M. Bagherzadeh, *Dalt. Trans.* **2012**, 11026–11031.

## References

---

- [134] A. Iyer, J. Del-Pilar, C. K. King ondu, E. Kissel, H. F. Garces, H. Huang, A. M. El-Sawy, P. K. Dutta, S. L. Suib, *J. Phys. Chem. C* **2012**, *116*, 6474–6483.
- [135] M. M. Najafpour, *Dalt. Trans.* **2011**, *40*, 3805–3807.
- [136] D. M. Robinson, Y. B. Go, M. Greenblatt, G. C. Dismukes, *J. Am. Chem. Soc.* **2010**, *132*, 11467–11469.
- [137] D. M. Robinson, Y. B. Go, M. Mui, G. Gardner, Z. Zhang, D. Mastrogiovanni, E. Garfunkel, J. Li, M. Greenblatt, G. C. Dismukes, *J. Am. Chem. Soc.* **2013**, *135*, 3494–501.
- [138] A. Indra, P. W. Menezes, I. Zaharieva, E. Baktash, J. Pfrommer, M. Schwarze, H. Dau, M. Driess, *Angew. Chemie Int. Ed.* **2013**, *52*, 13206–13210.
- [139] M. M. Najafpour, *Orig. Life Evol. Biosph.* **2011**, *41*, 237–47.
- [140] K. Kailasam, J. D. Epping, A. Thomas, S. Losse, H. Junge, *Energy Environ. Sci.* **2011**, *4*, 4668–4674.
- [141] J. Z. Marinho, F. C. Romeiro, S. C. S. Lemos, F. V. Motta, C. S. Riccardi, M. S. Li, E. Longo, R. C. Lima, *J. Nanomater.* **2012**, *2012*, 1–7.
- [142] J.-Y. Zheng, J.-B. Pang, K.-Y. Qiu, Y. Wei, *J. Mater. Chem.* **2001**, *11*, 3367–3372.
- [143] B. V. Lotsch, W. Schnick, *Chem. – A Eur. J.* **2007**, *13*, 4956–4968.
- [144] A. Thomas, A. Fischer, F. Goettmann, M. Antonietti, J.-O. Muller, R. Schlogl, J. M. Carlsson, *J. Mater. Chem.* **2008**, *18*, 4893–4908.
- [145] A. E. Shilov, *Kinet. Katal.* **1979**, *20*, 1156–1162.
- [146] N. N. Greenwood, A. Earnshaw, *Chemistry of the Elements*, Butterworth-Heinemann, Oxford, **1997**.
- [147] C. M. Julien, M. Massot, C. Poinignon, *Spectrochim. Acta Part A Mol. Biomol. Spectrosc.* **2004**, *60*, 689–700.
- [148] T. R. White, W. S. Glaunsinger, H. S. Horowitz, J. M. Longo, *J. Solid State Chem.* **1979**, *29*, 205–214.
- [149] G. B. Ansell, M. A. Modrick, J. M. Longo, K. R. Poeppemeler, H. S. Horowitz, *Acta Crystallogr., Sect. B Struct. Sci.* **1982**, *38*, 1795–1797.
- [150] I. Zaharieva, M. M. Najafpour, M. Wiechen, M. Haumann, P. Kurz, H. Dau, *Energy Environ. Sci.* **2011**, *4*, 2400–2408.
- [151] D. Shevela, S. Koroidov, M. M. Najafpour, J. Messinger, P. Kurz, *Chem. – A Eur. J.* **2011**, *17*, 5415–5423.
- [152] B. A. Pinaud, Z. Chen, D. N. Abram, T. F. Jaramillo, *J. Phys. Chem. C* **2011**, *115*, 11830–11838.
- [153] H. Dau, M. Haumann, *Coord. Chem. Rev.* **2008**, *252*, 273–295.

## References

---

- [154] E. Y. Tsui, T. Agapie, *Nat. Chem.* **2013**, 110, 10084-10088.
- [155] N. A. Pecoraro, M. J. B. V. L., Caudle, M. T., Hsieh, W.-Y., Law, *Pure Appl. Chem.* **1998**, 70, 925–929.
- [156] J. Limburg, V. A. Szalai, G. W. Brudvig, *J. Chem. Soc. Dalton Trans.* **1999**, 0, 1353–1362.
- [157] F. Jiao, H. Frei, *Chem. Commun.* **2010**, 46, 2920–2922.
- [158] K. Mette, A. Bergmann, J.-P. Tessonnier, M. Hävecker, L. Yao, T. Ressler, R. Schlögl, P. Strasser, M. Behrens, *ChemCatChem* **2012**, 4, 851–862.
- [159] S. Zouari, L. Ranno, A. Cheikh-Rouhou, O. Isnard, M. Pernet, P. Wolfers, P. Strobel, *J. Alloys Compd.* **2003**, 353, 5–11.
- [160] J. E. Penner-Hahn, *Coord. Chem. Rev.* **1999**, 190-192, 1101–1123.
- [161] G. Villalobos, M., Lanson, B., Manceau, A., Toner, B., Sposito, *Am. Miner.* **2006**, 91, 489–502.
- [162] J. E. Post, *Proc. Natl. Acad. Sci.* **1999**, 96, 3447–3454.
- [163] H. Dau, C. Limberg, T. Reier, M. Risch, S. Roggan, P. Strasser, *ChemCatChem* **2010**, 2, 724–761.
- [164] R. W. G. Wyckoff, *Crystal Structures*, Interscience Publishers, **1963**.
- [165] T. G. Spiro, J. R. Bargar, G. Sposito, B. M. Tebo, *Acc. Chem. Res.* **2009**, 43, 2–9.
- [166] B. M. Tebo, J. R. Bargar, B. G. Clement, G. J. Dick, K. J. Murray, D. Parker, R. Verity, S. M. Webb, *Annu. Rev. Earth Planet. Sci.* **2004**, 32, 287–328.
- [167] Y. Zhang, Q. Pan, G. Chai, M. Liang, G. Dong, Q. Zhang, J. Qiu, *Sci. Rep.* **2013**, 3.
- [168] M. M. Najafpour, S. Heidari, E. Amini, M. Khatamian, R. Carpentier, S. I. Allakhverdiev, *J. Photochem. Photobiol. B.* **2014**, 133C, 124–139.
- [169] A. Erdoheily, *J. Catal.* **1993**, 141, 287–299.
- [170] Z. Zhang, *J. Catal.* **1996**, 158, 51–63.
- [171] C. Carrara, J. Múnera, E. A. Lombardo, L. M. Cornaglia, *Top. Catal.* **2008**, 51, 98–106.
- [172] J. Kehres, J. G. Jakobsen, J. W. Andreasen, J. B. Wagner, H. Liu, A. Molenbroek, J. Sehested, I. Chorkendorff, T. Vegge, *J. Phys. Chem. C* **2012**, 116, 21407–21415.
- [173] P. Ferreira-Aparicio, C. Márquez-Alvarez, I. Rodríguez-Ramos, Y. Schuurman, A. Guerrero-Ruiz, C. Mirodatos, *J. Catal.* **1999**, 184, 202–212.
- [174] F. Barrai, T. Jackson, N. Whitmore, M. Castaldi, *Catal. Today* **2007**, 129, 391–396.
- [175] M. C. J. Bradford, M. a. Vannice, *Catal. Rev.* **1999**, 41, 1–42.
- [176] C. Liu, J. Ye, J. Jiang, Y. Pan, *ChemCatChem* **2011**, 3, 529–541.
- [177] S. Wang, *Appl. Catal. B Environ.* **1998**, 16, 269–277.

## References

---

- [178] M. Rezaei, S. M. Alavi, S. Sahebdehfar, L. Xinmei, L. Qian, Z.-F. Yan, *Energy & Fuels* **2007**, *21*, 581–589.
- [179] N. Laosiripojana, S. Assabumrungrat, *Appl. Catal. B Environ.* **2005**, *60*, 107–116.
- [180] D. Liu, X.-Y. Quek, H. H. A. Wah, G. Zeng, Y. Li, Y. Yang, *Catal. Today* **2009**, *148*, 243–250.
- [181] A. Albarazi, P. Beaunier, P. Da Costa, *Int. J. Hydrogen Energy* **2013**, *38*, 127–139.
- [182] T. Horiuchi, K. Sakuma, T. Fukui, Y. Kubo, T. Osaki, T. Mori, *Appl. Catal. A Gen.* **1996**, *144*, 111–120.
- [183] J. Juan-Juan, M. C. Román-Martínez, M. J. Illán-Gómez, *Appl. Catal. A Gen.* **2006**, *301*, 9–15.
- [184] G. Gonçalves, M. K. Lenzi, O. A. A. Santos, L. M. M. Jorge, *J. Non. Cryst. Solids* **2006**, *352*, 3697–3704.
- [185] J. Blanchard, A. J. Nsungui, N. Abatzoglou, F. Gitzhofer, **2007**, *85*, 889–899.
- [186] S. Yasyerli, S. Filizgok, H. Arbag, N. Yasyerli, G. Dogu, *Int. J. Hydrogen Energy* **2011**, *36*, 4863–4874.
- [187] B. Koubaissy, A. Pietraszek, A. C. Roger, A. Kiennemann, *Catal. Today* **2010**, *157*, 436–439.
- [188] Ş. Özkara-Aydinoğlu, A. E. Aksoylu, *Int. J. Hydrogen Energy* **2011**, *36*, 2950–2959.
- [189] S. Damyanova, B. Pawelec, K. Arishtirova, J. L. G. Fierro, C. Sener, T. Dogu, *Appl. Catal. B Environ.* **2009**, *92*, 250–261.
- [190] M. García-Diéguez, E. Finocchio, M. Á. Larrubia, L. J. Alemany, G. Busca, *J. Catal.* **2010**, *274*, 11–20.
- [191] J. Choi, K. Moon, Y. Gul, J. Sung, C. Kim, D. L. Trimm, **1998**, *52*, 43–47.
- [192] T. Osaki, *J. Catal.* **2001**, *204*, 89–97.
- [193] D. San José-Alonso, M. J. Illán-Gómez, M. C. Román-Martínez, *Catal. Today* **2011**, *176*, 187–190.
- [194] F. Frusteri, F. Arena, G. Calogero, T. Torre, a. Parmaliana, *Catal. Commun.* **2001**, *2*, 49–56.
- [195] Z. Hou, T. Yashima, *Appl. Catal. A Gen.* **2004**, *261*, 205–209.
- [196] R. Bouarab, O. Akdim, A. Auroux, O. Cherifi, C. Mirodatos, *Appl. Catal. A Gen.* **2004**, *264*, 161–168.
- [197] Ş. Özkara-Aydinoğlu, A. E. Aksoylu, *Catal. Commun.* **2010**, *11*, 1165–1170.
- [198] Q. JING, X. ZHENG, *Energy* **2006**, *31*, 2184–2192.
- [199] J. Montoya, *Catal. Today* **2000**, *63*, 71–85.

## References

---

- [200] W. Wang, S. M. Stagg-Williams, F. B. Noronha, L. V. Mattos, F. B. Passos, *Catal. Today* **2004**, *98*, 553–563.
- [201] S. Seok, *J. Catal.* **2002**, *209*, 6–15.
- [202] L. Zhi Min, W. Jian Li, Z. Jun Bo, C. Yao Qiang, Y. Sheng Hui, G. Mao Chu, *J. Hazard. Mater.* **2007**, *149*, 742–6.
- [203] D. Terribile, A. Trovarelli, C. de Leitenburg, A. Primavera, G. Dolcetti, *Catal. Today* **1999**, *47*, 133–140.
- [204] J. R. Rostrup-Nielsen, *Catalysis, Science and Technology*, Springer, Berlin, **1984**.
- [205] M. G. González, N. N. Nichio, B. Moraweck, G. Martin, *Mater. Lett.* **2000**, *45*, 15–18.
- [206] P. Chen, H.-B. Zhang, G.-D. Lin, K.-R. Tsai, *Appl. Catal. A Gen.* **1998**, *166*, 343–350.
- [207] X. Xie, T. Otremba, P. Littlewood, R. Schomäcker, A. Thomas, *ACS Catal.* **2012**, *3*, 224–229.
- [208] K. Takanae, K. Nagaoka, K. Nariai, K. Aika, *J. Catal.* **2005**, *232*, 268–275.
- [209] S. J. Tauster, **1986**, *298*, 1–9.
- [210] S. J. Tauster, *Acc. Chem. Res.* **1987**, *20*, 389–394.
- [211] F. Meshkani, M. Rezaei, *Int. J. Hydrogen Energy* **2010**, *35*, 10295–10301.
- [212] S. Wang, G. Lu, G. Millar, *Energy & Fuels* **1996**, *0624*, 896–904.
- [213] R. E. Reitmeier, K. Atwood, H. Bennett, H. Baugh, *Ind. Eng. Chem.* **1948**, *40*, 620–626.
- [214] A. SACCO, *J. Catal.* **1989**, *119*, 322–341.
- [215] J. H. Edwards, A. M. Maitra, *Fuel Process. Technol.* **1995**, *42*, 269–289.
- [216] H. M. Swaan, V. C. H. Kroll, G. A. Martin, C. Mirodatos, *Catal. Today* **1994**, *21*, 571–578.
- [217] V. A. Tspouriari, A. M. Efstathiou, Z. L. Zhang, X. E. Verykios, *Catal. Today* **1994**, *21*, 579–587.
- [218] E. R. S. A. Stevenson, J. a. Dumesic, R. T. K. Baker, *Metal-Support Interactions in Catalysis, Sintering and Redispersion*, **1987**.
- [219] **1964**, 1964.
- [220] V. Y. Bychkov, Y. P. Tyulenin, a. a. Firsova, E. a. Shafranovsky, A. Y. Gorenberg, V. N. Korchak, *Appl. Catal. A Gen.* **2013**, *453*, 71–79.
- [221] C. H. Bartholomew, *Appl. Catal. A Gen.* **2001**, *212*, 17–60.
- [222] S. Polarz, A. V Orlov, M. W. E. van den Berg, M. Driess, *Angew. Chem. Int. Ed. Engl.* **2005**, *44*, 7892–6.
- [223] D. Zhao, J. Feng, Q. Huo, N. Melosh, G. H. Fredrickson, B. F. Chmelka, G. D. Stucky, *Sci.* **1998**, *279*, 548–552.

## References

---

- [224] F. Habimana, X. Li, S. Ji, B. Lang, D. Sun, C. Li, *J. Nat. Gas Chem.* **2009**, *18*, 392–398.
- [225] H. Liu, H. Wang, J. Shen, Y. Sun, Z. Liu, *Appl. Catal. A Gen.* **2008**, *337*, 138–147.
- [226] R. J. Farrauto, C. H. Bartholomew, *Fundamentals of Industrial Catalytic Processes*, Blackie, London, **1997**.
- [227] D. T. Wickham, J. Engel, M. E. Karpuk, **2002**.
- [228] P. BILOEN, *J. Catal.* **1980**, *63*, 112–118.
- [229] D. Trimm, *Catal. Today* **1999**, *49*, 3–10.
- [230] J. Radnik, A. Benhmid, V. N. Kalevaru, M.-M. Pohl, A. Martin, B. Lücke, U. Dingerdissen, *Angew. Chemie Int. Ed.* **2005**, *44*, 6771–6774.
- [231] L. Cited, K. K. Ghosh, D. Kunzru, **1988**, 559–565.
- [232] J. R. Rostrup-Nielsen, I. Alstrup, *Catal. Today* **1999**, *53*, 311–316.
- [233] N. Macleod, J. R. Fryer, D. Stirling, G. Webb, *Catal. Today* **1998**, *46*, 37–54.
- [234] A. K. Rovik, S. K. Klitgaard, S. Dahl, C. H. Christensen, I. Chorkendorff, *Appl. Catal. A Gen.* **2009**, *358*, 269–278.
- [235] K. Yu, Z. Wu, Q. Zhao, B. Li, Y. Xie, *J. Phys. Chem. C* **2008**, *112*, 2244–2247.
- [236] M. Cargnello, T. Montini, S. Polizzi, N. L. Wieder, R. J. Gorte, M. Graziani, P. Fornasiero, *Dalt. Trans.* **2010**, *39*, 2122–2127.
- [237] J. Guo, H. Lou, H. Zhao, D. Chai, X. Zheng, *Appl. Catal. A Gen.* **2004**, *273*, 75–82.
- [238] J. Guo, J. Gao, B. Chen, Z. Hou, J. Fei, H. Lou, X. Zheng, *Int. J. Hydrogen Energy* **2009**, *34*, 8905–8911.
- [239] S. Takenaka, E. Kato, Y. Tomikubo, K. Otsuka, *J. Catal.* **2003**, *219*, 176–185.
- [240] J. A. Rodríguez, J. Hrbek, *Surf. Sci.* **2010**, *604*, 241–244.
- [241] J. A. Rodriguez, J. Graciani, J. Evans, J. B. Park, F. Yang, D. Stacchiola, S. D. Senanayake, S. Ma, M. Pérez, P. Liu, et al., *Angew. Chemie Int. Ed.* **2009**, *48*, 8047–8050.
- [242] D. V Potapenko, J. Hrbek, R. M. Osgood, *ACS Nano* **2008**, *2*, 1353–1362.
- [243] M. Juppo, A. Rahtu, M. Ritala, M. Leskelä, *Langmuir* **2000**, *16*, 4034–4039.
- [244] A. Rahtu, T. Alaranta, M. Ritala, *Langmuir* **2001**, *17*, 6506–6509.
- [245] A. C. Dillon, A. W. Ott, J. D. Way, S. M. George, *Surf. Sci.* **1995**, *322*, 230–242.
- [246] A. W. Ott, J. W. Klaus, J. M. Johnson, S. M. George, *Thin Solid Films* **1997**, *292*, 135–144.
- [247] R. L. Puurunen, *J. Appl. Phys.* **2005**, *97*, -.

## References

---

- [248] J. Lu, B. Liu, J. P. Greeley, Z. Feng, J. a. Libera, Y. Lei, M. J. Bedzyk, P. C. Stair, J. W. Elam, *Chem. Mater.* **2012**, *24*, 2047–2055.
- [249] J. a. Dieringer, A. D. McFarland, N. C. Shah, D. a. Stuart, A. V. Whitney, C. R. Yonzon, M. a. Young, X. Zhang, R. P. Van Duyne, *Faraday Discuss.* **2006**, *132*, 9.
- [250] A. V. Whitney, J. W. Elam, S. Zou, A. V. Zinovev, P. C. Stair, G. C. Schatz, R. P. Van Duyne, *J. Phys. Chem. B* **2005**, *109*, 20522–20528.
- [251] X. L. Zhou, J. M. White, *Surf. Sci.* **1992**, *273*, 322–340.
- [252] S. Wang, G. Q. (Max) Lu, G. J. Millar, *Energy & Fuels* **1996**, *10*, 896–904.
- [253] N. a. Ray, R. P. Van Duyne, P. C. Stair, *J. Phys. Chem. C* **2012**, *116*, 7748–7756.
- [254] J. Lu, J. W. Elam, P. C. Stair, *Acc. Chem. Res.* **2013**, *46*, 1806–1815.
- [255] J. Lu, B. Fu, M. C. Kung, G. Xiao, J. W. Elam, H. H. Kung, P. C. Stair, *Science* **2012**, *335*, 1205–1208.
- [256] F. Solymosi, *J. Mol. Catal.* **1991**, *65*, 337–358.
- [257] M. F. Mark, W. F. Maier, **1993**.
- [258] J. H. Bitter, K. Seshan, J. A. Lercher, **1997**, *286*, 279–286.
- [259] J. Nakamura, K. Aikawa, K. Sate, T. Uchijima, **1994**, *25*, 265–270.
- [260] R. K. Hocking, R. Brimblecombe, L.-Y. Chang, A. Singh, M. H. Cheah, C. Glover, W. H. Casey, L. Spiccia, *Nat. Chem.* **2011**, *3*, 461–6.
- [261] I. Zaharieva, P. Chernev, M. Risch, K. Klingan, M. Kohlhoff, A. Fischer, H. Dau, *Energy Environ. Sci.* **2012**, *5*, 7081.
- [262] Z. Li, L. Mo, Y. Kathiraser, S. Kawi, **2014**.
- [263] J. W. Elam, M. D. Groner, S. M. George, *Rev. Sci. Instrum.* **2002**, *73*.
- [264] J. A. Libera, J. W. Elam, M. J. Pellin, *Thin Solid Films* **2008**, *516*, 6158–6166.
- [265] M. Schwarze, D. Stellmach, M. Schröder, K. Kailasam, R. Reske, A. Thomas, R. Schomäcker, *Phys. Chem. Chem. Phys.* **2013**, *15*, 3466–72.
- [266] “Solgel technology for textile treatment,” can be found under <http://www.centexbel.be/solgel-treatment>.
- [267] S. H. Tolbert, *Nat Mater* **2012**, *11*, 749–751.
- [268] P. Ferreira-Aparicio, I. Rodríguez-Ramos, J. A. Anderson, A. Guerrero-Ruiz, *Appl. Catal. A Gen.* **2000**, *202*, 183–196.
- [269] “Scanning Electron Microscope,” can be found under <https://www.purdue.edu/ehps/rem/rs/sem.htm>.

## References

---

- [270] "Nanotechnology: A Brief Overview," can be found under <http://barrett-group.mcgill.ca/tutorials/nanotechnology/nano02.htm>.